Recovery in aluminium

Gundlach, Carsten

Publication date:
2006

Document Version
Publisher's PDF, also known as Version of record

Recovery in aluminium

Ph.D. thesis
by
Carsten Gundlach

Supervisors:
Henning Friis Poulsen
Wolfgang Pantleon
Erik Johnson

Center for Fundamental Research: Metal structures in Four Dimensions
Risø National Laboratory
and
University of Copenhagen
March 27, 2006

Edited: January 26, 2007

Abstract

In the present thesis the development of a unique experimental method for volume characterisation of individual embedded crystallites down to a radius of 150 nm is presented. This method is applied to *in-situ* studies of recovery in aluminium.

The method is an extension of 3DXRD microscopy, an X-ray diffraction technique for studies of the evolution of grains within polycrystalline materials. The much smaller volume of the crystallites of interest here in comparison to grains implies that the existing method is not applicable due to overlap of diffraction spots. In this work this obstacle is overcome by the combined use of X-ray micro focusing optics, new scanning algorithms and the use of foils. The ratio of foil thickness to crystallite size should be at least 10 such that the central ones are situated in a bulk environment. To avoid thermal drifts, gold reference markers are deposited onto the sample. The X-ray fluorescence from these markers defines the position of the crystallites with respect to the beam to within 1 μm.

Two types of data analysis approaches have been developed. The first one generates apparent size distributions of an ensemble of crystallites. These may be converted to true size distributions by stereological tools. Uniquely, this method enables *in situ* studies of the evolution in size distribution - at a specific sample location - with good statistics (5000-20000 per 20 minutes).

The second approach generates growth curves (volume vs. time) of individual crystallites. This involves at all times 1) separating a given diffraction spot from neighbouring spots originating from other crystallites and 2) measuring the complete integrated intensity of the spot (as this is related to volume). This image analysis problem is formulated in a 5D observational space, where growth curves are represented as strings. To identify the strings a combination of a 5D connected component type algorithm and multi-peak fitting was found to be superior.

The first use of the method was a study of recovery of a deformed aluminium alloy (AA1050). The aluminium alloy was deformed by cold rolling to a thickness reduction of 38%. The sample was annealed at 300°C for 3 hours. From the statistical analysis of the size distribution most of the recovery was found to occur during the first 3 minutes of annealing. Growth curves are presented for nine individual subgrains. A difference is observed between these experimental data and predictions from curvature-driven grain growth models. The observed individual subgrains showed no evidence of rotation.

In outlook, several synchrotrons are presently developing nano-X-ray beams. Applying the methodology developed in this thesis to these beams will enable *in-situ* studies of the dynamics of bulk crystalline nano-structures down to the scale of ∼20 nm.

Dansk resumé

I denne afhandling præsenteres udviklingen af en unik metode til bestemmelse af volumener af individuelle indlejrede krystallitter ned til 150 nm præsenteret. Metoden er anvendt til *in-situ* studier af recovery i aluminium.

Metoden er en generalisering af 3DXRD mikroskopi, en synkrotron baseret diffraktionsteknik til strukturelle studier af korn indeni polykrystallinske materialer. Volumen af de krystallitter der i denne afhandling anvendes medfører at den eksisterende metode ikke var anvendelig grundet overlap i diffraktionsmønstrene. I denne afhandling overvindes denne begrænsning ved anvendelse af mikrofokuserende røntgenoptik, en ny skanningsmetode og brugen af folier som prøver. Foliets tykkelse skal være mindst 10 gange krystallit størrelsen, således at de centrale krystallitter er beliggende i prøvens indre. Til at hindre termisk drift under opvarmning afsættes guldmærker på prøverne. Røntgenfluorescensen fra disse markeringer definerer krystallitternes position i forhold til røntgenstrålen indenfor 1 μm.

To forskellige tilgange til dataanalysen er blevet udviklet. Den første frembringer fordelinger af tilsyneladende størrelse i en samling af krystallitter. Disse kan omdannes til reelle størrelsesfordelinger via stereologiske værktøjer. Denne metode muliggør *in-situ* studier af udviklingen i størrelsesfordeling i en specifik prøve med god statistik (5000-20000 per 20 minutter).

Den anden metode frembringer vækstkurver (volumen vs. tid) for individuelle krystallitter. Dette involverer til enhver tid 1) separation af en given diffraktionsplet fra nabopletter hidrørende fra andre krystallitter samt 2) måling af den fuldstændige, integrerede intensitet af pletten (dette mål er relateret til volumen). Dette billed behandlings problem er formuleret i et 5D observations rum, hvor vækstkurverne er repræsenterede som strenge. For at kunne identificere strengene var det nyttigt at benytte en kombination af en '5D sammenhængende komponenter' type algoritme og et multi-top fit.

Metoden blev anvendt første gang til et studie af recovery i en deformeret aluminium legering (AA 1050). Aluminiumslegeringen var deformeret med koldvalsning indtil en reduktion i tykkelse på 38%. Prøven blev *in-situ* varmebehandlet ved 300°C i 3 timer. Den statistiske analyse af størrelsesfordelingen gav som resultat at størstedelen af recovery processen forløb indenfor de første 3 minutter af opvarmningen. Vækstkurver blev genereret for 9 individuelle delkorn. Der observeredes en forskel mellem disse eksperimentelle data og forudsigelser i krumnings drevne korn vækst modeller. De observerede individuelle delkorn viste ingen tegn på at roterer.

I øjeblikket arbejdes der intenst på flere synkrotroner med udvikling af nano-røntgenstråler. Kombineres den i afhandlingen udviklede metode med sådanne stråler, vil det muliggøre *in-situ* bulk studier af dynamikken af krystallinske nano-strukturer ned til en størrelse på $\sim$20 nm.

Preface

This thesis is submitted in partial fulfillment of the requirement for obtaining the Ph.D. degree at the University of Copenhagen. The research described was carried out in the Center for Fundamental Research: Metal structures in Four Dimensions (4D-center), at Risø National Laboratory, under the supervision of Erik Johnson, University of Copenhagen and Henning Friis Poulsen and Wolfgang Pantleon both at the 4D-center.

The work presented in the present thesis was been carried out from the summer of 2002 to the end of 2005. During this time I had the great pleasure of working with some wonderful people and talented scientists.

I am grateful to Dorte Juul Jensen who gave me the opportunity to work within the 4D-center. I am thankful to my supervisors Wolfgang Pantleon and Henning Friis Poulsen for showing confidence in my work and me and for their enthusiasm and good spirits. I would also like to thank everyone associated with the 4D-center, for their help and discussions. A special thanks goes to the people involved in the synchrotron experiments, with whom I have spent many working nights, and to Søren Schmidt for endless discussions. None of my experiments could have been done with out the great help from the technicians Preben Olesen, Palle Nielsen, Helmer Nilsson and Gitte Christiansen and a special thanks goes to them.

Thanks to Thorbjørn Møller for proof reading the present thesis and contributing with useful suggestions.

Finally I would like to thank my family and my friends for their support. Special thanks goes to Mona for her patience and great support.

Carsten Gundlach, Amager marts 2006

Contents

List of Figures

Abbreviations

3DXRD	Three Dimensional X-Ray Diffraction
AOI	Area Of Interest
APS	Advanced Photon Source
CCD	Charge-Coupled-Device
DDW	Dense Dislocation Walls
EBSD	Electron Back-Scatter Diffraction
ESR	Equivalent Sphere Radii
ESRF	European Synchrotron Radiation Facility
FIB	Focused Ion Beam
FWHM	Full-Width-at-Half-Maximum
GNBs	Geometrically Necessary Boundaries
HAGB	High Angle Grain Boundary
IDBs	Incidental Dislocation Boundaries
LAGB	Low Angle Grain Boundary
ND	Normal Direction
RD	Rolling Direction
SEM	Scanning Electron Microscope
TD	Transverse Direction
TEM	Transmission Electron Microscope

List of Publications

I **Direct observation of subgrain evolution during recovery of cold-rolled aluminium**
C. Gundlach, W. Pantleon, E. M. Lauridsen, L. Margulies, R. Doherty and H. F. Poulsen
Scripta Materialia **50**, 477-481 (2004)

II **In-situ observation of subgrain evolution during static recovery of cold-rolled aluminium**
C. Gundlach, W. Pantleon, E. M. Lauridsen, L. Margulies, R. Doherty and H. F. Poulsen
Materials Science Forum **467-470**, 1389-1394 (2004)

III **Characterising the dynamics of individual embedded dislocation structures**
H. F. Poulsen, J. R. Bowen and C. Gundlach
Scripta Materialia **51**, 783-788 (2004)

IV **Watching the Growth of Bulk Grains During Recrystallization of Deformed Metals**
S. Schmidt, S. F. Nielsen, C. Gundlach, L. Margulies, X. Huang and D. Juul Jensen
Science **305**, 229-232 (2004)

V **In-Situ Investigation of Bulk Nucleation by X-Ray Diffraction**
A. W. Larsen, C. Gundlach, H. F. Poulsen, L. Margulies, Q. Xing and D. Juul Jensen
Materials Science Forum **467-470**, 81-86 (2004)

VI **Metal Microstructures in Four Dimensions**
S. F. Nielsen, C. Gundlach, E. M. Lauridsen, R. V. Martins, H. F. Poulsen, S. Schmidt and D. Juul Jensen
In Proceedings of IMECE2004

VII **Image analysis for X-ray studies of the dynamics of individual embedded subgrains during revovery**
C. Gundlach, S. Schmidt, L. Margulies, T. Knudsen, W. Pantleon, H. F. Poulsen
Materials Science and Technology **21**, 1476-1479 (2005)

VIII **Nucleation of recrystallization observed in situ in the bulk of a deformed metal**
A. W. Larsen, H. F. Poulsen, L. Margulies, C. Gundlach, Q. Xing, X. Huang and D. Juul Jensen
Scripta Materialia **53**, 553-557 (2005)

IX **Formation and Subdivision of Deformation Structures during Plastic Deformation**
B. Jakobsen, H. F. Poulsen, U. Lienert, J. Almer, H. O. Sørensen, C. Gundlach, and W. Pantleon
Science In press

Chapter 1

Introduction

Metallic materials play an important role in today's society. Many large cities are dominated by their skylines. To build such skylines a huge amount of steel is used. Looking at the streets in different cities of the world one see that these streets are dominated by cars or other types of transportation vehicles which have almost all been made from some sort of metal. The transportation of goods across different parts of the world is done by ships or planes, again a use of metallic material. Hence metals are the basic of much modern industry producing the goods or transportation vehicles.

The properties (mechanical, physical and chemical) of the metals can be altered by thermo-mechanical processing. This is typically done by combining diverse types of deformation and annealing processes. The various properties are to a large extent governed by the structure of the material. Metallic materials are crystals with lattices as described in solid state physics. In solid state physics most theories concern perfect lattices (single crystals) but in materials science samples are typically polycrystals containing many lattices which are rotated with respect to each other. The boundary between two lattices is labelled according to the angle between the two lattices - the misorientation angle. When the angle is small the boundary is called a Low Angle Grain Boundary (LAGB) or sometimes a dislocation boundary because the boundary consists of an array of dislocations. If the angle is large the boundary is named a High Angle Grain Boundary (HAGB). Regions of a crystal surrounded by HAGBs are labelled grains and regions surrounded by at least one boundary that is not a HAGB is named dislocation cells or subgrains; in this thesis the term subgrains are used. Grains, subgrains, HAGBs, LAGBs and dislocation boundaries constitute the structure of a

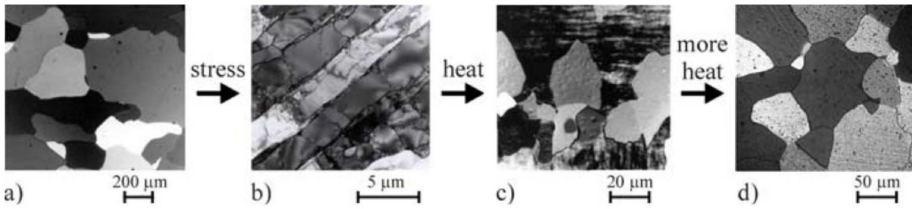

Figure 1.1: *Microstructure evolution following deformation and annealing. Reproduced from (Lauridsen, 2001).*

metallic material. The structure is usually named the microstructure because the length scale of the elements in the structure implies the use of microscopes in order to study the nature of these structures. Figure 1.1(a) shows the microstructure of a polycrystal; different contrast is from different grains or subgrains.

The link between the changes of the structure in metals due to thermomechanical processing and the changes of their properties is of great importance in order to form and design metallic materials with desired properties.

During the deformation of a metallic material point and line defects are introduced into the crystal structure of the metallic material. Line defects are named dislocations. In order to reduce their associated stress fields these dislocations form more energetically favourable dislocation structures. The details of the microstructure after deformation depend on the material. Figure 1.1(b) shows an example of a resulting microstructure after deformation.

By applying energy in the form of heat by annealing at lower temperatures individual dislocations and dislocation structures start to rearrange into new dislocation structures. The rearrangement of dislocation structures during annealing is typically summarised as part of recovery. Recovery consists of a number of different processes. Such processes are responsible for the removal of vacancies (point defects) by diffusion of such vacancies to free surfaces or boundaries. Other processes are responsible for the movement of dislocations which may result in annihilation, i.e. two dislocations cancelling each other, or rearrangement of dislocations into low energy arrays producing dislocation boundaries. The latter process is sometimes referred to as polygonisation.

One definition of recovery is given by Cotterill and Mould (1976). "*Recovery* usually implies those changes which do not involve the sweeping of

the deformed material by migrating high-angle grain boundaries. Thus, in this stage, a deformed crystal (or a polycrystalline aggregate) retains it basic identity, although the density and distribution of defects within it change."

Raising the temperature activates a new set of processes, named recrystallisation. Recrystallisation involves migration of one or more HAGBs through the microstructure, eliminating the deformation structure. When recrystallisation sets in, it is the dominating process, but recovery processes still occur in regions of the microstructure where no HAGB is migrating. During recrystallisation parts of a sample can be recrystallised while other parts are still in the deformed state, an example of the microstructure in this state is shown in figure 1.1(c). At the end of recrystallisation the microstructure consists of dislocation-free grains. The microstructure after recrystallisation, however, is not an exact reproduction of the microstructure before deformation. Figure 1.1(d) shows a microstructure after complete recrystallisation.

1.1 Motivation

As described above recovery is a set of processes which do not involve migration of HAGBs which typically means minor structural changes. However, even small structural changes alter the properties of the material.

Some of the interesting questions in recovery is: How do the microstructural changes occur? What are the conditions that lead to different types of processes? When subgrains almost have been cleared of point defects and dislocations, some subgrains are seen to increase in size. Different hypothesises have been proposed on the governing processes. One is by migration of LAGBs to reduce the total number of LAGBs which would reduce the system energy. Another hypothesis is the rotation of neighbouring subgrains, where two neighbouring subgrains rotate their crystal lattices into a common orientation. If two neighbouring subgrains have the same orientations there is no differences in the lattice and no boundary, hence the system energy is reduced.

In monitoring properties, recovery has been identified since the 1950s. By means of electron microscopy it has been possible to characterise the microstructures of specimens before and after annealing, or when interrupting the annealing process at intermediate stages. However, this type of study provides no direct information on the local interactions in, or the evolution

of the microstructure, respectively. Some *in-situ* electron microscope investigations of microstructural evolution during annealing exist, but a serious problem with electron microscopes is the combination of electron energy and stopping power, which leads to a low penetration depth. Electron microscopes are ideal and powerful to study surface processes, but since most material have a small surface-to-volume fraction, bulk processes are the most important processes in terms of material properties.

In-situ bulk characterisation at the scale of grains or subgrains was not feasible until the construction of third generation synchrotrons like the European Synchrotron Radiation Facility (ESRF), Grenoble, France. A number of different features contribute to the uniqueness of material characterisation by high energy X-rays from third generation synchrotrons: 1) High energy X-rays in the range 50-100 keV are ideal for bulk measurements in most materials. This 50-100 keV energy range is a trade off between penetration power (X-ray attenuation decreases with increasing X-ray energy) and number of diffracting photons (diffraction intensity decreases with increasing X-ray energy). 2) Extinction (attenuation of the diffracted X-rays in the diffracting material) decreases with increasing X-ray energy. 3) The development of insertion devices (wigglers and undulators) used in third generation synchrotrons lead to a dramatic increase in the photon flux.

A Three Dimensional X-Ray Diffraction (3DXRD) microscope was developed in collaboration between ESRF and Risø National Laboratory and put to use in 2000. This microscope is dedicated to *in-situ* characterisation of multiple individual scattering domains (initially only grains) during deformation or annealing, it is possible to monitor orientations, volumes, strains and positions of many grains, simultaneously.

1.2 Project work

The aim of this project was to extend the 3DXRD methodology to include a method for characterising the dynamics (the so-called growth-curves) of individual subgrains during annealing in order to study recovery processes. The basic idea is to measure subgrain volumes as a function of time. The starting point of this extension was a well-established method for the study of volumes and orientations of grains during annealing. In order to study individual subgrains the number of simultaneously diffracting subgrains had to be cut down; this turned out to be one of the main challenges of the project.

Analysing the recorded diffraction images is a major part of a 3DXRD experiment, and it is not uncommon that the time from when an experiment is performed to the time when the data is analysed and published, is more than one year. One reason for this is that the 3DXRD microscope still is not standardised and there exists no standard analytical tool. Many experiments require new analytical tools in order to analyse the specific data acquired during that experiment. The need for new analysis software was no exception in this project. A new software package to analyse growth curves based on the method developed had to be designed and implemented.

An aluminium alloy (AA1050) was selected as the material for the studies. AA1050 has been extensively studied at Risø and there exists a large knowledge base about this alloy at the Material Research Department. In order to have subgrains with detectable volumes a deformation structure at not too high strain was selected; the deformation chosen was cold rolling to 38%. For the material used in the second experiment another aluminium alloy (AA1200) with a larger deformation; cold rolled to a true strain of 2 (86.4% thickness reduction) was selected.

The time of a synchrotron experiment is limited and therefore it is highly recommended not to waste time during such an experiment. Various types of (pre-)investigations were performed to obtain knowledge to select the right annealing temperature during the 3DXRD experiment. These were electron microscope investigations of the microstructure and investigations of property changes during annealing.

During the course of the project an upgrade of the 3DXRD microscope was installed. Because I participated in this upgrade I was positioned at the ESRF for one month which gave the possibility to learn more about the operation of the microscope. In return I was a member of a small group located at Risø who was able to setup and operate the 3DXRD microscope. This meant that I have been fortunate enough to participate in a wide range of 3DXRD experiments. I have participated in six experiments at the 3DXRD microscope. Beside my own experiments on recovery, the experiments were on deformation, nucleation of recrystallisation and recrystallisation; two of these experiments are presented in this thesis. Besides the experiments at ESRF I have been part of X-ray diffraction experiments at 1-ID at the Advanced Photon Source (APS), USA and an experiment in tomography at HASYLAS, Germany.

This thesis work has resulted in nine publications (where eight, I-VIII) are reprinted at the end of the present thesis. The main part of this thesis

is based on 3 of these papers (I,II and VII).

1.3 Outline

This thesis is divided into six chapters concerning the different aspects related to the studies performed during the course of this Ph.D. project.

Chapter 1 the present chapter contains an introduction to the present thesis.

Chapter 2 includes a short introduction to recovery processes and related annealing processes. The basis of the metallic microstructure is also presented in this chapter including findings from a study of the formation of a deformed microstructure in which I had a small part.

Chapter 3 contains a presentation of the 3DXRD microscope itself and selected uses of the 3DXRD microscope. A detailed description of an existing 3DXRD method to study volumes and orientations of an ensemble of grains is provided. This method was the starting point from which I developed a method to study volumes of an ensemble of subgrains. In addition, this chapter summarises two 3DXRD annealing studies in which I have participated. The topics of these two experiments are closely related to recovery.

Chapter 4 describes the analytical software developed. Two different types of analytical tools were developed. 1) One which generates apparent size distributions of an ensemble of subgrains. This enables *in-situ* studies of the evolution of the apparent size distributions of subgrain (bulk and surface) ensembles during annealing. 2) Another which generates growth curves of individual subgrains. Each analysed subgrain has to be fully illuminated by the X-rays in order to measure the fully integrated diffraction intensity. Neighbouring diffraction spots originating from different subgrains have to be separated. Two different approaches to analysing this have been developed to fulfill these two tasks. The first approach focused on generating growth curves from a few individual subgrains in order to prove the use of the 3DXRD method. The second approach focused on producing growth curves from all non overlapping diffraction spots. A tool based on 5D Connected Component and Labelling type algorithms and multi-peak fitting was developed.

Chapter 5 presents a feasibility study of the method developed and the results and findings from the experiment. The second part of chapter 5 presents the results and findings from a second experiment where the experimental methodology had been substantially upgraded.

Chapter 6 is a summary of this thesis and an outlook, including a list of ideas for improving the developed 3DXRD method, and expanding its range of applications.

Chapter 2

Recovery: background and theories

This chapter provides a short introduction to topics related to the the studies discussed in this thesis. Recovery is part of a number of annealing processes occurring in a deformed material. Therefore recovery can not be considered as an isolated part, without considering the other parts of the annealing process (recrystallisation and grain growth). Also the deformed state of the material has to be considered. Recovery consists of a number of different processes as will be seen below. Only brief descriptions and an introduction to the different phenomena are given here because the main emphasis in this Ph.D. project has been on the technical and analytical issues concerning developing a 3DXRD method to study subgrain behaviour during annealing. For a detailed description of the phenomena the reader is referred text books on metallurgy processes and dislocations (e.g. Reed-Hill, 1964; Friedel, 1964; Cotterill and Mould, 1976; Humphreys and Harherley, 1995; Haasen, 1996; Hull and Bacon, 1984) and references within this chapter.

2.1 Introduction

Having selected a material with a suitable basket of properties to fabricate an object, a processing route has to be selected. In the case of metallic materials the main routes available are by casting from the liquid state, by compacting high melting point powders in the solid state and by working and heat treatment, again in the solid state.

This thesis is concerned with the last of these routes that is working and annealing. This route is by no means new and a good traditional example of its use is the way a blacksmith forms horseshoes. As it happens working/annealing is more or less unique to metallic materials and reflects the importance of metallic materials in engineering practice.

2.1.1 Technological interest

In the metal working industries enormous use is made of processes such as forging and rolling whereby shaping and sectioning may be generated. Here it is important to distinguish between hot working and cold working. The temperature range over which recrystallisation occurs separates these two regions. Hot working, i.e. temperatures above the recrystallisation temperature has the advantages of large section changes (strains) with low working forces and also helps to break up segregation and to refine the grain size. However, hot working does not give good dimensional accuracy or surface finish.

By contrast, in cold working much smaller strains are possible (without intermediate anneals), the working loads are much higher but the dimensional tolerance and surface finish are excellent.

There is a third regime of considerable technological interest currently and this is the warm working region which is just below the recrystallisation temperature.

The term recovery refers to changes in the properties of a deformed material which occurs before recrystallisation. These changes partially restore properties to the initial values before deformation. Some changes may occur during the deformation these are referred to as dynamic recovery.

2.1.2 Scientific interest

The relations between the underlying microstructure of metallic materials and their physical and chemical properties are of considerable scientific interest. Understanding how and why the properties are determined by the microstructure will produce one of two links that will lead to the possibility to design metallic materials with the desired properties. The other link is to understand how the microstructure changes when the metallic material is processed either by deformation, heat treatment or combinations thereof.

Investigations of the deformed microstructures have been performed since the introduction of the light microscope in the study of metals (Sörby, 1886). These investigations of the deformed microstructures have progressed in close relation with the development of other types of microscopes, such as the Transmission Electron Microscope (TEM) and the Scanning Electron Microscope (SEM).

Perhaps the reason that conventional engineers favour the use of metallic materials over other classes of engineering material is the broad range of property values (physical including mechanical, and chemical) which are achievable by microstructural control. This microstructural control can be achieved, to a very large extent, by a combination of working and annealing treatments.

2.2 Cold deformation

When a polycrystalline metallic material is plastically deformed, a series of changes to the overall material occur:

1. There is a change in the overall shape of grains. For instance in cold rolling of metallic materials with an initially equiaxed grain shape, the shape is altered to what is known as "pancake". This shape change broadly reflects the macroscopic strains imposed, which often closely approximate plane strain.

2. A second, relatively macroscopic feature, is that a deformation texture (preferred orientation) is introduced by rotation of grains due to various slip systems being activated differently in different grains.

3. A major change, which is reflected in the work hardening coefficient, $|\frac{d\sigma}{d\varepsilon}|$, seen in the plastic portion of the stress strain curve, is the production of very large numbers of extra dislocations. It is quite normal for the dislocation density to increase between the yield stress and high rolling stresses by more than one million times.

One of the current "hot topics" in materials science is the understanding of the arrangements of groups of dislocations into various forms of boundaries during the deformation process. This is discussed below.

2.2.1 Microstructural aspects of cold deformed structures

A detailed description of the deformed microstructure and the evolution of the microstructure is beyond the scope of this thesis and the following description is limited to the most common features seen in the cold rolled deformation microstructure of aluminium. More detailed information about the evolution of the deformed microstructure can be found e.g. in (Hansen, 1990; Bay, Hansen, Hughes and Kuhlmann-Wilsdorf, 1992; Bay, Hansen and Kuhlmann-Wilsdorf, 1992; Hansen and Juul Jensen, 1999).

During plastic deformation of metallic materials a large number of dislocations are produced, these dislocations dominate the microstructure of the deformed material. The dislocations configure a network of dislocation boundaries separating regions with low dislocation density. The dislocation boundaries can typically be divided into two distinct types, extended planar dislocation boundaries and randomly oriented cell boundaries (Hansen and Juul Jensen, 1999). The two types of boundaries may coexist in the microstructure to form cellblocks, where a number of cells are located between a set of extended planar dislocation boundaries (see figure 2.1). The two types of boundaries may be formed by different mechanisms. Therefore cell boundaries have been termed Incidental Dislocation Boundaries (IDBs) and the extended planar dislocations boundaries Geometrically Necessary Boundaries (GNBs) (Kuhlmann-Wilsdorf and Hansen, 1991).

Figure 2.1 consists of a TEM micrograph and a sketch from the micrograph. The thick black lines in the sketch are GNBs separating cell blocks where IDBs separate cells. It is found that the cellblock size and cell size decreases with increasing strain but the misorientation across GNBs increases (Liu and Hansen, 1995; Hughes, Chrzan, Liu and Hansen, 1997).

The deformed microstructure is dependent on a number of parameters, such as the strain, the strain rate, the deformation type, the temperature, but also the starting grain size and orientations are important(Liu and Hansen, 1995; Hansen and Huang, 1998; Liu, Juul Jensen and Hansen, 1998).

The dislocation-free regions of the microstructure surrounded by low angle dislocation walls are in general referred to as cells or subgrains depending on the boundary morphology, in this thesis the term subgrains will be used.

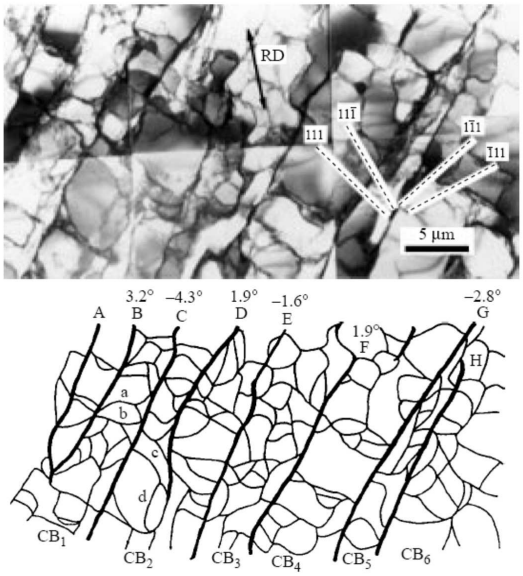

Figure 2.1: *TEM micrograph and sketch of a microstructure in a grain of a 10% cold rolled specimen of pure aluminium (99.996%) in longitudinal plane view (the plane containing rolling and normal directions). Thick lines are GNBs marked A,B,C, etc., which separate cell blocks. Cell blocks are subdivided into cells by IDBs (thin lines). Reproduced from (Liu and Hansen, 1995).*

2.2.2 Subgrain development during deformation[1]

The development of subgrains during the initial stage of deformation has been studied using X-ray diffraction. The experiment was performed at beamline 1-ID at APS.

A grain within a polycrystalline copper specimen with its [100] direction close to the tensile axis was positioned in such a way that a 400 diffraction spot was located on a high resolution detector (as seen in figure 2.2). The X-ray beam was defined by a slit system to a size of 14x14 μm^2.

The individual peaks were identified as diffraction spots arising from individual subgrains within the the grain. Three facts were suggesting this:

[1]This section largely comes from a paper in press titled "Formation and Subdivision of Deformation Structures during Plastic Deformation" by B. Jakobsen, H. F. Poulsen, U. Lienert, J. Almer, S. D. Shastri, H. O. Sørensen, C. Gundlach and W. Pantleon.

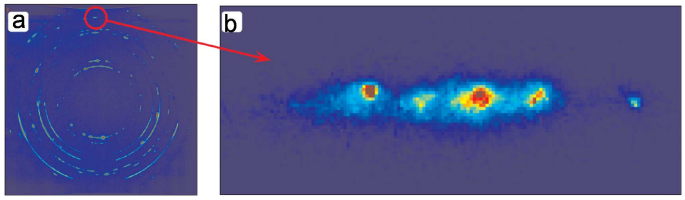

Figure 2.2: Diffraction patter at a strain of 3% (a) Diffraction image with Debye-Scherrer rings completely in the image. (b) High resolution diffraction image of the (400) reflection. Reproduced from (Jakobsen *et al.*, 2006).

1. The size of the diffraction domains calculated from the integrated intensities were found to be 1-3 μm in agreement with TEM measurements.

2. The peaks were sharp in all directions of reciprocal space. Implying the domains to be nearly free of dislocation.

3. The diffraction spots were determined from knife-edge scans to originate from one position within the grain.

In figure 2.2 an enhanced intensity above background level can be seen between the diffraction spots. This cloud of intensity is suggested to be identified as arising from the disordered dislocation boundaries.

Dynamic investigations have shown that the individual diffraction spots can be observed already at tensile strains as low as 0.6%.

2.3 Annealing

Annealing simply refers to warming up a piece of material which has previously been deformed. Annealing is of great technological importance since it permits an engineer to optimise a number of properties. It is possible to make the material more ductile by annealing; however this is at the expense of some strength.

From a scientific viewpoint it is customary to separate annealing into three processes which are listed below. The driving force for the recovery processes is a decrease of the total energy in the crystal:

1. **Recovery**, where properties changes towards the initial values. Also changes are observed in the microstructure. At the end of recovery subgrains are entirely dislocation free.
2. **Recrystallisation**, is a far more rapid process, where a new set of strain-free grains are nucleated which grow through the deformed/recovered material removing dislocations and subgrain boundaries.
3. **Grain growth**, here the energy of the ensemble of grain boundaries drives the system to adopt a coarser grain size with time. The grain growth process has a much smaller driving force than recrystallisation and is therefore much slower.

2.3.1 Recovery

The term recovery covers a set of different processes occurring in the microstructure, the joined result of these processes is a more ordered microstructure. It is possible to identify a number of processes by:

1. The annihilation of excess point defects (vacancies). These are eliminated at:
   (a) the free surface of the sample;
   (b) the grain boundaries;
   (c) dislocations leading to climb of edge dislocations or in the case of screw dislocations to the formation of helical dislocations.
2. the annihilation of many of the dislocations. These are eliminated by:
   (a) moving into the surrounding grain boundaries;
   (b) shrinking back, as loops, into the sources from which they came;
   (c) combining opposite signed dislocations;
3. climbing (using the vacancy absorption described above) to form polygon walls. This process, termed polygonization, creates polygon boundaries which are of low angle and become the subgrain boundaries of the recovered subgrain structure.

The processes described above occur either during deformation as **dynamic recovery** or during annealing as (**static**) **recovery**. Another process in recovery is the growth of subgrains for which two different mechanisms have been proposed:

1. Subgrain boundary migration, where subgrains grow by migration of a LAGB on the expense of neighbouring subgrains.

2. Subgrain rotation and coalescence where the crystal lattice of two subgrains rotates relative to each other in order to decrease the misorientation over a LAGB until the boundary has disappeared.

Both mechanisms are described in more detail in section 2.4.1.

Recovery is a complex process because the deformed microstructure described section 2.2.1 is not homogenous with dislocations homogenously spread out and the selection of the presented processes may vary during annealing.

2.3.2 Recrystallisation

In the technologically more important field of recrystallisation, a completely new set of relatively strain-free grains are generated; often with a completely different set of textural components from those generated by cold working.

Substantial interest in the nucleation process arises from the fact that, elementary calculations suggest that the critical nucleus size is micrometres (rather than atomic scale as for other solid state phase transformations).

A number of nucleation mechanisms and nucleation sites have been proposed. Favoured sites include grain corners (where four grains meet), grain edges (where three grains meet) and grain faces (where two grains meet). Second-phase particles present in the material may induce a local orientation gradient during deformation. Such orientation gradients are a preferred sites for nucleation.

The general view is that a nucleus arises from some local instability of the subgrain structure in the neighbourhood of grain boundaries (and the sites identified in the previous paragraph). Models embracing this idea are the so called strain induced boundary migration model and developments of this model. However, in some important cases (some of which will be discussed later in section 3.4.1) nuclei appear with orientations which were not present in the deformed/recovered structure. Various models involving twinning, multiple twinning and grain boundary dissociation have been suggested for these cases.

2.3.3 Grain Growth

Grain size control is of paramount importance from a property viewpoint, hence the current interest in nanocrystalline metallic materials. Broadly for low temperature strength and fatigue resistance a small grain size is desirable, whereas for resistance to high temperature environments (the creep regime) a coarse grain size (or a single-crystal) is selected. Grain growth models are described in section 2.4.1 in connection with subgrain growth.

2.4 Previous studies of recovery processes

Recovery processes have been studied for more than 50 years, and a wide number of experimental techniques have been used over the years. These techniques can be divided according to the studied elements. Some techniques monitor the material properties (Kuhlmann, Masing and Raffelsieper, 1949), while electron microscopes provide information about the evolution of the microstructure (Friedel, 1964; Hu, 1962; Li, 1962).

Most recovery models either try to model the recovery of some material property (e.g. in (Nes, 1995; Nes and Sæter, 1995; Furu, Ørsund and Nes, 1995)) or the changes in the microstructure (e.g. Li (1962).

It has been suggested that recovery should be treated as one part of a unified theory covering all annealing processes, recovery, recrystallisation and grain growth (Humphreys, 1997a; Humphreys, 1997b; Humphreys, 1999). This model considers an ensemble of subgrains each described by a radius R (with a mean $\bar{R}$) and the type of subgrain boundary, described by misorientation θ, energy γ and mobility $\bar{\mu}$. The model is based on boundary migration which is assumed to be the only important microscopic mechanism.

As described in section 2.3.1 dislocation annihilation and removal of point defects are also processes in recovery. These processes are not the aim of the 3DXRD studies and therefore will not be considered in this section. In this section the focus will be on the different recovery models describing the changes in microstructure on a length scale larger than dislocation annihilation, i.e. subgrain growth. Subgrains grow by either coarsening or coalescence as described below. A study of subgrain growth in order to distinguish between coarsening and coalescence was one of the motivations behind the 3DXRD method developed in this thesis.

2.4.1 Subgrain growth by subgrain coarsening

Subgrain coarsening is based on subgrain boundary migration, that is the boundary between two subgrains migrates thereby changing the orientation of the swept area to the orientations of the growing subgrain.

If the subgrain structure can be approximated by an ensemble of subgrains corresponding to grains in a recrystallised microstructure, the subgrain boundary migration process can be considered analogously to the process of grain growth. Therefore the mechanisms of grain growth are illustrated here for subgrain growth.

Following the analysis by Burke and Turnbull (1952) a parabolic relationship between subgrain (grain) size and time was found for the growth kinetics, is given by (Atkinson, 1988):

$$\overline{R_t}^2 - \overline{R_0}^2 = Kt \tag{2.1}$$

where $\overline{R_t}$ and $\overline{R_0}$ respectively are the mean subgrain size at time t and the initial mean subgrain size, K is a constant dependent on the subgrain boundary energy γ, which is assumed equal for all subgrain boundaries, and boundary mobility μ, and independent of subgrain size and time. Included in K can also be a shape related factor. Equation (2.1) is derived based on boundary migration, caused by curvature forces. The velocity v is given by:

$$v = \mu P \tag{2.2}$$

where μ is the subgrain mobility and P the driving pressure, given by:

$$P = \gamma \left(\frac{1}{r_1} + \frac{1}{r_2} \right) \tag{2.3}$$

where r_1 and r_2 are the main radii of the surface curvature. Approximating the boundary to part of a sphere, $r_1 = r_2 = r$ and assuming proportionality to the mean radius of an individual subgrain ($r \propto R$), the change in subgrain radius over time becomes:

$$\frac{dR}{dt} = v = 2\mu\gamma \left(\frac{1}{R} \right) \tag{2.4}$$

from which equation 2.1 can be obtained for the average. In the limit where $\overline{R_t}^2 \ll \overline{R_0}^2$ equation 2.1 is rewritten in a general from as:

$$\overline{R_t}^2 = Kt \tag{2.5}$$

$$\overline{R_t} = Kt^{1/n} \tag{2.6}$$

where n is often termed **grain growth exponent**, here $n = 2$.

In the theory described above the only microstructural parameter is the average subgrain size. Other theories called **mean field theories**, take the change in subgrain sizes of an ensemble of subgrains into account. Mean field theories are statistical theories based on grain size distributions. These theories can be divided in two groups focusing on either drift (**drift models**) or diffusion (**diffusion models**, not discussed in this thesis) of the flux of grain sizes. The basis of drift models are subgrain size distributions $f(R)$, and dynamics where grains larger than a critical size R_C will grow and grains smaller than R_C will shrink.

One example of a drift model was developed by Hillert (1965). The basic idea was that given an expression for the drift velocity $v = \frac{dR}{dt}$ the grain size distribution $f(R, t)$ could be found, using:

$$v = \frac{\mathrm{d}R}{\mathrm{d}t} = \alpha\mu\gamma\left(\frac{1}{R_C} - \frac{1}{R}\right) \tag{2.7}$$

where α is a geometric factor, Hillert obtained parabolic kinetics similar to equation (2.1).

Another expansion of the growth models is the introduction of orientation-dependent grain boundary energies and mobilities in the model. Abbruzzese and Lücke (1986) built on Hillert's model, by a assuming a growth rate of neighbouring grains given by:

$$\left(\frac{\mathrm{d}V_\nu}{\mathrm{d}t}\right)_\mu = s_{\nu\mu}m2\gamma\left(\frac{1}{R_\mu} - \frac{1}{R\nu}\right) = Ms_{\mu\nu}\left(\frac{1}{R_\mu} - \frac{1}{R_\nu}\right) \tag{2.8}$$

where μ and ν are indices of neighbouring grains, V and R are respectively volume and radius of a grain, $s_{\mu\nu}$, m, γ and $M = 2m\gamma$ is the grain boundary area connecting grain μ and ν, the mobility, the tension and the diffusivity of the grain boundary $\mu\nu$. Grains are then groupped according to their sizes (i) and orientations (H) in grain classes of (i, H).

In Abbruzzese and Lücke's (1986) model it was shown that in a textured microstructure each orientation class has its own critical radius. This critical radius depends not only on the grain size distribution of its own orientation but also on the distributions of the other orientations classes.

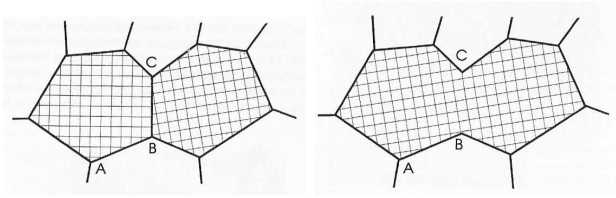

(a) (b)

Figure 2.3: *Coalescence schematic. (a) situation before coalescence. (b) One subgrain has rotated into the same orientation of the other subgrain. Reproduced from (Humphreys and Harherley, 1995).*

Subgrain growth by subgrain boundary migration is a continuous mechanism. An *in-situ* study of subgrain sizes would result in smooth continuous growth curves, increasing for the growing subgrains and decreasing for the disappearing subgrains.

2.4.2 Subgrain coalescence

An alternative mechanism for subgrain growth was proposed by Hu (1962). The mechanism involves two neighbouring subgrains. The subgrains rotate in orientation until the two subgrains are of the same orientation, at which point the two subgrains would coalesce into one subgrain. The driving force arises from a reduction in boundary energy, as discussed by Li (1962). A schematic of the mechanism can be seen in figure 2.3.

If the misorientation across boundary BC is smaller than the misorientation across boundary AB, a rotation of the orientation of one of the subgrains decreases the misorientation across boundary BC by $\Delta\theta$ and simultaneously increases the misorientation across the boundary AB by the same amount, x°. The boundary energy γ_s is given by the Read-Shockley equation (Read and Shockley, 1950):

$$\gamma_s = \gamma_0\theta(A - \ln\theta) \tag{2.9}$$

The change in boundary energy $|\frac{d\gamma}{d\theta}|$ is larger at low angles. Therefore it is energetically favourable for the system that the subgrains rotate in the way leading to coalescence. Evidence of coalescence has been widely reported from TEM studies (Faivre and Doherty, 1979; Jones, Ralph and Hansen, 1979; Doherty and Szpunar, 1984).

The subgrain coalescence can be seen as a discontinuous mechanism, an *in-situ* 3DXRD study of subgrain sizes would result in discontinuous curves, with jumps in measured sizes when coalescence occurs.

2.5 Techniques employed previously to study recovery processes

A number of experimental techniques can and have been applied to study the different annealing processes. In this section some of the techniques used to study the recovery processes will be presented.

All the different techniques that can be applied to study annealing processes can be divided into two classes;

- techniques that measure changes in the different properties of the metallic material;
- techniques that monitor the evolution of the microstructure.

During the heat treatment of metallic materials the processes described above involve the release of stored energy as heat. The change in stored energy can be monitored by calorimetry. The elimination of vacancies and the annihilation of dislocations that occur during the recovery process may be followed by monitoring the change in electrical resistivity. The main change in hardness occurs during the recrystallisation processes but a small change can be seen during the recovery processes also.

Many forms of microscopes have been used to study annealing processes and how the different annealing processes have changed the microstructure. A large portion of the information gained on structural changes were obtained with the use of TEM. With the TEM it is possible to follow the evolution of the dislocation structures. The drawback of TEM is that it operates in transmission and due to the stopping power of electrons by materials the sample thickness in practice has to be no more than 1 μm. Orientation contrast in different grains can be seen with an optical microscope, and this may be used to study grain sizes. With the development of Electron Back-Scatter Diffraction (EBSD), an extension technique in the SEM, a new method to characterise microstructures came into play. EBSD can be used to study orientations of many surface grains in a short time.

For this thesis a few of these methods have been used to provide an overview of the structure and the rate of the dynamics related to the material in question.

2.5.1 Electron microscopy

As described above electron microscopy is divided into two classes, TEM and SEM. The description of the technique of TEM is not within the scope of this thesis, but a short description of the EBSD method follows below.

In an SEM a finely focussed electron beam, which can be focussed down to 20 nm, scans the surface of the specimen (Haasen, 1996). Information is gathered from a volume close to the sample surface, the region from where backscattered electrons can escape the sample again. The depth of the region of information depends on the energy of the electrons and the sample material.

When the electron beam enters a crystalline sample, some electrons will be inelastically scattered in all directions. Some electrons will have an angle of incidence with the atomic planes in the crystalline sample that fulfill the Bragg law:

$$2d_{hkl} \sin\theta = n\lambda \tag{2.10}$$

where θ is the Bragg angle, d_{hkl} is the interplanar spacing for the crystal planes with Miller indices *hkl*, and λ is the electron wavelength. Electrons that fulfill the Bragg law are elastically scattered into two diffraction cones. Because the Bragg angles of electrons are low ($\sim 0.5^\circ$) the two cones appear as lines on a two-dimensional detector instead of hyperbolaes. These lines are called backscattered Kikuchi lines. Each pair of Kikuchi lines are diffracted from one set of *hkl* crystal planes in the specimen. The Kikuchi lines contain the information used by EBSD method. The information from the lines are extracted from the recorded images by a Hough transformation (Hough, 1962). When several pairs of Kikuchi lines are obtained and the Miller *hkl* indices found for the same position, the crystal orientation of the region hit by the electron beam can be determined (Lassen, Juul Jensen and Conradsen, 1992).

EBSD takes advantage of the fact that the combination of the scanning and a focussed beam yields information from a limited surface area. In this way the crystal orientation can be found in small regions while scanning the surface. The result is e.g. an orientation map. An example of this can be seen in chapter 5 figure 5.4.

2.5.2 Measurement of Hardness

Classic mechanical measurements of the softening of metals achieved after annealing are hardness tests. Hardness is the resistance of a material against being penetrated by another material with a higher hardness. A hardness test involves deformation and the ability to deform is dependent on the number of dislocations and the mobility of the dislocations. There exists a number of different hardness tests, the main difference is the shape of the indentation object. Vickers hardness indentations were used in the hardness investigations in this thesis. An example of the output achieved is given in figure 5.2.

The Vickers hardness indenter is a diamond indenter in the shape of a pyramid with a square base. The angle between two opposite faces of the pyramid is 136°. The indenter is forced into the material surface with a load between 1 and 100 kg, the time duration of the unloading is typically 10 to 15 seconds. After loading an indentation with the squared form of the indent is left in the surface, the size of this indentation can be measured with the use of an optical microscope.

The Vickers hardness is determined by the load and the area of indentation, which is calculated from the mean of the two diagonals in the square form. The relation is given as:

$$H_V = \frac{2L \sin \frac{136^\circ}{2}}{d^2} \tag{2.11}$$

where L is the load and d is the mean diagonal (Tabor, 2000). The accuracy of the hardness measurement is dependent on the optical measurements of the diagonals, therefore sample surfaces are normally pre-polished.

Chapter 3

Experimental Methodology

The main aim of this project has been to extend the use of the 3DXRD microscope to a study of subgrains in the microstructure of metals. The main interest is in the evolution of the volume of the subgrains, which means growth curves of individual subgrains. This problem is very closely related to a different use of the microscope, the study of recrystallisation by means of growth curves. There will be no spatial information on where the individual subgrains are located within the material.

This chapter on experimental methodology is divided into three parts. These parts reflects the basis of the experimental work involved in this thesis. The first part reviews the basis of 3DXRD methods: diffraction geometry, the 3DXRD microscope itself including the optics and detectors. The second part — sections 3.2 and 3.3 — considers the issues related to the 3DXRD method being applied to a study of recovery. The idea behind the experiments performed as well as the problems related to the experimentation will be described. The final part of the chapter discusses two other 3DXRD annealing experiments, closely related to the topic of recovery. The first experiment examines the nucleation of recrystallisation in deformed copper, while the second experiment examines the recrystallisation of aluminium.

3.1 3DXRD in general

This thesis is based on work carried out on the 3DXRD microscope. The 3DXRD microscope is developed collaboratively by the European Synchrotron Radiation Facility (ESRF) and the Material Research Department at

Risø (Poulsen, Garbe, Lorentzen, Juul Jensen, Poulsen, Andersen, Frello, Feidenhansl and Graafsma, 1997; Poulsen, 2004). The microscope is implemented at beamline ID-11 at ESRF.

The 3DXRD microscope is normally operated in the hard X-ray region of 50 keV to 100 keV. In this energy range the X-rays can penetrate up to 4 cm of aluminium.

The microscope is aimed at *in-situ* studies of structural dynamics of hundreds of individual bulk grains in a polycrystalline material when applying stress or heat, or a combination thereof, to the material. The structural properties of interest are: the volume of the grains, the position of grains within the material, the average crystallographic orientation for each of the grains, the average elastic strain tensor for each of the grains and the 3D morphology of the grains.

The microscope can operate in two different configurations depending on the aim of the study:

Orientation configuration is with a low spatial resolution detector positioned at a medium-to-large distance from the sample. This distance depends on how many Debye-Scherrer rings are needed on the detector. In this configuration information is acquired on crystallographic orientations, the volumes and the elastic strain of the grains in the sample.

Tracking configuration is with a high spatial resolution detector positioned close to the sample. Data acquisition is repeated at different sample-detector distances. Spatial information, such as grain morphologies are extracted from the diffraction data by an X-ray tracking algorithm, to be further discussed below in section 3.1.9.

3.1.1 Diffraction theory

When a monochromatic X-ray beam is incident on a crystal, the X-ray beam is scattered from all atoms in the crystal. The diffracted X-rays will interfere and can be observed in directions of constructive interference. This phenomenon was observed and described by Bragg and Bragg in 1913 and Bragg's law is the governing equation of diffraction theory:

$$2d \sin\theta = n\lambda \tag{3.1}$$

where θ is the diffraction angle, λ is the X-ray wavelength, n is an integer and d is the distance between the diffracting lattice planes of the crystal.

The distance between crystal lattice planes *hkl* in a cubic crystal is given by:

$$d_{hkl} = \frac{a}{\sqrt{h^2 + k^2 + l^2}} \tag{3.2}$$

where a is the lattice constant.

The X-ray wavelength λ is given by:

$$\lambda[\text{Å}] = \frac{hc}{E_{photon}} = \frac{12.398 \text{ Å keV}}{E_{photon}} \tag{3.3}$$

where E_{Photon} is the X-ray energy.

A more general description of diffraction theory can be found in many books such as (Warren, 1990) and (Als-Nielsen and McMorrow, 2001).

3.1.2 Implementation of 3DXRD at ID11, ESRF

The layout of the 3DXRD microscope is shown in figure 3.1. In this figure the synchrotron white beam is entering the experimental hutch from the right.

Initially, the white beam passes through a small optics box containing a Laue crystal and a multilayer (LC and ML in figure 3.1). The optics are described in detail in section 3.1.4. Leaving the optics box is a tilted monochromatic beam. Next the beam encounters a double slit system that can be used to define the size of the beam and/or cut down on tails from the beam (the position of the slit system is shown in figure 3.2).

The sample environment is located on a sample stage designed to carry a weight of 200 kg. The sample stage consists of horizontal (x, y)-translations, parallel and perpendicular to the X-ray beam, respectively. On top of this translation stage is a tilt stage used to align the rotation axis perpendicular to the X-ray beam. A ω-rotation stage is located on the tilt stage. Finally a second (x, y)-translation stage is placed on the rotation stage on top of which a z-translation device (not shown in figure 3.1) is placed in order to move the sample up and down through the X-ray beam. The (x, y)-translations are used to move the sample, while keeping the rotation axis centred in the X-ray beam. Definitions of (x, y, z, ω) can be seen on figure 3.2.

Behind the sample environment stage is a transverse arm on top of which three z-elevators are mounted. These are used for different detector configurations. The high-resolution detector is mounted on one of the elevators.

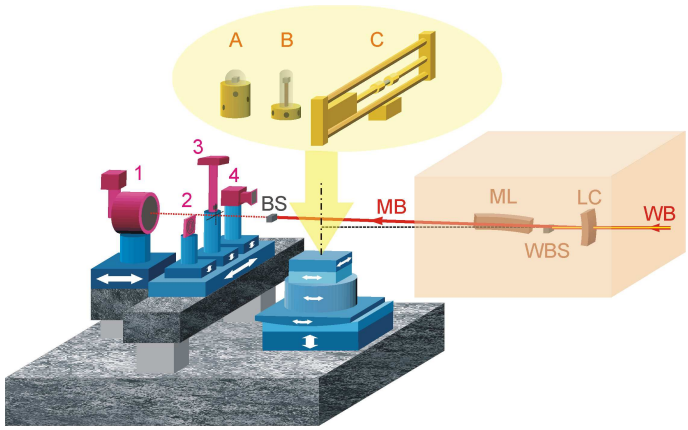

Figure 3.1: *Overview of the 3DXRD microscope. A combination of different elements can be used in the setup of the 3DXRD microscope. 1 is a Frelon detector, a large area detector used for orientation measurements. 2, 3 and 4 are high resolution detectors and a conical slit. On top of the rotation stage different sample environments can be selected: A is a cryostat, B is a furnace and C is a stress rig. WB is the incoming white beam, LC is the Laue crystal used to monochromate the X-ray beam, WBS is a beamstop blocking the white beam, ML is a multilayer, MB is the monochromated X-ray beam and BS is a beamstop shielding the detectors from the monochromised X-ray beam. Arrows mark translations and rotations. Courtesy of R. V. Martins.*

Other tools on this arm are a photodiode used to characterise the beam, and a conical slit. The conical slit is an optics element that ensures bulk measurement of millimetre thick samples (Nielsen, Wolf, Poulsen, Ohler, Lienert and Owen, 2000). It is a metal disc with openings (slits) that are arcs allowing parts of the diffracted Debye-Scherrer rings to pass though. The heights of these openings define a gauge volume in the sample from where the diffracted beams are allowed to pass through the slits. The elevators are mounted on a motorised block with a translation facility along the y-axis. In this way a shift between different configurations can be made without entering the experimental hutch.

The arm parallel to the incident X-ray beam is used to position the low-resolution detector (1 in figure 3.1) at an optimised distance from the rotation axis. This arm (not shown in figure 3.1) can be rotated 10° around the ω-rotation axis .

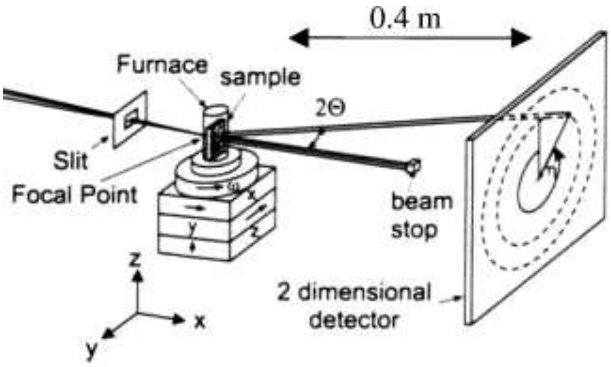

Figure 3.2: *A possible setup of the 3DXRD microscope in the orientation configuration, with the focusing optics (Bent Laue crystal and multilayer), a slit system and the sample positioned in the focal point. In some experiments the sample is positioned behind the focal point in the direction of the X-ray beam. The coordinates x, y, z, ω, η and 2θ are defined on the sketch.*

3.1.3 X-ray source

With a synchrotron source X-rays are produced with bending magnets or by insertion devices: wigglers and undulators.

The bending magnet is the classical device which is used to bend and lead the electrons in their path in the synchrotron. X-rays are produced when the electrons are accelerated in the bending magnet. Since the electrons are accelerated all the way though the bending magnet, X-rays are generated in a fan from the bending magnet.

More intense X-rays are produced by the wigglers and undulators, which are located on the straight sections at the synchrotron. An insertion device consists of arrays of magnets with opposing polarity, which forces the electrons into a sinusoidal path through the insertion device. In an undulator the X-rays emitted at one arc of the path are in phase with X-rays emitted from the following arc which makes the interference constructive, making the X-ray beam more intense.

The high energy X-rays at the 3DXRD microscope are produced by an in-vacuum undulator. An experimental undulator spectrum of the in-vacuum undulator at ID-11 taken at a motor gap (the distance between the two arrays of magnets in an undulator) of 8 mm is shown in figure 3.3.

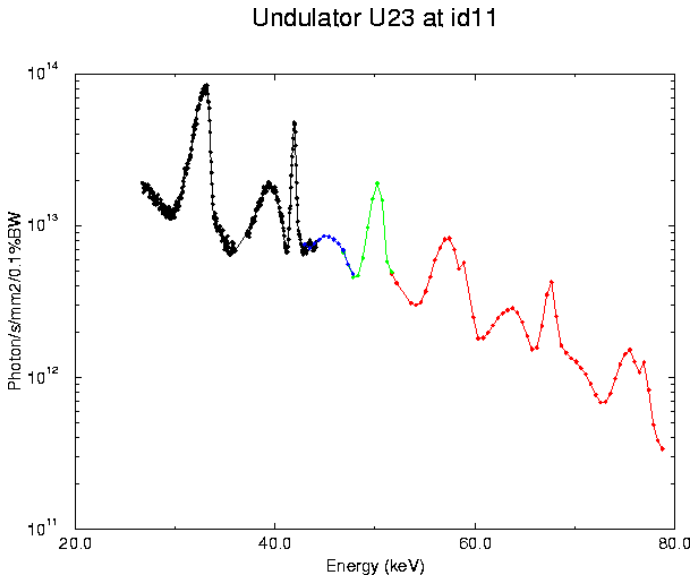

Figure 3.3: *Experimental undulator spectrum from the ID-11 undulator, measured at a gap of 8 mm. The vertical axis is the brilliance of the X-ray source, the standard way to characterise the intensity of the X-ray beam. Brilliance is defined as the number of photons per second per mrad^2 (how much the beam diverges) per mm^2 (of source area) per 0.1% (of the monochromator) bandwidth.*

3.1.4 Optics

The optics box of the 3DXRD microscope contains two optical elements that monochromate and focus the incident white beam.

The first element is an asymmetrically cut, cylindrically bent perfect silicon crystal, which is used in transmission mode (Schulze, Lienert, Hanfland, Lorenzen and Zontone, 1998). This so called Laue crystal monochromates the X-ray beam and focuses it in the vertical direction using the (111) plane of the silicon crystal. The second optical element is an elliptically-shaped, laterally-graded multilayer made of W and B_4C and used in reflection mode (Lienert, Schulze, Honkimäki, Tschentscher, Garbe, Hignette, Horsewell, Lingham, Poulsen, Thomsen and Ziegler, 1998) which is used for focusing the X-ray beam horizontally.

By focusing in both the vertical and horizontal dimensions and relaxing the bandpass to 0.1% an increase in peak flux in the order of 10^5 is obtained compared to standard optics used in condensed matter physics such as a Bragg-Bragg monochromator made of perfect flat Si crystals.

The optics is constructed such that it can produce three different types of incident X-ray beam. These three types of beam are: (1) a line beam where the beam has been focused in the vertical direction. (2) the second type of incident beam is a box beam, which has dimensions larger than the scattering domains of interest, typically dimensions are from 5×5 μm^2 to 100×100 μm^2. (3) the third type of beam is just like the box beam but smaller than the scattering domains and is therefore called a pencil beam, a typically size is 2×5 μm^2.

3.1.5 Sample environment

The 3DXRD microscope can be used with several sample environments depending on the aim of the experiment. These include a furnace which can operate up to 1000°C. In the furnace the sample is mounted on a copper rod, where a thermocouple is mounted close to the sample. The sample is surrounded by a glass tube which can be evacuated or filled with a gas. This provides a stable sample surrounding. The glass tube is formed into different shapes depending on the sample size. This enables the high-resolution detector to be as close as 4 mm from the sample rotation axis. For deformation studies a specially-designed 25 kN tensile stress rig is available. Finally, a cryostat is available for cryogenic studies.

3.1.6 Detectors

Different detectors are used in different configurations of the 3DXRD microscope. Two types of Charge-Coupled-Device (CCD) detectors are used.

A Frelon 14 bit 2D CCD detector is used to record diffraction images with a medium resolution. This detector consist of a 160x160 mm^2 fluorescent phosphor screen.

When the X-rays hit this fluorescent screen some photons are absorbed generating visible light. The visible light is then transformed into electrons in an image intensifier. The image intensifier also focuses the electrons to an area of the same size as the CCD-chip. Finally the electrons are transformed

into light which is transmitted to the CCD-chip. The detector exhibits anti-blooming. This is a technique which limits any electric charges over flowing the charge wells associated with the most intensely illuminated pixels in the CCD to the neighbouring well. This technique lowers the dynamic range to 14 bits. The detector is a 1024x1024 pixel detector with an effective pixel size of 175×175 μm^2. The fluorescent phosphor screen and camera optics will spread out the photons giving the effective pixel size. The spatial resolution on this detector is defined by the point-spread function, which is between 200 and 300 μm. The readout time of this detector is 0.2 seconds[1]

A Quantix 12-bit CCD detector is used to record high resolution diffraction images. This detector has a pixel size of 2.3×2.3 μm^2, this is the effective pixel size after the phosphor screen and camera optics[1]. This resolution is so good that the outline of a diffraction spot on the detector can be assumed to be an approximate projection of the outline of the diffracting grain, if no broadening of the diffraction spot from the grain is assumed.

3.1.7 Data collection - acquisition sweep

Two oscillation routines (the step-scan and sweep-scan) have been developed to ensure a fast and uniform sampling of the diffraction space. Both are synchronised with the opening and closing of a shutter, such that exposures are made exactly during the periods where the sample is rotated $\Delta\omega$ with a desired constant rotation velocity. The overall difference between the two routines are that one functions in steps of rotations and the other functions in two sweeps of rotations.

3.1.7.1 Step-scan

The rotation interval of the step-scan routine is defined by the initial ω value (ω_i) and the final ω value, (ω_f). During each exposure the sample is rotated from $\omega_j - \Delta\omega/2$ to $\omega_j + \Delta\omega/2$, where $\Delta\omega$ is the requested integration interval and ω_j is an incrementing value from ω_i to ω_f. With the use of the step-scan one image per three seconds can be acquired(Poulsen, 2004).

[1] http://www.esrf.fr/UsersAndScience/Experiments/MaterialsScience/ID11/ID11Detectors/

3.1.7.2 Sweep-scan

A newer developed ω-scan routine is the sweep-scan where all images are acquired in two rotation sweeps. ω_i and ω_f are still the initial and final ω positions of the sample and $\Delta\omega$ is the requested integration interval for each acquired diffraction image. During one rotation from ω_i to ω_f a series of exposures are made while the rotation are synchronised with the shutter in such a way that every second $\Delta\omega$ range is exposed. The holes left in the ω range of interest are measured during a second rotation. The frequency of this routine is four images per second.

The difference in frequency between the step-scan and the sweep-scan is due to the many movements and accelerations of the rotation motor in the step-scan.

3.1.8 Diffraction image - detector readout

The detectors produce two dimensional images of different sizes depending on the detector. Figure 3.4 shows an example of the image from the Frelon detector with the setup used for the recovery studies in this thesis. In the figure arcs of Debye-Scherrer rings are clearly visible. The image also has a number of artifacts, the glass on the furnace give raise to amorphous scattering, this scattering is strongest in the centre of the image and can be seen in region (3). In region (3) an area is also present where no scattering hits the detector due to a beamstop. The amorphous scattering is spread out through the image, but a difference is observed between region (2) and the rest of the image, this difference is due to shadowing from the sample holder. The sample holder absorbs part of the amorphous scattering but the sample holder is not shadowing region (2). Finally a slit in the slit system was hit by the X-rays giving scattering in region (1).

3.1.9 GRAINDEX

An algorithm for sorting and indexing the diffraction spots with respect to a grain of origin has been developed in house (Lauridsen, Schmidt, Suter and Poulsen, 2001). This algorithm, GRAINDEX, can be applied to both the tracking and the orientation configurations. The important parts of the algorithm will be described below.

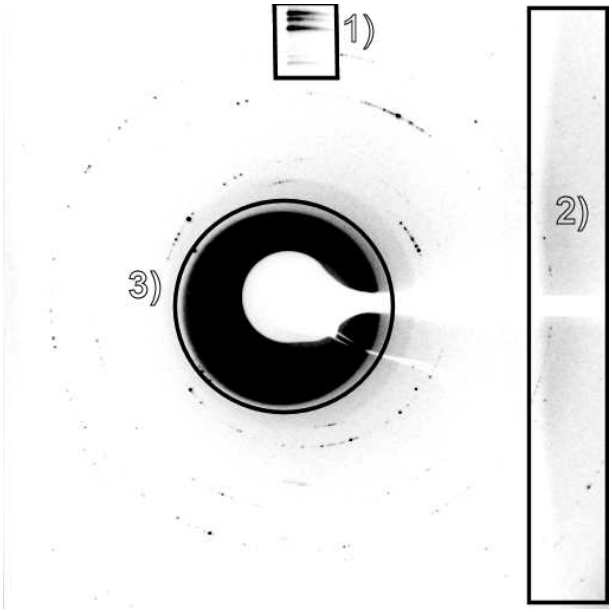

Figure 3.4: *An example of a raw data image acquired on the Frelon detector, where the image intensity is inverted. The material is AA1200 alloy (described in section 5.2.2). Most of the diffraction spots can be found on arcs of the Debye-Scherrer rings. A number of artifacts can be also seen on the image, these are: (1) scattering from the slit system, (2) The difference between the background in area (2) and the rest of the image is due to the sample holder absorbing the amorphous scattering from the furnace glass. (3) The black area within the inserted black circle is due to amorphous scattering from the glass. The white area is due to the beamstop in front of the detector.*

Diffraction spots are identified in the detector images by setting and applying a commercial "blob"-finding routine. Blobs located at the same image pixel in neighbouring ω-bins are grouped together as one blob. The integrated intensities of such blobs are scaled with a Lorentz factor.

The next step is the X-ray tracking. A diffraction spot from a particular grain will appear at the same θ-η-ω positions at different sample-detector distances. This can be used to back track the diffraction spot to the grain position in the sample.

The diffraction spots are sorted according to their grain of origin. This is done by a sorting algorithm based on scanning the 3D orientation space. Scattering vectors are simulated for each orientation. If there is a match between simulated diffraction spots and experimentally-found diffraction spots according to various criteria, a grain is identified and logged. Note that the orientations of the indexed grains are produced automatically by the algorithm.

This algorithm has successfully been applied to studies of recrystallisation (Lauridsen, Poulsen, Nielsen and Juul Jensen, 2003), grain rotation (Margulies, Winther and Poulsen, 2001) and two dimensional grain maps (Poulsen, Nielsen, Lauridsen, Schmidt, Suter, Lienert, Margulies, Lorentzen and Juul Jensen, 2001; Nielsen, 2000).

3.1.10 3D grain maps

One next step could be to make grain maps in three dimensions. This can be done by using the microscope in the tracking configuration with the high resolution detector close to the sample and illuminating the sample with a line beam.

The measurement procedure is repeated stepwise with the specimen translated in the z-direction, scanning layers of the sample. By making a grain map of each layer, a 3D space-filling grain map can be constructed; an example from Fu, Poulsen, Schmidt, Nielsen, Lauridsen and Juul Jensen (2003) is shown in figure 3.5.

3.2 Growth curve studies of recrystallisation

One well-established use of the 3DXRD microscope is the study of the change in volumes of individual grains during heat treatments. This has been used for studying recrystallisation (Lauridsen, Juul Jensen, Poulsen and Lienert, 2000; Lauridsen *et al.*, 2003) and to study phase transformations in steel (Offerman, Dijk, Sietsma, Grigull, Lauridsen, Margulies, Poulsen, Rekveldt and van der Zwaag, 2002). A review of the essential parts of 3DXRD methods to study volume changes of individual grains follows below.

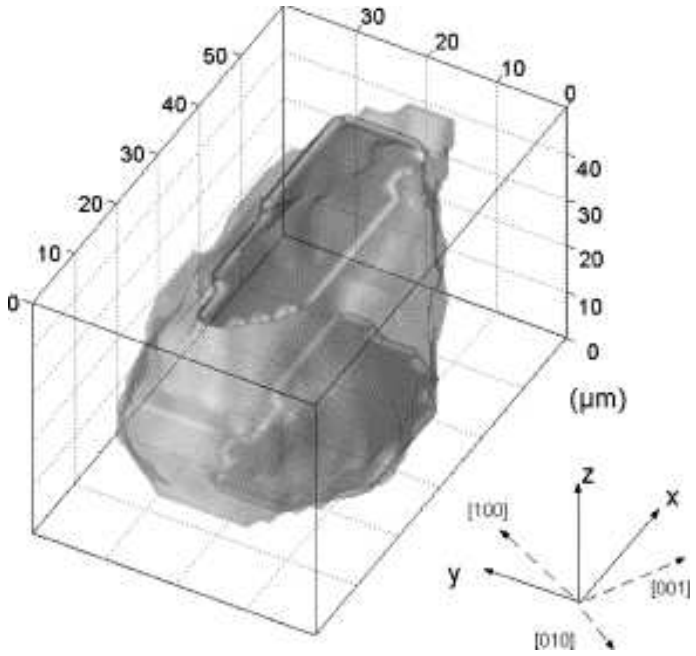

Figure 3.5: *A 3D grain map generated by serial stacking of layers. The grain are reconstructed by applying an algebraic reconstruction technique. Reproduced from* (Fu *et al.*, 2003).

3.2.1 Experimental setup

The experimental setup used in the two experiments by Lauridsen *et al.* (2000) and Lauridsen *et al.* (2003) involved the microscope in the orientation configuration (see section 3.1) with a uniform 100 by 100 μm^2 beam defined by a slit system. The diffraction images of the deformed state were broad arcs on the Debye-Scherrer rings. After annealing sharp distinct diffraction spots started to appear, which corresponded to the emerging new grains.

The sample was 1000 μm thick in the beam direction. This thickness of the sample was much larger than the grain size, and thereby ensured the fraction of surface grains to be negligible compared to the fraction of bulk grains.

The sample was kept fixed in the beam according to the axes x, y, z and rotated in ω, see figure 3.2 in N equidistant steps using either the step-scan (see section 3.1.7.1) or the sweep-scan (see section 3.1.7.2). The use

of the Frelon CCD detector, which has a small readout time, meant that the rotation time was limiting in terms of the time-resolution. This type of experiment has a time-resolution of a few seconds.

Due to various relaxation phenomena there can be positional drifts of the sample. To correct for these and ensure that the same area of the sample was illuminated during the experiment, external markers on the sample were used. The external markers were 300 nm thick gold markers, which had been deposited with a lithographic technique before the 3DXRD experiment. The position of the gold markers were monitored by X-ray fluorescence with an accuracy of 1 μm.

3.2.2 Validation

To verify that a measured grain was fully illuminated by the beam at all ω-positions a validation procedure was developed for this type of experiment. The validation was done by opening the slit system, thereby making the beam bigger. This gives two types of diffraction spots, one where the diffracted intensity does not change and one where the diffracted intensity increased. The first case means that the corresponding grain was fully illuminated. The latter case means that the diffracting grain was only partly illuminated at a tight slit setting; these diffraction spots were rejected. A second validation criteria rejects all diffraction spots which appeared in two or more neighbouring ω-bins.

3.2.3 Volume calibration

The determination of the size (volume) of the grain was the overall main point of the experiment because the volume measurements at different annealing times gave a picture of the growth kinetics, in this case the recrystallisation dynamics and activation energies.

The volume was found by calibrating the integrated intensity of an associated diffraction spot with the integrated intensity from a known gauge volume of a known material. As a reference, a foil of aluminium of known thickness and with nearly random texture was placed in the beam and a rotation measurement was made. This produced a powder diffraction pattern from the gauge volume of the foil. The gauge volume is the thickness of the foil times the dimensions of the beam. The oscillation at each rotation position was a few degrees and with exposure times of a few seconds to

achieve an even sampling and a powder diffraction image as homogeneous as possible.

A scaling factor between the intensity (I^{gauge}) from the foil of known volume (V^{gauge}) and the intensity (I^{grain}) from the diffraction domain of unknown volume (V^{grain}) could be found. Given the expressions for total diffracted intensity in the powder case and in the case of diffraction from a single domain, this scaling factor is given by (Lauridsen *et al.*, 2000; Lauridsen, 2001):

$$V^{grain} = \frac{\omega t}{4} \frac{m_{hkl}^{gauge} |F_{hkl}^{gauge}|^2}{|F_{hkl}^{grain}|^2} \frac{|\sin \eta| \sin 2\theta_{hkl}^{grain}}{\sin \theta_{hkl}^{gauge}} \frac{I^{grain}}{I^{gauge}} V^{gauge} \tag{3.4}$$

where m_{hkl}^{gauge} is the multiplicity of the integrated *hkl*-ring of the powder pattern, F_{hkl}^{gauge} and F_{hkl}^{grain} are the structure factors given for the gauge foil and the sample respectively, θ_{hkl}^{gauge} and θ_{hkl}^{grain} are the corresponding Bragg angles, ω is the rotation velocity and t is the acquisition time.

In the remaining part of this thesis "size" will refer to Equivalent Sphere Radii (ESR) and not to the volume of the subgrains.

3.2.4 Limitations

All experimental setups have their limitations and this is also the case for the present setup. One issue is the time resolution versus the crystallographic orientational accuracy. A large number of narrow ω-bins are necessary to achieve a high accuracy in the orientation, which means a longer acquisition time for each rotation. This produces longer time periods between two diffraction images of the sample at the same ω position which yields a poorer time resolution. During these dynamic studies the time resolution is the most important factor and therefore a small ω range is normally used during each experiment.

Another limitation to consider is the smallest size of the scattering domain that could be detected. The diffracted X-rays have to be intense enough to be seen on the detector as a signal above the noise of the detector. This signal-to-noise ratio varies from experiment to experiment depending on the number of photons hitting the scattering domain.

3.3 Growth curve studies of recovery

The use of the 3DXRD microscope to study recovery aims at studying the evolution of individual subgrain volumes as a function of annealing time. The growth curve study for recovery is almost similar to the one made in recrystallisation. The main difference is the size of the objects studied. Since the subgrains normally are below a few μm in size some issues need to be reconsidered.

3.3.1 Studies of foils

In the work on recrystallisation by Lauridsen (Lauridsen *et al.*, 2000; Lauridsen *et al.*, 2003) a sample volume of 100x100x1000 μm^3 was illuminated. Assuming that the typical subgrain volume is 5 μm^3 then 2 million subgrains exist within the illuminated area corresponding to a powder sample, and consequently observation of individual subgrains cannot be expected.

In order to observe distinct spots from individual subgrains it is therefore necessary to cut down the number of illuminated subgrains. This can be accomplished by making the illuminated sample volume smaller. An easy way to obtain smaller sample volumes is by reducing the sample thickness; in other words to study foils.

In many experiments using the 3DXRD microscope the ideal sample thickness is considered to be 10 times the size of the individual scattering domain of interest. This sample dimension is roughly the minimum thickness where the scattering domains in the centre continues to exhibit bulk properties.

In the case of recovery with a subgrain size around 1-2 μm this means that the minimum foil thickness is 10-20 μm. To produce foils of this thickness with the desired deformation turned out to be challenging. At Risø there is extensive experience of making TEM sample foils, and this was the solution used. In the first 3DXRD experiment (see section 5.1) a TEM sample foil was made in the standard way. The foil was made from a 3 mm circular disk with a thickness of 100 μm, which is electro-polished until visible light can just be transmitted. The resulting foil now has a near parabolic thickness profile with a hole in the centre and a large area where the foil is thin (Christiansen, Bowen and Lindbo, 2002).

The unknown shape of the sample (TEM sample foil) is a weak point in this study. As described the ideal sample would be 10-20 μm thick with the surface planes parallel to each other. In making a TEM sample foil the aim is to ensure an area in which the thickness is $\leq$ 1 μm. The gradient of the parabolic thickness profile is the interesting part in the search for a procedure to fabricate a useful sample for the 3DXRD experiment. If the gradient is small the surface planes are nearly parallel. Because the profile is parabolic the gradient is smaller in the centre of the foil than on the edge. The goal would then be to stop electro-polishing when the thickness is the desired 10-20 μm in the centre of the foil. This has been attempted, assuming linear time dependence with the depth of the electro-polishing. Discs of the same thickness were electro-polished and the time just to make a hole in the centre of the disc was measured. It was then tried to electro-polish discs to the desired thickness. These foils were studied using the 3DXRD microscope and it was concluded that the thickness was much higher than expected as there were severe spot overlapping in the Debye-Scherrer rings. Consequently, this approach could not be used.

One suggested method to examine the thickness profile was by SEM, using the electron beam to "pollute" the sample with carbon in a line. After carbon pollution of the sample, the sample was tilted. In SEM this carbon line would not be a straight due to different heights. Empirically it was found to be not possible to describe the profile using this method.

The thickness of the used foils remained a problem, and the final method to evaluate the thickness eventually was the use of Focused Ion Beam (FIB). In this method a hole next to the area subjected to 3DXRD measurements is sputtered using the FIB. Tilting the foil then makes it possible to measure the height of the sputtered hole. This method has been used to measure the thickness of the foil used in one 3DXRD experiment (see section 5.14).

3.3.2 Microbeam and optics

Cutting the sample thickness down to 10 μm only reduces the number of subgrains in the beam by a factor of hundred. Another factor of hundred can be obtained by reducing the beam size to 10×10 μm^2. This may be achieved by the use of a slit system (see figure 3.2). However, this procedure will reduce the number of photons emerging from the diffraction domains and thereby deteriorate the signal-to-noise ratio.

A better way of reducing the beam size is by micro-focusing the beam. This can be done with the bent Laue crystal and multilayer described in section 3.1.4. By focusing the beam all incoming photons are used to illuminate the sample, making the size of the detectable diffraction domains smaller.

The ideal intensity beam profile would be a box profile, with a constant intensity across the beam and no intensity outside it, i.e. a beam with no tails. Unfortunately this is not the product of the method used for micro-focusing, and the resulting beam profile is different in the horizontal and vertical planes due to the different focusing optic elements used. By inspection it is found that both profiles can be approximated by pseudo-Voight functions with clearly different α parameters, where α is a scaling factor of the combination of a Gaussian and a Lorentzian function in the pseudo-Voight function.

3.3.3 Verification

The fact that the beam profile is non-uniform implies that the procedure for validating if subgrains are fully illuminated changed a great deal.

The shape of the beam profile means that some diffraction spots appearing on the detector will originate from subgrains positioned in the tails of the beam. Such a diffraction spot will be less intense than a diffraction spot belonging to a subgrain of the same size laying in the centre of the beam. However, the intensity difference could also arise from a size difference of the diffracting subgrains. The solution to this ambiguity is to translate the sample horizontally and vertically with respect to the beam within a two dimensional measurement grid.

One subgrain illuminated in different positions in the beam according to the grid, will give raise to diffraction spots in the same position on the detector. The intensity will differ at different positions in the grid. An integrated intensity is found by fitting the beam intensity profile to the measured intensities in the grid. The result of the fit is the integrated intensity of the subgrain, which may be converted to a volume, and the two dimensional centre-of-mass position of the subgrain.

Rejection of diffraction spots because of tails in the neighbouring ω-bins depend on the size of the ω-bins. In the case where the bins are large compared to the mosaic spread of subgrains it makes sense to reject the diffraction spot. If not, a summation of the intensities must be made.

The introduction of a measurement grid implies that the time resolution is much worse than in the case of recrystallisation. In practice the introduction of a measurement grid means that only a few ω-bins can be measured. In the experiment discussed in Chapter 5 a 4×4 grid in (x, z) was used with 30 ω bins. This was associated with a time resolution of 15 minutes. Because of the few ω bins only limited information on the orientation of the subgrains was obtained.

3.4 Related experiments

During the course of this Ph.D. project some time have been spent on experiments closely related to recovery. Two of these experiments will be discussed in this section. The first experiment aimed at *in-situ* studying nuclei of recrystallisation with orientations not present in the deformed grains. The aim of the second experiment was to study the grain morphology of the individual grains during growth in the deformed microstructure due to recrystallisation.

3.4.1 Nucleation

The work described in this section are mostly performed by A. W. Larsen and is part of his Ph.D. thesis (Larsen, 2004) and published in (Larsen, Poulsen, Margulies, Gundlach, Xing, Huang and Juul Jensen, 2005) and (Larsen, Gundlach, Poulsen, Margulies, Xing and Juul Jensen, 2004). In this section a brief description of the experiment, results and findings are presented.

3.4.1.1 Introduction

Nucleation of recrystallisation is one of many nucleation processes vigorously debated in the literature. One reason for the debate is the experimental techniques used. The combination of *in-situ* measurements and detection of a single bulk grain is not a possibility with standard techniques.

The aim of the experiment described in this section was to expand the use of the 3DXRD microscope to enable detection of nuclei during annealing and determination of the orientation of the nuclei.

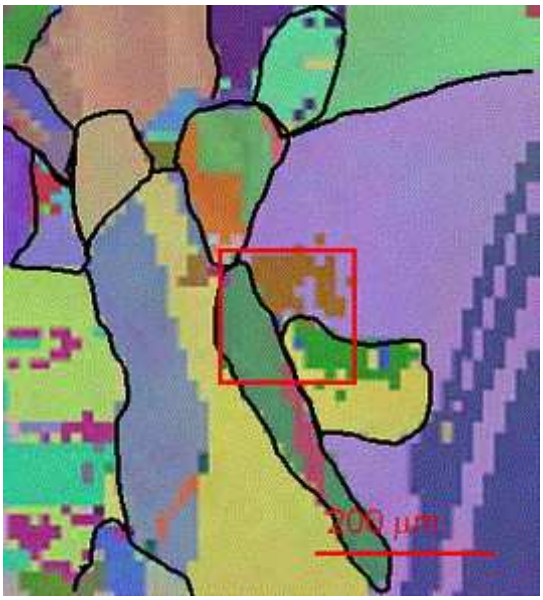

Figure 3.6: *An EBSD map of sample B. Grain boundaries are marked in black and the red box indicates the area surrounding a triple junction, this is the area subjected to X-ray diffraction examination. Reproduced from* (Larsen *et al.*, 2005).

3.4.1.2 Material

The material used in this study was a 99.995% pure copper cold rolled to 20% reduction in thickness, and annealed afterwards for 8 hours at 700°C, which gave a microstructure with coarse grains with an average size of 500 μm. Finally the material was cold rolled to 20% reduction in thickness. From TEM studies the distance separating dislocation walls, which exhibited a misorientation larger than 1°, was found to be 1 to 2 μm.

Three samples (A, B, C) used for the 3DXRD experiment were cut into 10 by 10 mm^2 plates, which was thinned to a thickness of 300 μm. Finally the sample was electrochemically polished to remove possible unwanted surface nucleation sites. An EBSD orientation map of sample B is shown in figure 3.6.

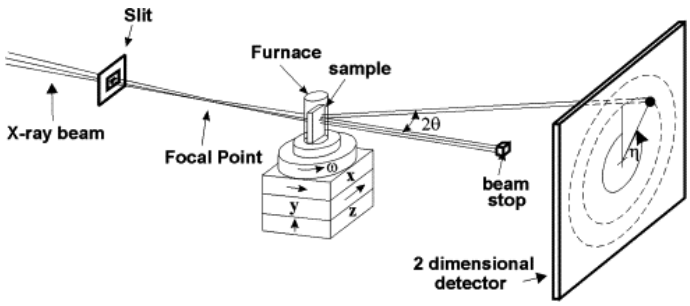

Figure 3.7: *Schematic diagram of the setup. The angles ω, θ and η are shown. In contrast to the setup used for recovery studies where the focal point is on the sample, in this case the focal point here is in front of the sample. Reproduced from* (Larsen *et al.*, 2005).

3.4.1.3 Experimental setup

The experiment was performed using the 3DXRD microscope in orientation configuration (see section 3.1) with a 14-bit FRELON detector (described in section 3.1.6). The X-ray beam was monochromated (51 keV) and focused in both the horizontal and vertical directions using the bent Laue crystal and the graded multilayer (see section 3.1.4) to a nearly homogenous beam of 49×49 μm.

This setup follows the line of setups for experiments used to study growth curve behaviour in recrystallisation (see section 3.2) and the experimental setup for recovery studies (see section 3.3). A schematic diagram of the setup can be seen in figure 3.7.

The idea was to characterise some areas of the samples with respect to the crystal orientation, before, during and after annealing. To increase the volume characterised, exposures were made at a set of sample positions. These sample positions were in a 2×2 (y, z)-grid, in which the grid points were 40 μm apart. At each position a sweep scan over 42° in ω (see section 3.1.7.2) was made with $\Delta\omega = 1°$ which corresponds to measurements of partial pole figures covering a fan of 42° allowing the crystallographic orientation to be determined. The acquisition time was 1 second per image and about 10 minutes per measurement grid. The samples were mounted in the furnace, and annealed at 290° for 1 to 3 hours.

3.4.1.4 Data analysis

All acquired X-ray diffraction images were subjected to a background correction. The applied background subtraction algorithm was not the background subtraction described in section 4.1.1, but one where the corrections are made only from information given in the image. The algorithm[2] is based on a box sliding across the image. The box is of a given pixel size (square box 5 to 10 pixels wide). Inside the box the average and standard deviation of the pixel intensities are calculated. All pixels with a 'low' standard deviation are defined as background pixels. The overall background of the images is determined by interpolation of the average pixel intensity values of the background pixels.

For each nucleus found the orientation was determined by the multigrain indexing algorithm, GRAINDEX (described in section 3.1.9). Before images could be used for GRAINDEX analysis the X-ray diffraction images had to be spatially corrected, this spatial correction was done by the program FIT2D. Examples of background subtracted and spatially corrected X-ray diffraction images is presented in figure 3.8. The volume of the nucleus was determined from the intensity of the diffraction spot and from the intensity of a reference sample of known thickness (see section 3.2.3). Finally the position of the nucleus within the sample (x, y, z positions) was determined by trigonometry, based on the information when a nucleus rotated out of the X-ray beam during the ω-scan.

3.4.1.5 Results

When studying the intensity level of the background the smallest detectable volume was determined using the method for calculating the volume from intensity. The smallest detectable volume was found to be 0.70 μm in diameter.

Three nuclei were detected: One in sample A, two in sample B and none in sample C. All three nuclei were determined to be positioned at least 65 μm from the surfaces. This confirms the hypothesis that internal triple junctions are potential nucleation sites in the material. Such a finding was also reported from surface studies (Sabin, Winther and Juul Jensen, 2003) and from serial sectioning results (Vandermeer, 1959).

[2] Algorithm for background subtraction in 3DXRD images developed by J. Tauber and E. M. Lauridsen and J. R. Bowen

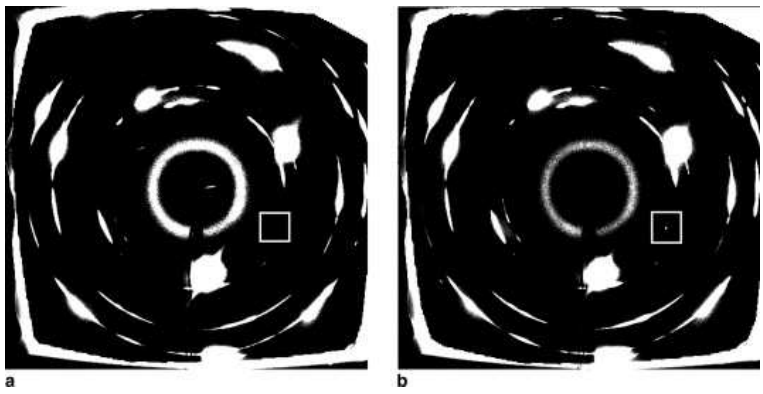

Figure 3.8: *Examples of X-ray diffraction images, which have been subjected to both background subtraction and spatial correction. (a) the as-deformed sample (b) the sample having been annealed at 290°C for 3 hours. Reproduced from* (Larsen *et al.*, 2005).

Two of the three nuclei were found to have orientations associated with the orientations of the deformed parent grains. The last nuclei did not have any association to the deformed parent grains nor was it related to their first order twins. Nor was the orientation found in the range of orientations from the as-deformed sample.

3.4.1.6 Conclusions

The 3DXRD microscope experimental package has been expanded with a unique method for *in-situ* studies of nucleation of recrystallisation. This method is closely related to the methods developed to *in-situ* studies of growth curves in recrystallisation (see section 3.2) and the *in-situ* study of recovery (see section 3.3). Using the method developed three nuclei have been identified and followed during annealing at 290°C. The analysis of orientation relationships between the nuclei and the deformed parent grains, revealed that a nuclei may develop within the parent orientation, the twin orientation or a completely new orientation.

3.4.2 Recrystallisation

The work described in this section was mostly performed by S. Schmidt and published in part in (Schmidt, Nielsen, Gundlach, Margulies, Huang and Juul Jensen, 2004).

3.4.2.1 Introduction

The motivation for this experiment was to measure *in-situ* grain shape and the growth velocity of recrystallising grains migrating through the deformed matrix of a deformed metal without interferences from other grains. Such measurements could lead to a better understanding of the mechanisms occurring during recrystallisation.

3.4.2.2 Sample preparation

The material chosen for this study was an aluminium alloy (AA1050). The initial material was a single crystal with orientation {110}[001], which was cold rolled to 42% reduction in thickness yielding a final thickness of 1 mm. Samples for the 3DXRD experiment were cut out into 6×5 mm^2 sizes (Transverse Direction (TD), Rolling Direction (RD) directions respectively). A TEM image of the cold rolled material can be seen in figure 3.9.

To produce controlled nucleation sites hardness indentations were made in the TD-Normal Direction (ND) surface. The idea behind the indentation was that when the sample was annealed a nuclei would form from at least one of these indentation sites and grow during recrystallisation. This geometry resembles that used in the classical work by Beck (1954).

3.4.2.3 Experimental setup

The experiment was performed using the 3DXRD microscope in tracking configuration (see section 3.1) with a high resolution detector (described in section 3.1.6) placed a few millimetres from the sample. The X-ray beam was monochromated (52 KeV) and focused in the vertical direction, to 6 μm using the bent Laue crystal. In the horizontal direction the beam size was 600 μm defined by slits.

The concept of the experiment was to preanneal the sample for one hour to nucleate a grain. A diffraction spot from such a grain was located at

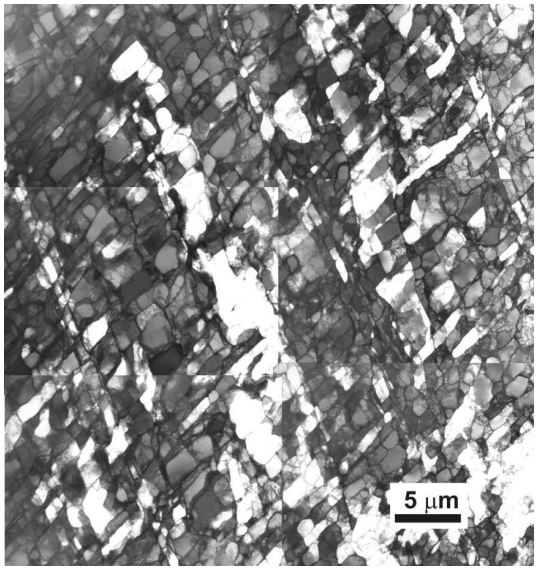

Figure 3.9: *A TEM micrograph of the cold rolled material used for the recrystallisation study. The structure is subdivided by elongated, almost planar dislocation boundaries inclined at 30° to 35° to the rolling direction. Reproduced from* (Schmidt *et al.*, 2004).

$\omega = -9°$, $2\theta = 14.7°$ and $\eta = 220°$. A number of diffraction images were acquired while the sample was translated stepwise in the z-direction, each image provided information on the grain shape in one section (one layer) as sketched on figure 3.10. In this way the complete 3D shape of the grain was determined. The basis of this idea and the setup can be seen in figure 3.10. To ensure that the grain did not grow out of the number of layers probed, a few extra diffraction images were recorded as a buffer, after the grain was translated out of the X-ray beam. If the grain was found in one or more of the buffer images, more layers were used in the next 3D picture.

After the initial measurement the sample was annealed for 30 hours at temperatures between 280°C and 290°C. During the time of annealing 73 3D pictures of the grain shape were obtained. After 30 hours the temperature was raised to 310°C and the last picture was gathered.

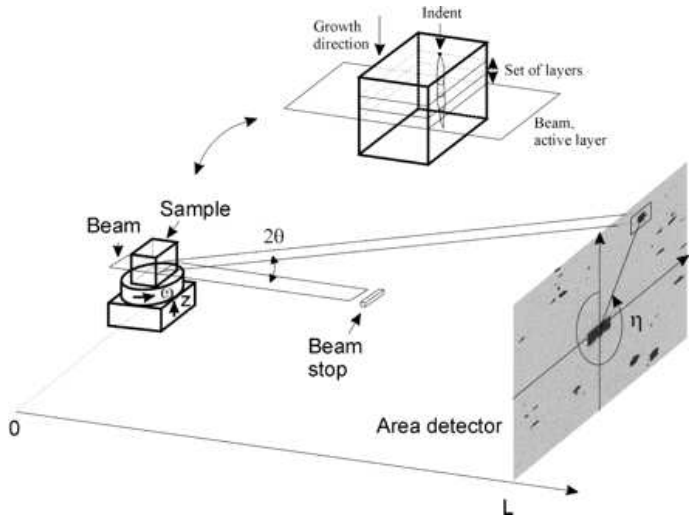

Figure 3.10: *Sketch of the setup for the experiment. The coordinate system (x,y,z) is defined in the standard way of the 3DXRD microscope. Inserted is a sketch of the sample and the X-ray beam. Translating the sample in the z direction yielded a set of layers used to produce a picture of the grain. Reproduced from* (Schmidt *et al.*, 2004).

3.4.2.4 Data analysis

All recorded X-ray diffraction images were deconvoluted by the point spread function of the detector. Afterwards all images were subjected to background subtraction and normalised to the synchrotron current. The resulting shape of the diffraction spot is a projection of a cross section of the grain seen from that exact angle (ω). A number of pictures of the grain can be seen in figure 3.11.

3.4.2.5 Results

Looking at all the 3D pictures the grain was found to be very irregular in shape and the growth also occurred irregularly. Similarly the growth was very abrupt; some times the growth was in one direction, at other times the growth was in other directions. Interestingly, the growth behaviour mentioned is in sharp contrast to theories of steady state boundary migration, which predict growth behaviour similar to that of soap bobbles.

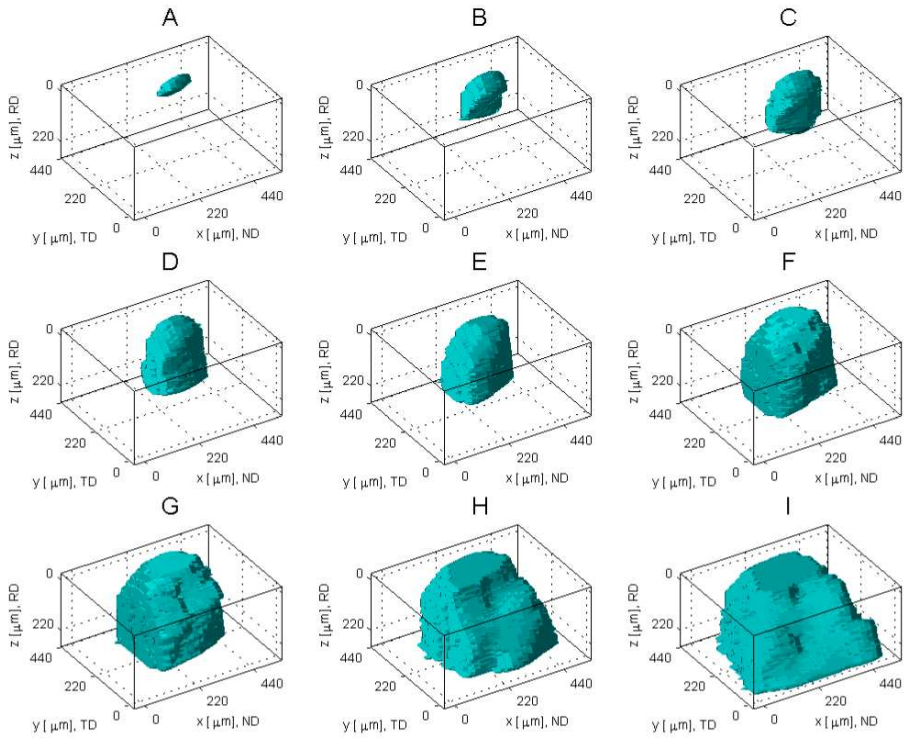

Figure 3.11: *A storyboard of the measured grain growth during recrystallisation. The surface of the sample was roughly at $z = 0$. The grain, initially a small object, expanded mainly along the x and y axes during the first time intervals. It is observed that different parts of the grain are expanding at different rates at different times. Reproduced from* (Schmidt *et al.*, 2004).

Electron microscopy *in-situ* studies have reported similar results (see references in Schmidt *et al.* (2004)). However in electron microscopy investigations surface effects cannot be ruled out. This objection is not valid in this experiment because the observed grain is identified as a bulk grain.

3.4.2.6 Conclusions

A new use of the 3DXRD microscope has been demonstrated. This method enables a direct measure of the 3D shape and growth of recrystallising grains. The method can be used to study the fundamental mechanisms of grain boundary migration during recrystallisation. Expanding the method to more angle projections will provide pictures with a higher spatial resolution. Simultaneously a broader ω-scan (e.g. -45° to 45°) will provide the orientation of the grain.

Chapter 4

Data Analysis Algorithms

This thesis follows the tradition of the 4D centre at Risø for developing software to analyse 3DXRD data (e.g. Lauridsen (2001)). The reason why this tradition exists is that there exists no program or software suite that does the analysis which is wanted.

The present chapter is divided into three sections, considering three complementary methods of analysing the data acquired. In all cases, the basis of the analysis is the acquisition of diffraction spots from a specific individual subgrain at a given time.

The first method is based on a size distribution (discussed in section 4.1.) In this method no information on the dynamics of individual subgrains is stored. Instead the method provides statistical information on the time evolution of an ensemble of subgrains.

The two other methods (discussed in section 4.2 and section 4.3) both produce growth curves for individual subgrains. The reasons for two approaches to the same kind of analysis are manyfold. **Firstly**, due to a new scanning method implemented at the 3DXRD microscope —the sweep-scan (see section 3.1.7.2)— the number of diffraction images has increased enormously. This increased amount of data could hardly be handled by the first approach. In the second approach the amount of data was reduced by only using the image pixels in the Debye-Scherrer rings. **Secondly**, the first approach was based on two different programs, one being an image analysis program (ImagePro) and the other being a programming language designed as a mathematical language for data applications (MatLab). The second approach eliminates the dependence of two programs. **Thirdly**, a wish to oper-

ate in a higher dimensional space to ensure the best possible interpretation of the diffraction intensities recorded. This method was published (Gundlach, Schmidt, Margulies, Knudsen, Pantleon and Poulsen, 2005). All three algorithms are designed to run on the same type of 3DXRD data described in section 3.3. The data acquisition for a (h×i) measurement grid with j ω bins of size k, can be summarised in nested loops:

```
while time from start to end of experiment
    for sample position y = 1 to h
        for sample position z = 1 to i
            for sample omega position w = 1 to j
                {acquire diffraction image while rotating the
                 sample from -k/2 to +k/2}
            end
        end
    end
end
```

The run times of the algorithms discussed in the following sections are commented but no worst case analysis of the algorithms are presented.

4.1 Histogram analysis

In this analysis method all diffraction images are seen as single "snap shots" of the current state of the material. This means that all images in one time frame are considered and no validations are made to ensure that the full volume of a given subgrain is in the X-ray beam. This histogram analysis is not the main analysis tool used for the experimental 3DXRD method developed for *in-situ* studies of recovery (described in section 3.3). But since no additional data acquisition is necessary to perform this histogram analysis, the histogram analysis is considered to provide "free" extra information. The same diffraction images used for the growth curve analysis in sections 4.2 and 4.3 that can be used in the histogram analysis.

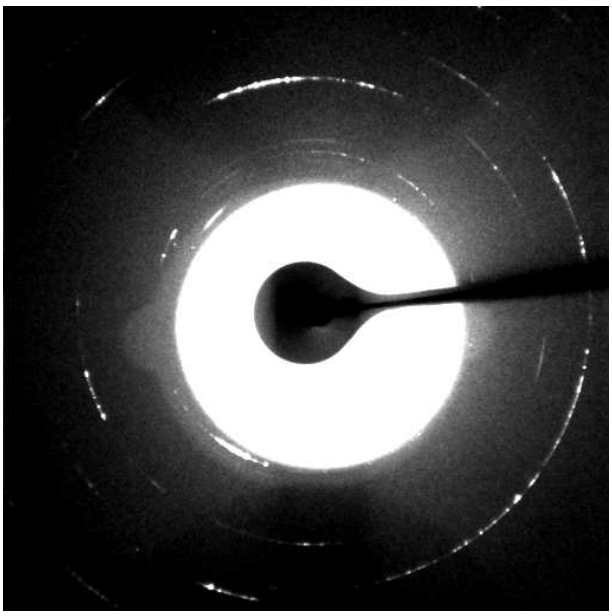

Figure 4.1: *A diffraction image of Aluminium cold rolled to 38% reduction. This X-ray diffraction image was recorded by a Frelon detector. No background subtraction has been made on the image. Similar effects as the ones in figure 3.4 and explained in section 3.1.8 can be seen in the image.*

4.1.1 Background subtraction

The images acquired on the Frelon CCD are subjected to a special background due to scattering from the various elements between the X-ray optics and the detector, and also from artifacts like hot spots on the detector and from an inhomogeneous flat field. An example of a typical diffraction image can be seen in figure 4.1. Evidently, the background signal can be as intense as the diffraction patterns and a correction of the images is consequently required.

The standard method of background subtraction is the following: two images are recorded, one image without the sample present, the background image, and another image without any X-ray illumination a so called darkfield image. The latter image records the internal electronic noise in the detector which is dependent on the acquisition time of the image. The darkfield image is subtracted from both the data image and the background

image. The subtracted images are scaled to the synchrotron current and finally the background image is subtracted from the data image. This gives an image of only the diffracted X-rays.

The standard method does not apply to the present case. The furnace glass gives raise to "amorphous scattering", which is absorbed in parts of the image by two rather large metal plates in the sample holder. This background signal is very sensitive to the angular position (ω position) of the sample. In addition, the background depends critically on the mounting of the sample. Applying the standard method would therefore at best be tedious. Consequently another method for background subtraction was applied.

The method applied is a median method. All images in one acquisition sweep (see section 3.1.7) are stacked together for each image pixel. The median of the intensity distribution for this pixel is found and placed in a new background image. This background image is subtracted from all images in the acquisition sweep. No scaling to the synchrotron current is made because, the acquisition time of a sweep is so short that the synchrotron current is almost constant during the acquisition. An example of a background-corrected diffraction image can be seen in figure 4.2. The same background subtraction method is applied to all three analysis methods discussed in this chapter.

4.1.2 Spot finding

After the background correction, all images are grouped into time frames; one time frame being one run of the measurement grid introduced in section 3.3.3. One by one the images are processed in ImagePro, a commercial image processing program. This program has a powerful spot-finding/labelling algorithm for two dimensional images used here to identify the distinct (non-overlapping) diffraction spots. Spots are found based on the following three criteria:

1. **an intensity threshold criterium.** Neighbouring pixels all with intensities above the threshold are considered to be a spot;
2. **an aspect ratio criterium.** Isolated diffraction spots will appear as nearly circular. By setting a threshold of 2 on the aspect ratio, spots composed of several overlapping sub-spots are rejected from the analysis;

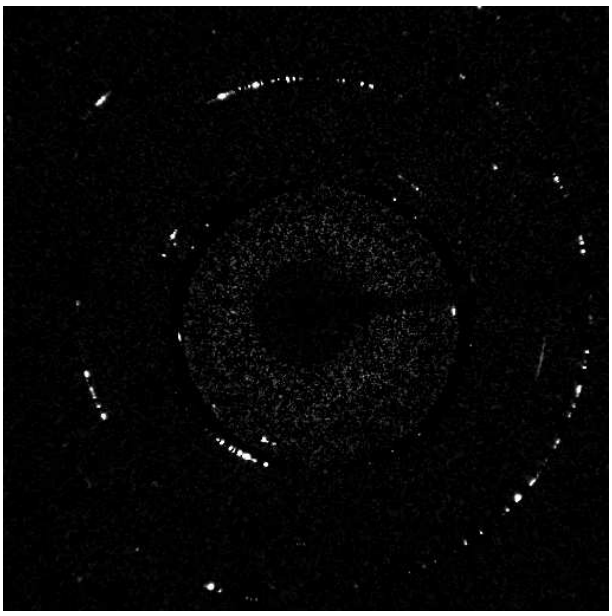

Figure 4.2: *A diffraction image of Aluminium cold rolled to 38% reduction subjected to the median background subtraction method. The diffraction image before the background subtraction is displayed in figure 4.1.*

3. **a position criterium.** If the Bragg angle (2θ) of the spot is not within 1% of the predicted value for any of the relevant Debye-Scherrer rings the spot is rejected. Such spots are typically caused by cosmic rays or hot spots on the CCD, or they can arise from second phase particles in the sample.

For each spot the centre of mass, the integrated intensity (measured as the sum of intensities of the pixels belonging to the spot) and the aspect ratio are recorded along with the image number to a text file to be used in subsequent parts of the analysis.

4.1.3 Histograms of apparent subgrain size

The core program parts of the histogram analysis are programmed in MatLab. The third criteria described above turned out to be easier to implement in MatLab. All the text files are read and from the centre of mass position,

spots are associated with a Debye-Scherrer ring. If no Debye-Scherrer ring can be associated with a given spot, that spot is rejected as described in section 4.1.2. Spots with overlapping pixel coordinates and appearing in images related to adjacent ω-positions are treated as one spot. Their integrated intensities are summed. The result is a list of diffraction spots. The integrated intensity of these spots can be used to calculate the associated subgrain volumes according to section 3.2.3, and the list of diffraction spots may finally be grouped according to associated subgrain size. However, the subgrain sizes calculated from the integrated intensities of diffraction spots, are apparent subgrain sizes, since it has not been validated whether a subgrain is fully located within the X-ray beam or if the diffraction spot is related to a subgrain positioned in the tail of the X-ray beam. Subgrains located in the tail of the X-ray beam are not illuminated with the same number of photons as subgrains fully located within the X-ray beam and thereby appear to be of smaller size. This gives a bias towards smaller subgrain sizes.

By comparison the classical techniques used to measure subgrain sizes, such as electron microscopy, do not measure the true three dimensional sizes either. In EBSD measurements, a two dimensional area is measured and the size of this is dependent on the section probed within the subgrain. However, the method of apparent subgrains sizes can be and has been used to compare relative changes between measurements. Also stereological tools exist for estimating the true size distribution from the apparent size.

The second part of the program performs a "brute force" least-squares fit of a logarithmal normal distribution simulated for the known size of the X-ray beam to the frequencies found in the acquired data. The fitting parameters are the width and the centre of the distribution. By "brute force" is meant that given a range for the centre and a range of widths, the algorithm calculates subgrain size distributions for each combination of width and centre. The one combination with the lowest χ^2 is returned from the fitting. An example of one output is shown in figure 4.3.

4.2 Growth curves - first approach

This section discusses the approach taken in the software development which resulted from the analysis of the first experiment performed in year 2002 (Gundlach, Pantleon, Lauridsen, Margulies, Doherty and Poulsen, 2004a). In this approach two different software programs are used: Initially the background-corrected diffraction images are processed in ImagePro, and

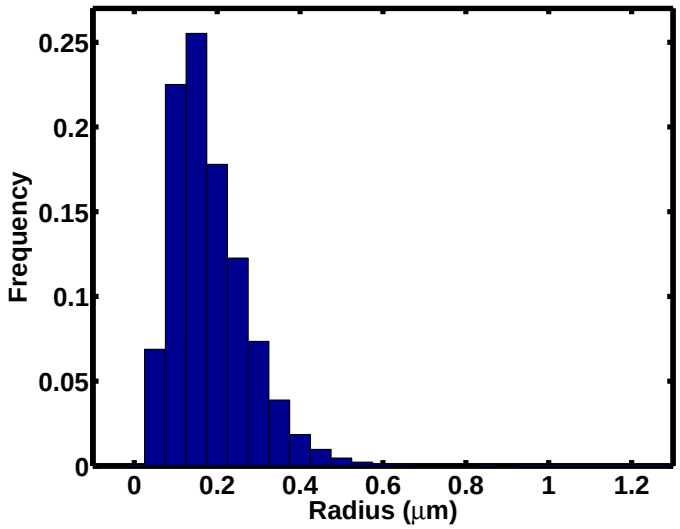

Figure 4.3: *Histogram of true subgrain sizes found by the least-squares fit to the measured apparent subgrain sizes. The figure is from a sample of aluminium (AA1200) cold rolled to a true strain of 2 measured at room temperature.*

subsequently the output is processed by a MatLab program which produces the growth curves for the individual validated subgrains. The method is based on an area-by-area concept in the sense that a small area around a diffraction spot is analysed individually at each time step and at each ω position.

4.2.1 Spot finding

The aim of this image processing procedure is to identify non-overlapping diffraction spots in individual images and determine their integrated intensity. The integrated intensity is found by summing the pixel intensities within a small square area around the diffraction spot, this area is referred to as the Area Of Interest (AOI). The criterion used to identify these diffraction spots are the intensity threshold criterion, the aspect ratio criterium and the diffraction spot position criterion as described in section 4.1.2. The selection and validation of diffraction spots according to the above criteria is performed manually.

Since each measurement grid is recorded in the same sequence at each time step, image numbers can be sorted by the position in the measurement grid and the ω position. The integrated intensity is calculated for the AOI using the "histogram function" in ImagePro. The AOI is selected to be as narrow as possible around a diffraction spot and centred at the diffraction spot. A small portion of the integrated intensity originates from the background surrounding the diffraction spot but still from within the AOI. However, since a background subtraction has been performed on the images (see section 4.1.1) the integrated intensity from the background is negligible.

The output of the ImagePro procedure is a table of integrated intensities according to positions in the measurement grid at each time step in the experiment. The centre of mass pixel position is determined from which the η position (see figure 3.2) is calculated and recorded in the table. Such a table is produced for each ω position for each AOI.

To ensure that the selected AOI is valid during all time steps a mosaic image containing the AOI at all times, is created for a given AOI at each position in the measurement grid and each ω position. Based on these mosaic images, validation is performed manually rejecting AOIs where either multiple diffraction spots appear or the diffraction spot is not fully in the AOI. An example of such a mosaic image is displayed in figure 5.6.

4.2.2 Growth curves

The final step in the data analysis method is the calculation of growth curves for individual subgrains. These growth curves are based on the evolution of the integrated intensity of the AOIs. This final step in the analysis method is implemented as a program in MatLab. The overview of this program is as follows:

- For each ω position
  - Find the right sequence of files
  - Make a matrix of integrated intensities from the measurement grid
  - For each time step in the experiment
    - Perform a fit of the known X-ray beam profile to the intensity matrix
    - Calculate the corresponding diffracting volume

4.2.2.1 Right sequence of files

This is a small task that ensures that the right output files from the Image-Pro program are read into MatLab in the right sequence corresponding to the right position in ω and position in the measurement grid.

4.2.2.2 Intensity matrix construction

For each ω position one output file is produced from each position in the measurement grid. Each file has the calculated values (integrated intensity, η position) at each time step during the experiment. The values are subsequently transformed into an integrated intensity matrix for each time step where the indices of the intensity matrix are equivalent to the positions in the measurement grid. In MatLab this can be constructed as a three dimensional matrix M_{ijk} where i, j represents the measurement grid position and k represents the time step.

4.2.2.3 Fit of intensities to the known X-ray beam profile

The critical part of this growth curve analysis program is the fitting of the intensity matrix to the known X-ray beam profile. This is done by using a built-in least-squares curve-fitting function. The X-ray beam profile was assumed to be of a two dimensional Gaussian form with a measured Full-Width-at-Half-Maximum (FWHM) contaning no background. The fitting procedure simultaneously finds the position of the centre of the subgrain with respect to the measurement grid and the fully integrated intensity of the diffraction peak.

4.2.2.4 Volume calculation

The final part of the MatLab program is the determination of the subgrain volumes. The fully integrated intensity calculated in the least square curve fit is used to calculated a subgrain volume using the method described in section 3.2.3.

Some subgrains are rejected on the basis of the fitted positions. If the centre position of the subgrain is outside the measurement grid the fit is considered unreliable, due to the fact that all the data points used in the

fitting procedure are located only on one side of the curve of the beam profile. This validation is done manually.

4.2.3 Evaluation

The final product of the program is the growth curves of the AOIs of the diffraction images. Only a small portion of all AOIs results in growth curves, these AOIs satisfy the following: 1) The AOIs contains only one diffraction spot that stays within the AOI during all time steps of the experiment. 2) The position calculated for each of the diffracting subgrains are found to be in the centre of the measurement grid. 3) The mosaic spread of the diffraction is contained within one ω bin.

Overall this is a "hands-on" analysis method, where it is possible to follow all steps of the construction of the growth curves. All validations are made manually, which makes it ideal for proving the experimental method developed to study the growth of small diffraction domains. However the analysis is slow, partly because it is based on two separate programs that are not linked, making it troublesome to use for large data sets and partly because of all the manual inspections.

Another problem originates from the fact that two different subgrains located apart in the measurement grid, may result in overlapping diffraction spots with an aspect ratio close to 1, which means that these are seen as one diffraction spot. The least-square fitting will not converge, and the diffraction spots will be rejected since there is no means to separate these diffraction spots. In this process more subgrains are lost.

4.3 Growth curves - 5D approach[1]

An improvement of the approach presented in section 4.2 would be to automate the image processing part (finding isolated diffraction spots and defining AOIs containing single diffraction spots). Another analysis method was developed for a number of other reasons such as:

[1]This section is based on the article "Image analysis for X-ray studies of the dynamics of individual embedded subgrains during recovery" from the authors C. Gundlach, S. Schmidt, L. Margulies, T. Knudsen, W. Pantleon and H. F. Poulsen.

One program. Implement a program that as input takes either the raw data images or background corrected data images and performs both the task of identifying non-overlapping diffraction spots and the task of the production of a large number of growth curves;

Increase the number of diffraction spots. A method to increase the number of diffraction spots may be realised either by splitting overlapping diffraction spots or by incorporating into the analysis method the ability to identify diffraction spots appearing later in the time series.

Decrease bias. The first approach could be seen as biased because of all the manual validations and because only very isolated single diffraction spots could be used, (hence biased towards certain orientations.) Furthermore as the diffraction spots were identified in the first timestep, the selection was biased towards certain subgrains, excluding e.g. those that grew larger than the detection threshold during the annealing.

The new idea behind the new approach is to look at the entire data set, in a higher dimensional space. Where a diffraction spot could spread out in different directions, this spread could be in orientation (mosaic spread), spatial (subgrain illuminated at different positions of the measurement grid) and over time (the diffraction spots exist in more time steps during the measurement). In this higher dimensional space diffraction spots can be tracked and the integrated intensities can be found and calibrated to volumes to provide the growth curves. It will be shown that this method can separate diffraction spots belonging to the same ω and η values but at different positions in the measurement grid.

The analysis software program implemented consists of a few small routines each of which will be described in the following.

4.3.1 Caking

The first consideration in working with a higher dimensional space and attempting to handle all the data simultaneously is to exclude those parts of the images which contains no relevant information. As a result the space between Debye-Scherrer rings are excluded.

The centre position of a diffraction spot in a given image can be described by its pixel coordinates, but it can also be described by the azimuthal position, η, on a given Debye-Scherrer ring with a radius given by the Bragg angle, 2θ.

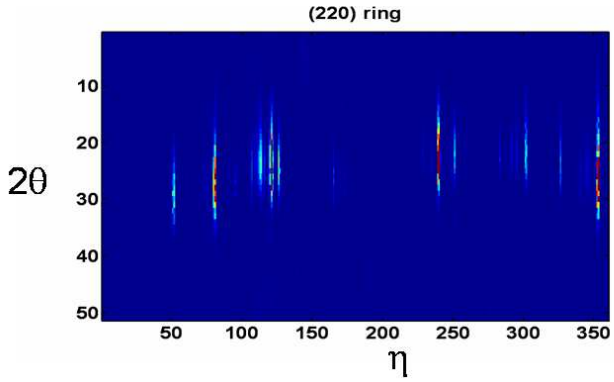

Figure 4.4: *The result of a polar transformation of one Debye-Scherrer ring is a* $(2\theta, \eta)$ *plot.*

The first step in the analysis is the caking of Debye-Scherrer rings. Caking is a polar transformation from pixel coordinates to coordinates of 2θ and η. The Debye-Scherrer ring is defined by a range in 2θ. An example of a caked Debye-Scherrer ring is plotted in figure 4.4.

Integrating pixel intensities over 2θ in the polar coordinate space gives an intensity plot over η values. In this program the caking is done by a MatLab program[2] An example of this intensity plot can be seen on figure 4.5.

4.3.2 The 5 dimensions

The five dimensions that are giving raise to the 5 dimensional diffraction space are described in the following.

Sample positions y and z The measurement grid is made by translating the sample perpendicular to the X-ray beam. Given the laboratory coordinate system these translations are in the y and z directions, hence the name sample positions y and z. This is a two dimensional space.

Angular coordinates At each position in the sample's y and z coordinates an (ω, η) plot can be inserted, where ω is the sample rotation angle

[2]The MatLab program was implemented by V. Honkimäki a beamline scientist at ID15, ESRF.

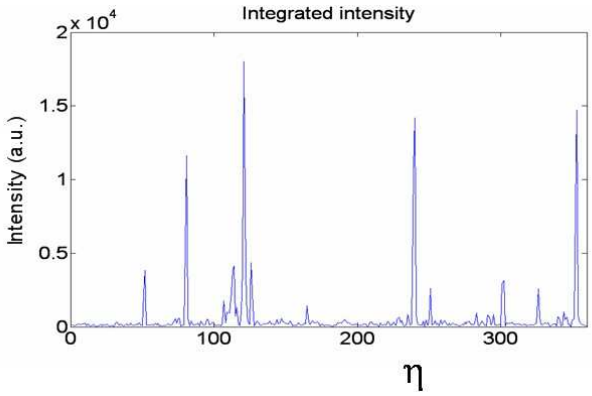

Figure 4.5: *Intensity plot of the caked image in figure 4.4. A peak in the plot show the position of a diffraction spot in η. The integrated intensity of a peak is the intensity of the corresponding diffraction spot.*

and η is the angle on the Debye-Scherrer ring (defined in figure 3.2). The (ω, η) plot is coming from the caking performed at different ω positions. An example of a (ω, η) plot is depicted in figure 4.6.

Time The fifth dimension is the time during the experiment.

4.3.3 Connected components and labelling

The problem of producing growth curves for individual subgrains is now reformulated as the problem of finding blobs in the 5D space. Blob finding in a 5D space is considered an extension to the general case of spot finding in a 2D space, a well-known problem. The solution to the spot finding problem in 2D space is algorithms named "Connected Components" and "Labelling" algorithms (Bässmann and Besslich, 1991). These algorithms are two pass algorithms where the connected components are located in the first pass and the unique labelling of the components are achieved in the second pass.

Initially the connected component and labelling algorithm is summarised as presented e.g. Bässmann and Besslich (1991). The space is expanded with two rows of zero values at the front and end of each dimension, these rows are used later in component testing. A threshold is used to mark when a pixel is above the noise level and should be counted as a spot.

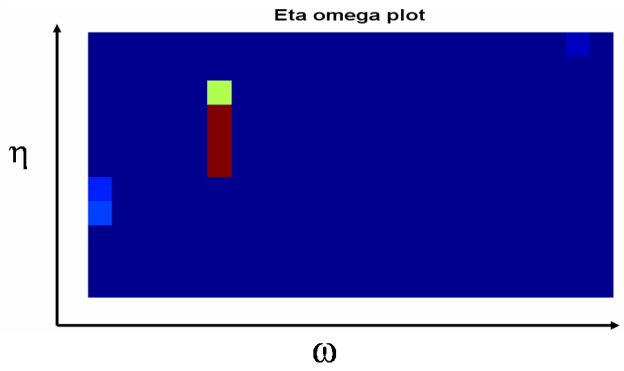

Figure 4.6: *An example of a* (ω, η) *plot. Different intensities above a threshold are marked with different colours. The threshold value is marked with dark blue.*

In two dimensions the algorithm starts at the index (0,0). When pixel (i,j) has a higher intensity than the threshold the corresponding pixel (i,j) in a second marked image is labelled. Before labelling the pixel, the neighbouring pixels according to connectivity in the marked image are tested. If a neighbouring pixel has already been labelled the pixel (i,j) receives that label. A potential problem is if more neighbouring pixels have different labels. A priority list of neighbours decides which label the pixel (i,j) will receive and an equivalent list for labels are maintained. The algorithm continues to the next pixel until all pixels have been tested. In the second pass the blobs are labelled according to the equivalents list.

Turning to the 5D space used in the 3DXRD method, the second pass is also used to calculate the integrated intensities of the components found. Each blob is assigned a table with entries for each of the desired properties. When a pixel is assigned to a specific blob the table of that blob is updated. Of special interest is the intensities of a given blob for each position in the measurement grid and to each time step. Another property in the table associated to a blob is the centre of mass in the ω and η dimensions at each time step.

4.3.3.1 Connectivity

The connectivity is one of the main concepts of this algorithm. The connectivity rule determines whether pixels above the intensity threshold are

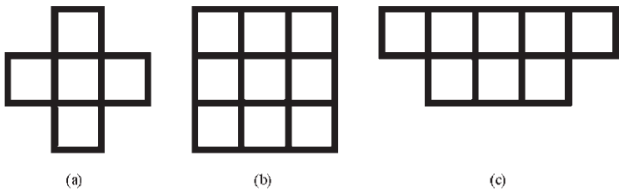

Figure 4.7: *Connectivity rules used in the Connected Component and Labelling algorithm. (a) is a nearest 4-neighbour connectivity used as default for all 2D subspaces. (b) is a nearest 8-neighbour connectivity used in the* (ω, η) *2D subspace. (c) is a special connectivity rule used in the* (ω*,time) 2D subspace, the reason for this connectivity is a minor sample rotation (in* ω*) due to heating.*

assigned to an existing blob or to a new blob. The connectivity rules applied are tailor-made to the 3DXRD experiment. The easiest way to look at the connectivity is to look at different two dimensional subspaces in the 5D space (see figure 4.7).

As a default all two dimensional subspaces are 4-connected. The meaning of this may be visualised by looking at a two dimensional plan. Looking at a pixel (i,j) with an intensity above the threshold 4-connected means investigating whether any of the neighbouring pixels (i,j-1), (i,j+1), (i-1,j) and (i+1,j) also have an intensity above the threshold.

The (ω,η) subspace is 8-connected, meaning that the pixels (i-1,j-1), (i-1,j+1), (i+1,j-1) and (i+1,j+1) also are considered. This choice of 8-connectivity is due to the fact that the mosaic spread of a given spot may be anisotropic with an arbitrary direction.

The data from the experiment described in section 5.2, turned out to be a little more complicated to analyse than expected. During the analysis of the data it was realised that the sample probably had rotated slightly in the ω direction during heating. Because of this rotation the connectivity in the (ω,time) 2D subspace is special. The solution was to assign a specific pixel to an existing blob only if it is one time step and within two ω steps away from a pixel in the blob.

An example of the results of the "Connected Component" and "Labelling" routine is depicted on figure 4.8. The figure is a snapshot in time (at a given value of time) and the 4D space is shown as a mosaic image

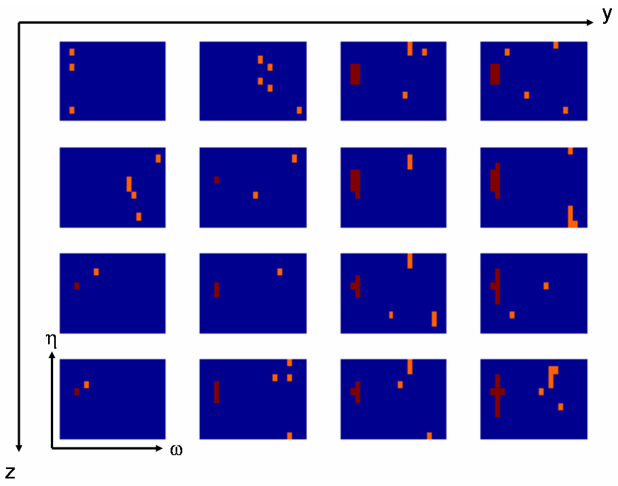

Figure 4.8: *A 4D mosaic image showing a blob found using the Connected Component and Labelling routine. Only a small portion of the 4D space surrounding the blob is shown. The red pixels belong to the blob. The rest of the coloured pixels have an intensity value above the threshold, but are not connected to the blob.*

composed of 16 (ω, η) images at the 4×4 sample positions.

4.3.4 Multiple peak splitting

The last part of the program performs a least squares curve fit of the known X-ray beam profile to the intensities obtained at each time step. A multi component least squares curve fit is used. The number of components used in a single fit is based on the number of local maxima in the intensity matrix. The use of a multi component least squares curve fit enables splitting of multiple peaks lying close in (ω, η) space but separated spatially. An example of this can be seen on figure 4.9.

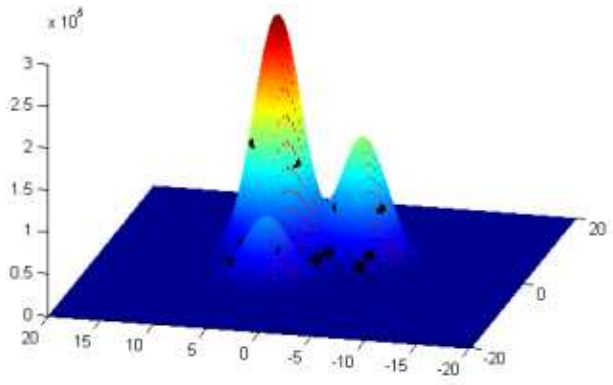

Figure 4.9: *Example of multiple peak splitting. The diffraction intensity found arises from three different diffraction domains located at different positions in the measurement grid. These positions can be found using a multi component least square curve fitting procedure. Axes on the base of the figure is positions in sample coordinates y and z given in μm and the height is the integrated intensity.*

The use of a multi component least squares curve fit solves some of the overlap problems but not all. If the diffraction spots are close in (ω, η) space and in spatial coordinates then it is not possible to split these spots.

From the fitted integrated intensities volumes can be calculated using the method described in section 3.2.3. An example of this can be seen in figure 4.10.

4.3.5 Evaluation

The 5D approach is a faster analysis program than the first approach and, it has furthermore the ability to split multiple peaks. With this program it is now possible to perform the entire analysis in one linked suite of programs. Consequently an entire experiment may be analysed in a few days or weeks depending on the structure of the data images and the available computer power. The program identifies all of the diffraction spots when they appear

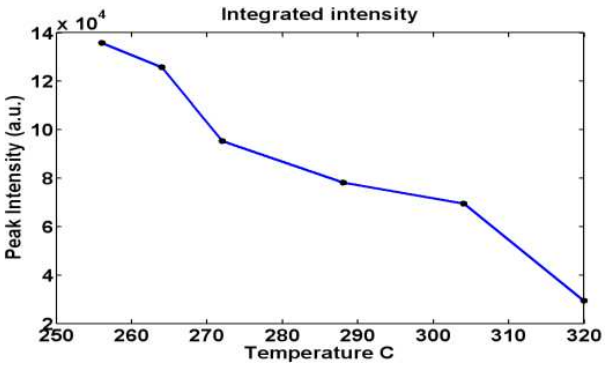

Figure 4.10: *This is an example of a result obtained using the 5D spot finding algorithm. A diffraction spots is located in the same area of the 4D (ω, η,y,z) subspace during a time sequence of the experiment (a string in the 5D space). The experiment is described in section 5.2.*

in the time series, thereby decreasing the bias in choosing specific diffraction spots for the analysis.

The separation of multiple spots in an image or multiple blobs in a higher dimensional space can also be achieved by a watershed algorithm (Roerdink and Meijster (2000) provide a review on watershed algorithms). The combination of a 5D blob finding algorithm using a threshold with the multi component fit is an approximation to a watershed algorithm. But this approximation is believed to be much faster than a full 5D watershed algorithm.

Chapter 5

Results from 3DXRD studies of the evolution of individual subgrains during recovery

In this chapter two different studies of recovery using the 3DXRD microscope are presented. The first experiment is a feasibility study which provided a number of generic results but which also revealed parts of the method which could be improved. Consequently, a second experiment was performed in which a number of such improvements were made.

5.1 Feasibility study

In this section the first 3DXRD study of recovery is described. This was a feasibility study and the main aim of this experiment was to study *in-situ* the dynamics of some individual subgrains. This work was published (Gundlach *et al.*, 2004a; Gundlach, Pantleon, Lauridsen, Margulies, Doherty and Poulsen, 2004b).

5.1.1 Sample material

The sample material was commercial purity aluminium AA1050 cold-rolled to 38% reduction in one pass with an intermediate draught. This material has been studied and characterised by electron microscopy in previous

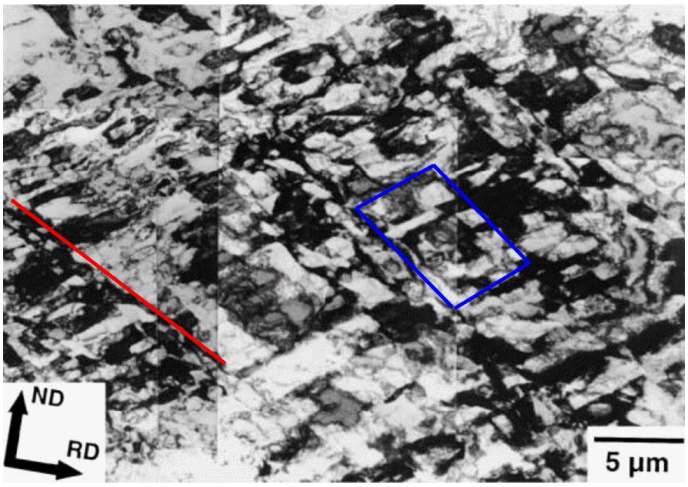

Figure 5.1: *A TEM micrograph of AA1050 cold rolled to 38% reduction. The red line is located next to an extended dislocation boundary and the blue box surrounds a cellblock in the micrograph. Reproduced from* (Delannay *et al.*, 2001).

work (Mishin, Bay and Juul Jensen, 2000; Mishin and Juul Jensen, 1999; Delannay, Mishin, Juul Jensen and Houtte, 2001), (from series A1 of these studies). A TEM micrograph of the material can be seen in figure 5.1. The figure clearly reveals extended dislocation boundaries, which are approximately aligned with an angle of 40° to the RD. The red line in figure 5.1 is an extended dislocation boundary while the blue box surrounds individual cells gathered in a cellblock.

Using mechanical grinding of the sheet material a thin slab was prepared and a 3 mm disc was punched out. By means of electro-polishing analogous to the preparation technique for foils suitable for TEM investigations (see section 3.3.1) a relatively large, thin area of nearly uniform thickness was obtained.

5.1.2 Additional investigations

The sample material was subjected to a few more measurements, one of which was a Vickers hardness test (for description of Vickers hardness tests see section 2.5.2). In the Vickers hardness test five different series of mea-

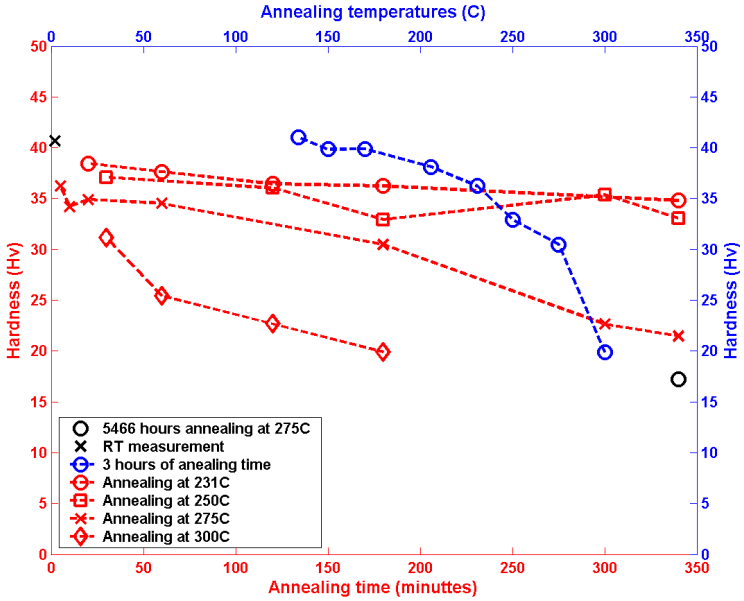

Figure 5.2: *Vickers hardness measurements of AA1050 cold rolled to 38% reduction. Five annealing series are plotted in the figure: Four series with a constant annealing temperatures (231°C, 250°C, 275°C and 300°C, red lines and belonging to the red axis) and one with constant annealing time (3 hours, blue line and belonging to the blue axis). Axes x_1 and y_1 (both in red) are the annealing time and hardness, respectively. Axes x_2 and y_2 (both in blue) are the annealing temperature and hardness, respectively.*

surements were carried out. Four series with constant annealing temperatures (231°C (○), 250°C (□), 275°C (x) and 300°C (◊)) shown in figure 5.2) and one series with a constant annealing time of 3 hours at different temperatures displayed as ○ in figure 5.2). All measurements were carried out on different individual samples, which were immediately put in cold water after the end of the annealing time to stop thermally-activated processes continuing while the sample was cooling down.

The results of the Vickers hardness tests are shown in figure 5.2. From the figure it can be seen that annealing at constant temperatures 231°C and 250°C only slightly decreased the hardness of the material. In contrast, annealing at a constant temperature of 300°C, the hardness decreases rapidly. In between these two types of behaviour are the results of annealing with a

temperature of 275°C. In the figure are also the results from two other hardness measurements: 1) the result from a sample annealed for 5466 hours at a constant temperature of 275°C and thereby fully recrystallised (represented by ∘ in the figure) and 2) the result from one hardness measurement of an as-deformed sample (represented by x in the figure). In none of the measurement series having 3 hours of annealing did the samples reach a hardness equal to the one of a 5466 hours annealed fully recrystallised sample.

In measurements with a constant annealing time of 3 hours, only a small decrease in hardness is detected with annealing temperatures below 250°C while a larger drop in hardness is observed between 250°C and 300°C, in agreement with findings from annealing at constant temperature. It may also be seen in this figure that any annealing above 231°C — even for just a few minutes — results in a decrease in hardness. This indicates that there exist some rapid thermally-activated processes. It may be argued that recovery is the only process observed when the annealing temperature is at 231°C and 250°C, and recrystallisation is the main process at higher temperatures. A combination of recovery and recrystallisation may be seen in the results from annealing at 275°C where there is a small nearly linear part followed by a drop after 180 minutes of annealing.

The material was also investigated by means of EBSD (a description of EBSD is found in section 2.5.1). EBSD was used in order to get a general view of the homogeneity of the sample material. Annealed samples were cut into two parts (along the (TD,ND) plane); one for the hardness investigations and the second to be used in EBSD investigations. An orientation map of the sample materials has been acquired both for the as-deformed material and for material annealed at different temperatures and times. Orientation maps for a sample of the as-deformed material and for a sample of the material that has been annealed at 231°C for 3 hours may be seen in figure 5.3 and figure 5.4, respectively.

In the orientation map of the as-deformed sample small misorientations (thin black lines marks 3° misorientation) are seen inside each grain. If 1° misorientation would be outlined almost every pixel in the image would be surrounded by a thin line. No favoured location for recovery in the as-deformed sample is obvious.

In the orientation map of the annealed sample (figure 5.4), it can be seen that different areas of the sample have recovered more than other parts of the sample. This is in contrast to the hardness investigations which averages over lager areas discussed above, which showed very little change in hardness

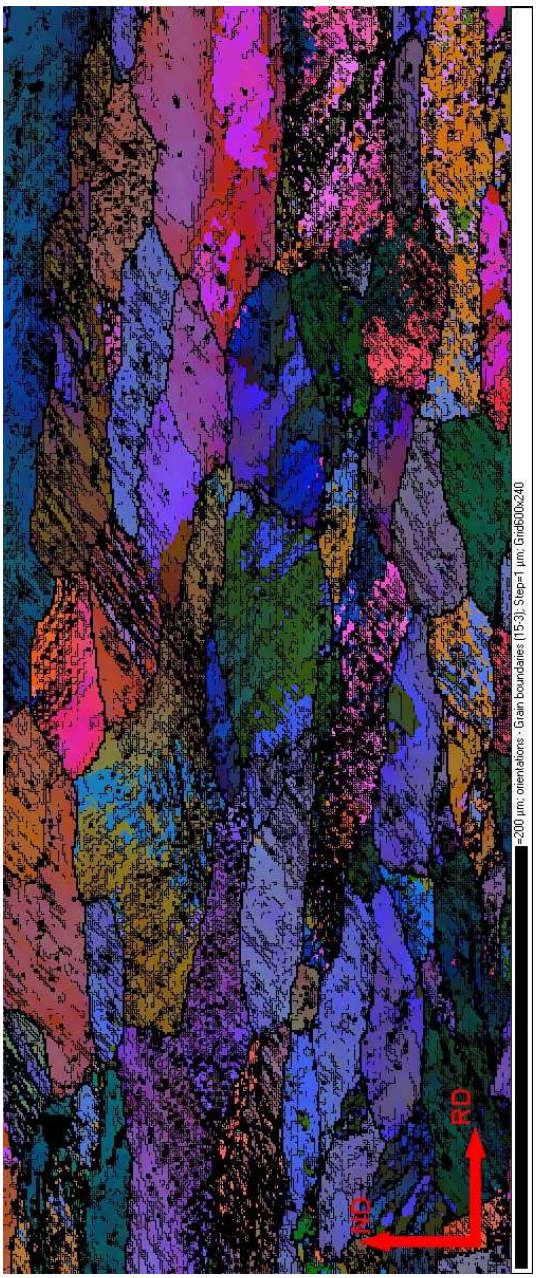

Figure 5.3: *EBSD orientation map of an as-deformed sample. Misorientations larger than* 3° *are marked with thin black lines and and misorientations larger than* 15° *are marked with thick black lines.*

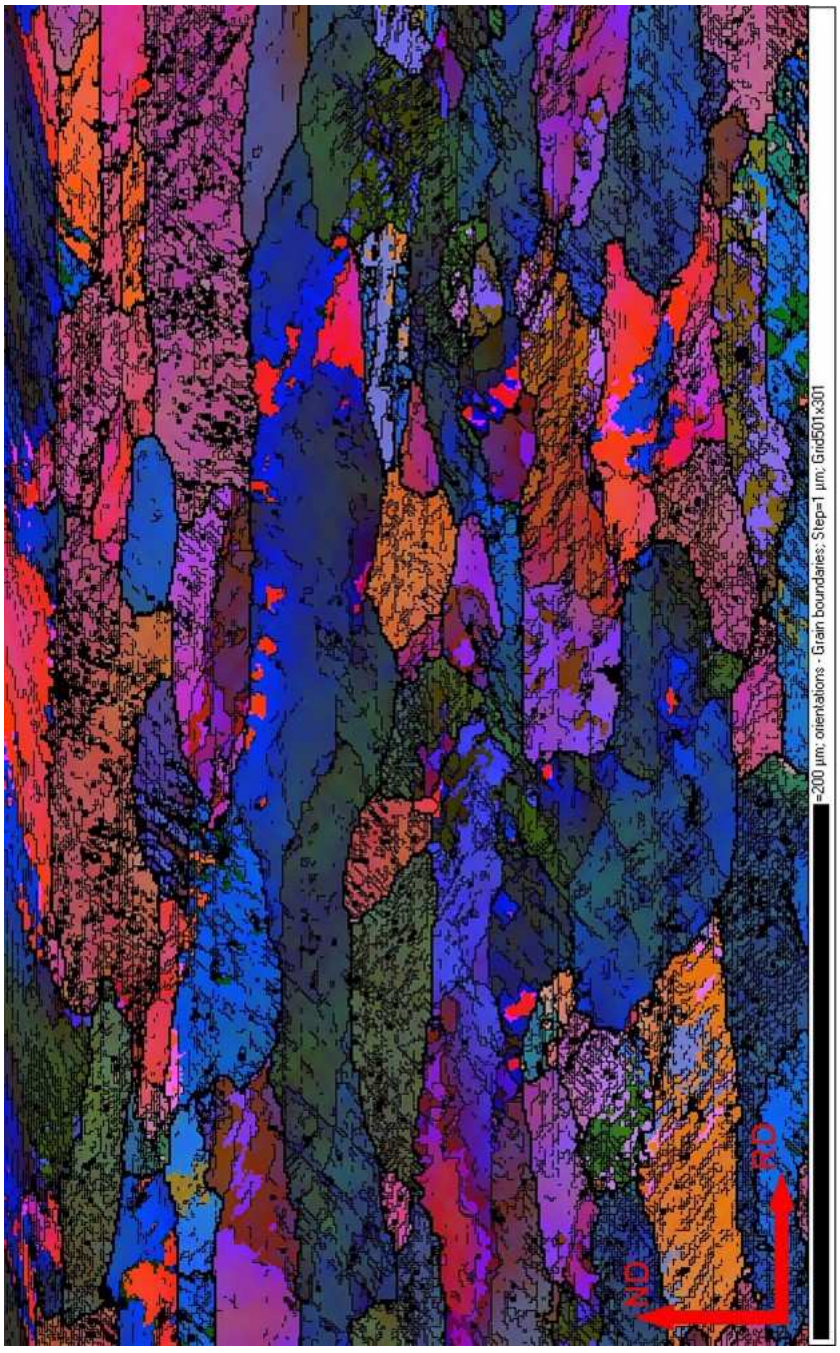

Figure 5.4: *EBSD orientation map of an sample annealed at* $231°C$ *for 3 hours. Misorientations larger than* $3°$ *are marked with thin black lines and and misorientations larger than* $15°$ *are marked with thick black lines.*

after 3 hours annealing at 231°C. The combination of this and the fact that there are no fully-recrystallised grains in the orientation map suggests that the dominating processes are recovery processes.

This inhomogeneity of recovery causes problems for the 3DXRD study because the size of the X-ray beam makes it a localised study within one of the deformed grains, or around a boundary between two deformed grains.

Based on the Vickers hardness tests and EBSD material investigations it was decided that an annealing temperature at 300°C should be used in the 3DXRD experiment. At this temperature recovery should be found in all grains, which should minimise the possibility of the X-ray beam hitting a grain with no recovery. On the other hand it increased the possibility of a grain recrystallising in or near the area subjected to X-ray investigations. In such a case diffraction spots from subgrains would disappear from the detector and leave a few large diffraction spots from the recrystallised grain. Significant recovery must occur in the time frame of the the 3DXRD experiment (i.e. within a few hours).

5.1.3 Experimental procedures

The experimental 3DXRD method used in this study is described in detail in section 3.3.

The disc was mounted in a massive copper holder together with a copper ring upon which L-shaped gold markers had been deposited. The two legs on these markers were 400 μm long and 100 μm wide. The markers were deposited by photo-lithography and was 300 nm in height. The internal corners of these markers served as reference position to ensure that the same area of the disc was illuminated during the experiment. The sample holder was placed in an X-ray transparent furnace. The furnace was mounted on top of an (x, y, z)-translation stage and an ω-rotation stage. Finally the disc was positioned in the focal spot of the beam.

The furnace was basically a heating element made from copper with a copper rod in the centre. Located inside the copper rod was a thermocouple to measure the temperature at the end of the copper rod. The sample holder was mounted in this copper rod. To ensure a good thermal conductivity and identical thermal expansion of the sample holder and the furnace rod the sample holder was consequently manufactured in copper too. A photograph of the special formed sample holder is displayed in figure 5.5.

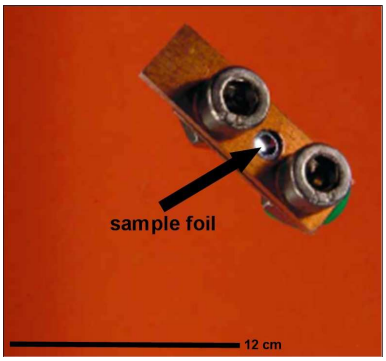

Figure 5.5: *Photograph of the sample holder. The thin sample foil is the small shining object in the middle of the sample holder at the end of the black arrow.*

5.1.4 Measuring procedure

The objective of the experiment was to determine the volume of a set of subgrains as function of annealing time. This can be accomplished by repeatedly determining the centre-of-mass position on the detector and the integrated intensity of a set of diffraction spots. As described in section 3.3.3, data acquisition was performed in a (y, z) grid on the sample due to the Gaussian X-ray intensity beam-profile. In this experiment the measurement grid was a 3×3 grid, with 5 μm between the grid points. Five different rotation (ω) positions were used, namely -2°, -1°, 0 °, 1° and 2° where 0° is the position where the sample is perpendicular to the X-rays. At each position the sample was rotated by $\mp 0.5°$ around the nominal ω-value. The data acquisition sweep is described in section 3.1.7.1.

The experiment was initiated by selecting and characterising a suitable area of the sample with a superior density of resolvable diffraction spots. The area was defined by a position vector to the reference L-shaped gold markers. The position of the L-shaped gold markers was found using the X-ray fluorescence signal from the gold. The sample was then heated from room temperature to 300°C in 3 minutes. During the following 181 minutes the temperature was kept constant while continuously repeating the (y, z, ω) grid measurements every 5 minutes. Between each of the 5-minute-sets of observations the sample position was re-checked against the L-shaped gold markers, to compensate for thermal expansion of the system.

5.1.5 Data analysis

All X-ray diffraction images were subjected to the background correction method described in section 4.1.1. Because of this background subtraction the resulting images had well-defined single diffraction spots laying on the Debye-Scherrer rings while the amorphous scattering from the glass of the furnace leads to a dark area in the centre of the images (see figure 4.2).

The integrated intensity of a diffraction spot is proportional to the volume of the associated coherently diffracting domain - a subgrain (kinematical scattering). The proportionality constant was calculated by calibrating with respect to a powder specimen of known geometry as explained in section 3.2.3. From the calibration it was also inferred that the detection limit on the diffraction spots corresponded to a subgrain radius of 150 nm.

Furthermore, by scaling the total intensity in specific hkl rings, the thickness of the disc at the illuminated position was determined to be (80 ± 20) μm. Since the mean subgrain size was determined to remain below 2 μm, most of the diffraction spots should be associated with bulk subgrains.

5.1.5.1 Selection of diffraction spots

The analysis method employed in this experiment is described in section 4.2. This was the first approach with an emphasis on the possibility to handle the analysis 'by hand' and thereby making it possible to follow all the steps in the analysis. Large single spots without close neighbouring diffraction spots were selected for the analysis.

5.1.5.2 Validation of the diffraction spot

A squared AOI closely surrounding the diffraction spot was analysed. All intensity within this AOI was used for the analysis. Hence, in the AOI only one diffraction spot should appear and the particular diffraction spot must be located fully within the AOI in all the diffraction images where the diffraction spot was observed. This must be valid for each sample position in the grid and for each ω position. An example of this is presented in figure 5.6.

The validation that only one full diffraction spot is located within the AOI for analysis is performed during the spot finding procedure described in

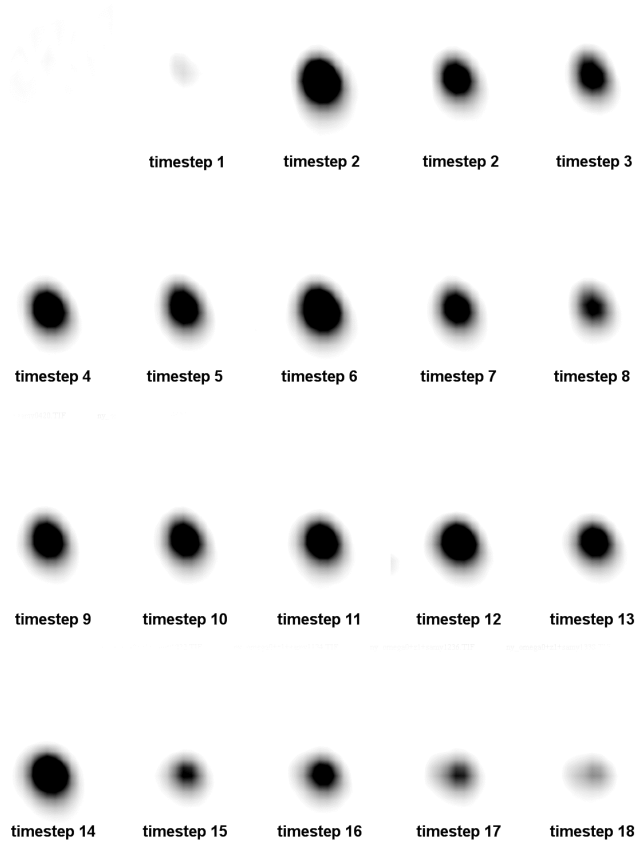

Figure 5.6: *Example of a "mosaic image" of an AOI, at a given* (x, y, ω) *position, used to validated diffraction spots. The image is read from left to right and from top to bottom as a function of time. At each position, all of one and only one diffraction spot must be visible within all positions to be considered valid.*

section 4.2.1. This validation reduces the number of useful diffraction spots. Another output from this procedure is a list of properties for the diffraction spot including the summed intensity within the AOI.

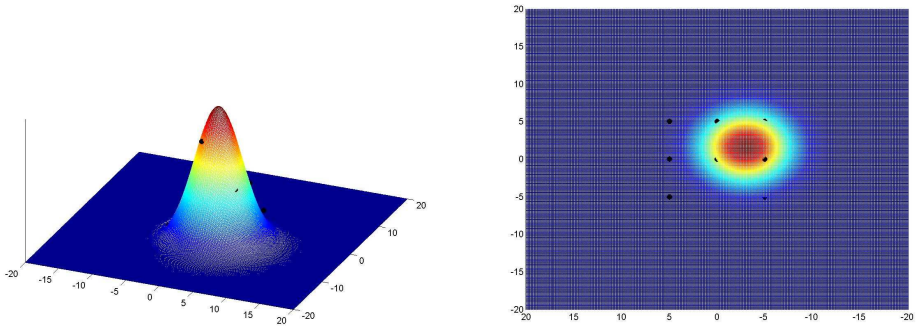

(a) (b)

Figure 5.7: *Overview of result from least squares curve fitting. Black spots are the measured diffraction intensities at each position in the* (x, z) *measurement grid. (a) A view from the side. The surface is calculated from the fitting parameter. (b) A top view which shows the position of the subgrain within the measurement grid. Axes on the base of the figure are positions in sample coordinates* y *and* z *given in* μm

5.1.5.3 Intensity fitting and validation

A least squares curve fitting of the intensities to the known X-ray intensity beam profile was performed on the summed intensity of the AOI in each position in the measurement grid. The result of this fitting procedure was two-fold: firstly the fully-integrated intensity of a diffraction spot was obtained, secondly the position within the measurement grid of the maximum intensity of a diffraction spot was identified. Diffraction spots with maximum intensities at positions within 5 μm from the centre of the measurement grid were considered valid, all other diffraction spots were rejected. An example of the least square curve fitting is plotted in figure 5.7(a) where the black dots represents the measured intensities at each grid point in the measurement grid. The curve is the fitted curve from the X-ray intensity beam profile. In figure 5.7(b) the same curve is displayed in a top view where the position of the maximum intensity may be located in the measurement grid.

5.1.6 Results and Discussion

Taking the fully integrated intensity of a diffraction spot found by the least squares curve fitting, the true volume of the corresponding diffraction domain interpreted as a subgrain volume can be calculated as described in section 3.2.3.

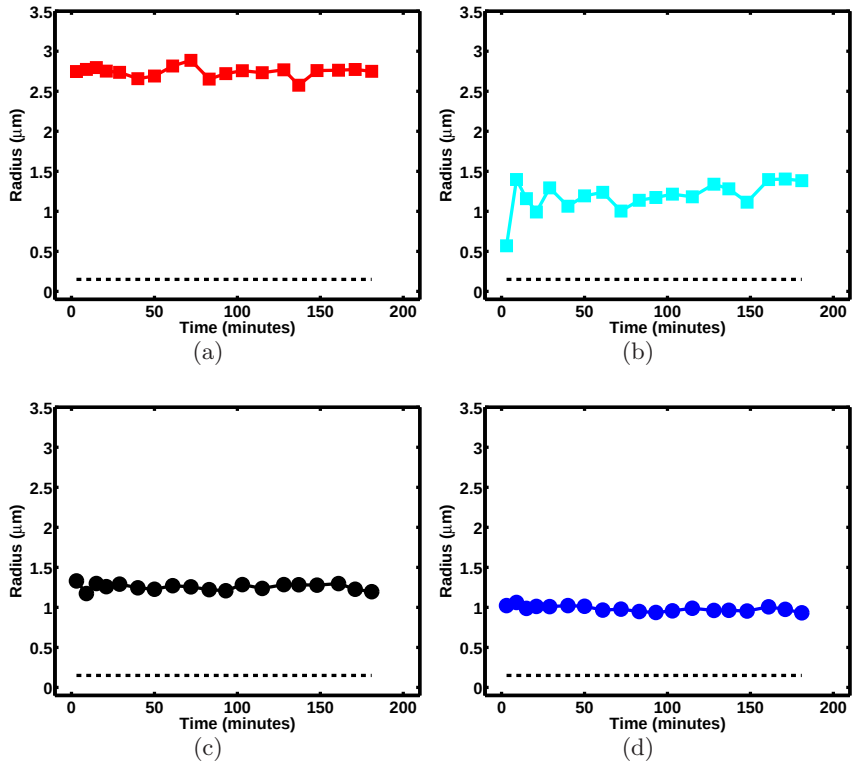

Figure 5.8: *The evolution in size of nine individual subgrains. The ESR is plotted as a function of annealing time. The dashed lines in the figures are the detection limit of 150 nm. (a), (c), (d), (h) and (j) exhibit essentially no growth. (g) and (i) shrink during the first hour. (b) grows rapidly during the first 5 minutes. (f) initially grows but shrinks after 100 minutes annealing.*

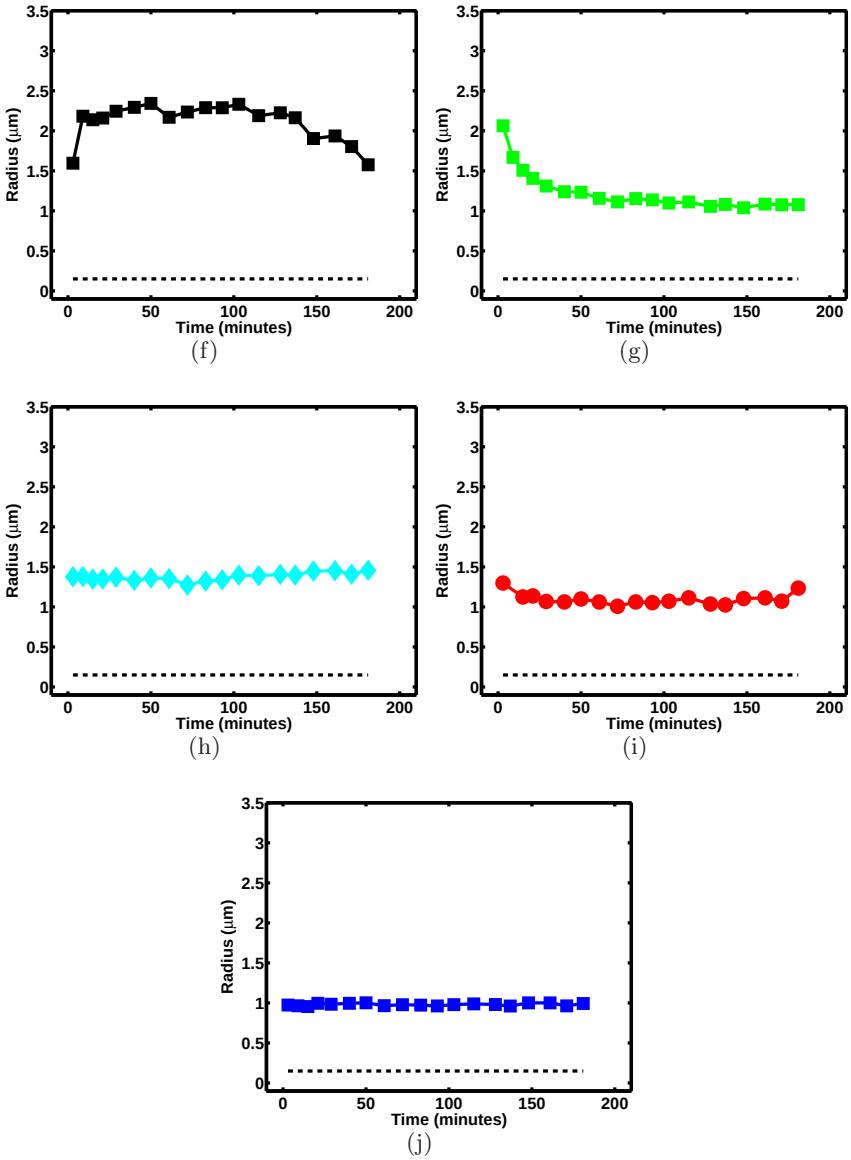

Figure 5.8: *The evolution in size of nine individual subgrains. The ESR is plotted as a function of annealing time. The dashed lines in the figures are the detection limit of 150 nm. (a), (c), (d), (h) and (j) exhibit essentially no growth. (g) and (i) shrink during the first hour. (b) grows rapidly during the first 5 minutes. (f) initially grows but shrinks after 100 minutes annealing.*

5.1.6.1 Dynamics of subgrain growth

In the following results for the dynamics of nine individual subgrains, which fulfil the validation criteria described above, are presented. Inserted in the figures is the detection limit, which is by analysing the noise in the diffraction images and which corresponds to subgrain radii of 150 nm.

The evolution in the true volume is shown in Figures 5.8(a)–(j). Among the subgrains, more than half exhibit essentially no growth (in figures 5.8(a), 5.8(c), 5.8(d), 5.8(h) and 5.8(j)), two shrink during the first hour and then stay constant (see figures 5.8(g) and 5.8(i)), one grows rapidly during the first 5 minutes after which it stagnates (see figure 5.8(b)), while the last one initially grows and finally shrinks (see figure 5.8(f)). In general all the curves exhibit a smooth evolution. Strikingly, there is no obvious correlation between subgrain volume and growth behaviour. The smallest subgrain (the one in figure 5.8(b)) exhibits a substantial growth during the first 3 minutes as does the rather large subgrain in figure 5.8(f). On the other hand, one of the larger subgrains shrinks during the observation and the largest one does not change in size at all.

5.1.6.2 Histogram analysis

A statistical analysis was made on this data set; this method is described in section 4.1.3. Histograms of the apparent subgrain sizes as derived from 500 diffraction spots are presented in Figure 5.9 for the as-deformed state and after 3 and 181 minutes of annealing at 300°C. Essentially all non-overlapping spots in the images are included in this analysis, irrespective of whether they are valid and whether they are the same spots that appear at the three stages or not. Note, that the apparent subgrain volume is the result of a convolution of the true subgrain volume with the Gaussian beam profile. From simulations based on a log-normal distribution of the true subgrain radii ESR, an average true subgrain radius of 1.2 μm is obtained by fitting the room temperature data. This is in agreement with estimations from TEM investigations on the same material (see figure 5.1) and corroborates the interpretation of the diffraction spots as arising predominantly from individual subgrains. After annealing for 3 minutes the average true subgrain size increased to 1.6 μm and even further to 1.7 μm after 181 minutes. Evidently, substantial coarsening has occurred during the 3 minutes of heating up and the duration of the first grid measurement at 300°C, while the amount of coarsening taking place during the following 3 hours is small.

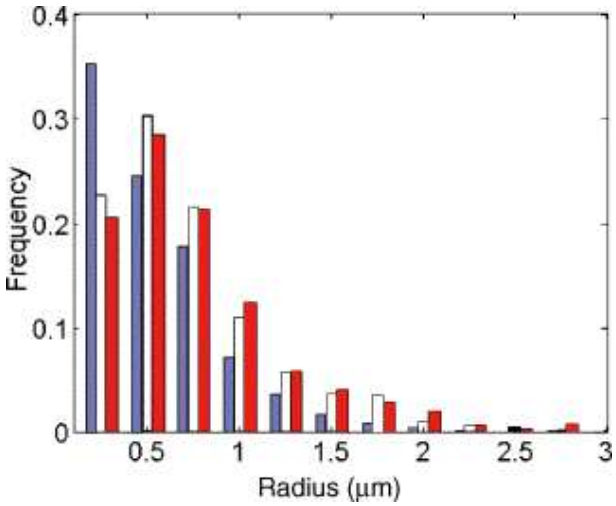

Figure 5.9: *Histogram of true subgrain radii obtained from 500 individual diffraction spots. Measured in the as-deformed state (blue), after 3 minutes of annealing (white) and after 181 minutes of annealing (red) at* $300°C$.

5.1.6.3 Discussion

The resulting individual growth curves are in marked contrast with elementary theories of curvature driven coarsening, e.g. (Humphreys and Harherley, 1995; Jones *et al.*, 1979)(see description of curvature driven coarsening in section 2.4.1), where subgrains larger than average are expected to grow while subgrains smaller then average are expected to shrink. However, this behaviour might be strongly affected by the local neighbourhood of the individual subgrains. From the small number of subgrains observed it cannot be excluded, that a curvature-driven model is valid in a statistical sense. Analysis of a larger number of subgrains is required to resolving this issue.

In Abbruzzese and Lücke's (1986) model each subgrain orientation has its own critical size, above which subgrains are expected to grow. It is possible that this model might describe the observed behaviour of the subgrains, but since the total orientations of the subgrains were determined this question cannot be answered.

In order to determine whether any of the nine validated subgrains rotated during the annealing the centre-of-mass position of the diffraction spots on the detector and the ω bin positions were monitored. The rotation of subgrains is interesting in order to test if there was any sign of coalescence (see section 2.4.2). For eight of the reflections no rotation was detected within the experimental accuracy, estimated to be 0.3°. For the subgrain in figure 5.8(g) the centre-of-mass position of the diffraction spot on the detector changed by 1° along η during annealing. However, this particular diffraction spot initially exhibits an orientation spread of 1.2° and may consist of contributions from different subgrains. This is further supported by a closer inspection showing that the change in η is caused mainly by the vanishing of part of the diffraction spot corresponding to the disappearance of a subgrain of a slightly different orientation; this disappearing subgrain is then of even smaller size.

5.1.6.4 Conclusions

1. A unique diffraction technique has been established, enabling *in-situ* studies of the dynamics of individual subgrains during recovery.

2. Statistics on subgrain size distributions in the first experiment implies that most of the subgrain coarsening occurs during heating up and the first 3 minutes of annealing.

3. The growth curves for the individual subgrains are different from the average behaviour for a subgrain of a given size as predicted by deterministic models based on interfacial energy driven mechanisms.

4. Within the accuracy of the method no rotation of the nine observed subgrains could be detected during annealing.

5.2 Experiment on AA1200

Analysing the first experiment a number of problems related either to the data acquisition or to the sample were observed. A second experiment was performed in which a number of improvements dealing with these problems were made.

5.2.1 Improvements

In the first experiment, for the majority of the detected diffraction spots, the position of the maximum intensity was not located within the centre of the measurement grid and consequently the spot could not be validated. In order to increase the number of diffraction spots within the validation region of the measurement grid, the grid was expanded to a 4×4 grid. The expansion from a 3×3 to a 4×4 grid almost doubled the number of measurement points from 9 to 16, thereby worsening the time resolution also by a factor of almost two. This effect was countered by the development of a new type of ω-scan, the sweep-scan (see section 3.1.7.2).

The combination of the expansion of the measurement grid and the development of the sweep-scan resulted in a substantially better time resolution than in the first experiment. It was therefore decided to increase the number of ω bins increase from 5 to 32 ω bins. The resulting time resolution was of the same order as in the first experiment. The total time of the acquisition scan was 15 minutes.

The expansion of the measurement grid and the increase of ω bins resulted in an increased number of diffraction images acquired. The increased number of diffraction images was a challenge to handle computationally and consequently new software including a new algorithm to locate the diffraction spots was developed. The details of the new algorithm are discussed in section 4.3.

5.2.2 AA1200 material

The sample material used in the experiment was an aluminium alloy, AA1200. The original grain size in the material was 75 μm and the material had been cold rolled to a true strain of $\epsilon = 2$. This type of material has been characterised by TEM (Liu, Huang, Lloyd and Hansen, 2002). Subgrain sizes in the as-deformed material were found to be about 1 μm in the rolling

direction and about half of that in the normal direction. Annealing studies have been performed by Xing, Huang and Hansen (2004) in which they observed: Structural changes after annealing at 200°C for 2 hours, specifically some regions started to coarsen and equiaxed subgrains were formed. After annealing at 220°C for 2 hours they observed more general structural changes, in which two main types of regions were observed: 1) One type exhibited equiaxed structures with sharp boundaries and a very small dislocation content between the boundaries. 2) The other type consisted of the same lamellar structures found in the as-deformed state. A correlation between the type of region and the local crystal orientation was observed, showing regions with a rolling texture having only few structural changes.

The texture of this material was more random than the texture of the AA1050 cold rolled to 38% reduction that was used in the first experiment. The random texture resulted in less overlapping of the diffraction spots on the Debye-Scherrer rings despite the smaller subgrain size. If diffraction spots are spread out through the full Debye-Scherrer rings the number of isolated diffraction spots is increased, hence improving the data from the 3DXRD microscope.

5.2.3 Experimental setup

The experimental setup of the 3DXRD microscope was similar to the one described in section 3.3 and section 5.1.3 together with the improvements described in section 5.2.1.

In order to ensure that recovery occurred in the measured region of the sample it was decided to start annealing at 200°C for 50 minutes and then increase the temperature by 8K after each completed cycle of the measurement grid in this way imitating isochronal annealing. The final temperature was 376°C. The annealing history of the experiment can be seen in figure 5.10.

The main difference between the experiment described in section 5.1.3 and this experiment was the shape of the focused X-ray beam. In this experiment the tails of the beam, that is the parts of the beam outside the FWHM of the beam intensity profile were much more intense. This intensity in the tails gave rise to diffraction from subgrains outside the desired region of the sample, thereby increasing the amount of overlapping diffraction spots on the detector. As the optic elements and optics alignment procedure were the same as in the first experiment, the increased intensity in the tails is believed to be due to deterioration of the optic components. The

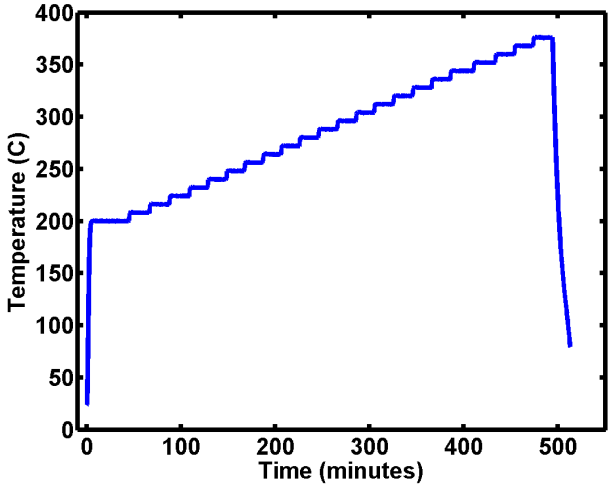

Figure 5.10: *Annealing history of the AA1200 sample. After initially annealing at* 200°C *for 50 minutes the temperature was stepped up by* 8K *after each measurement cycle. The final temperature step was to* 376°C.

problem was partially solved by using the second part of the double slit system installed between the optics and the sample. This last set of slits -the guard slits- were used to cut some of the X-ray beam tails. The reason for using the last set of slits instead of the normal first one was because the last set is closer to the sample. The drawback of using the second set of slits was that possible scattering from these slits could not be blocked, and in fact some scattering from the slits can be seen in the diffraction images. The double slit system was then positioned as close as possible to the sample, and hence some of the X-ray beam tails were reduced.

5.2.4 Results

Histograms of apparent subgrain sizes were calculated analogous to those in section 5.1.6.2 (see section 4.1.3 for the details of the algorithm). During the experiment some measurements were done with an attenuated X-ray beam in order to ensure that no diffraction spots saturated the detector pixels. If a diffraction spot would saturate the detector, a volume increase of the diffracting subgrain could not be detected. A weak beam intensity results in fewer diffractions spots on the detector, especially diffraction spots from

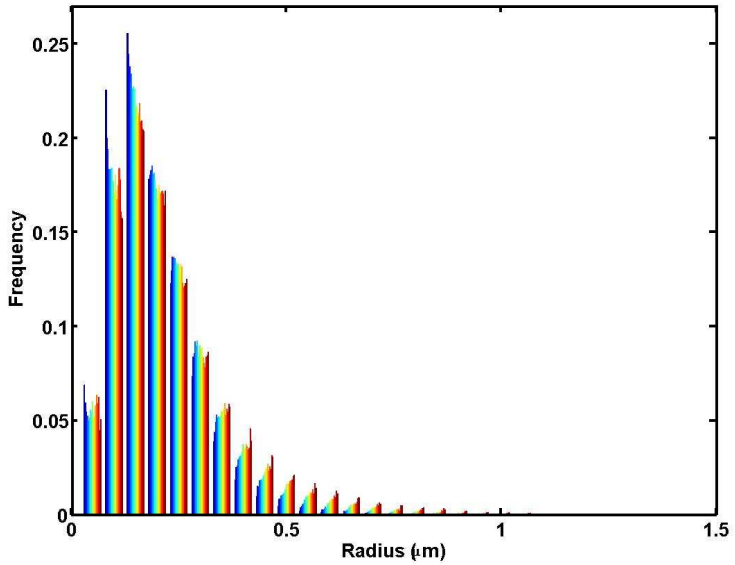

Figure 5.11: *Histogram of appeared subgrain sizes in AA1200 from all measurements without any attenuation in the beam. In each block the left side represents the lowest temperature and the right side the highest temperature.*

subgrains laying in the tails of the X-ray beam which may be to dim to be detected. Therefore the number of detected diffraction spots in the recorded images while switching between different attenuation levels will oscillate and consequently it makes more sense to study the measurement grids with the same attenuation level. However, with or without the attenuation the results were biased towards smaller sizes due to the tails. The effect was assumed to be less significant with more attenuation.

The histograms in figure 5.11 were calculated from measurements without any attenuation. The histograms show a slow increase in subgrain sizes with annealing time (and temperature). In the figure it can be seen that for smaller subgrains the number decreases more rapidly. The bin with subgrains of a radius of 0.1 μm is shrinking quicker than the one with subgrains of a radius of 0.15 μm. The turning point is in the bins of 0.25 μm and 0.3 μm where the frequency increases during the first part of the annealing and then begins to decrease in the second part of the annealing. From 0.35 μm the frequency increases with annealing. The figure also implies

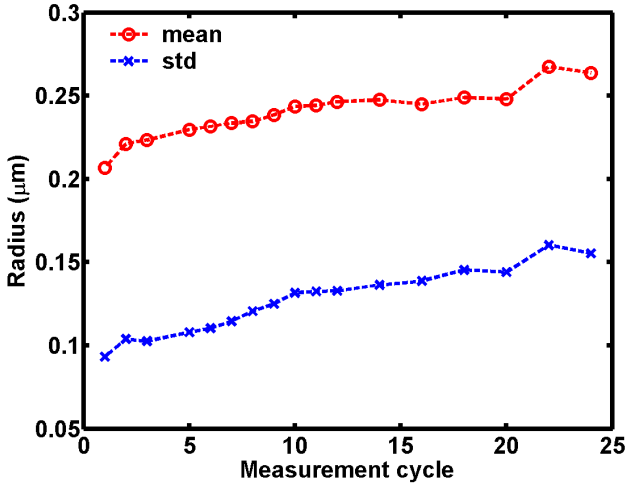

Figure 5.12: *Average apparent subgrain sizes and standard deviation during annealing of AA1200. Only measurements without attenuation were used. The annealing history can be seen in figure 5.10.*

that during the first measurement none or only a few subgrains were detected having a radius bigger than 0.7 μm whereas at the end of annealing subgrains were detected with radii up to 1.1 μm.

The growth of the subgrain sizes is also evident from the averages of apparent subgrain sizes, which are plotted in figure 5.12. The figure illustrates that the mean subgrain radius smoothly increases from 0.21 μm to 0.26 μm during annealing while the standard deviation also increases, indicating a bigger spread in the radii of the subgrains.

The shape of the subgrain size distribution changes during annealing as characterised by its moments. Figure 5.13 shows the ratio between average size and standard deviation is decreasing (remembering the increasing mean and standard deviation observed in figure 5.12), this shows that the distributions are changing and do not keep the same shape around the mean value. The increase in skewness of the subgrain size distributions also reflects the shape change of the distributions (see figure 5.13).

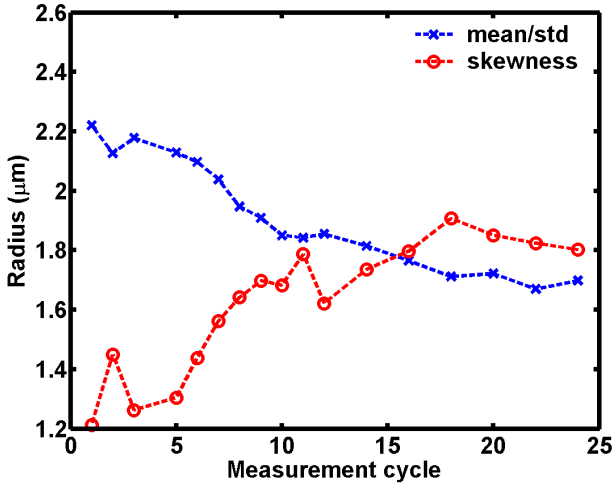

Figure 5.13: *Skewness of subgrain size distributions and mean/standard deviation during annealing of AA1200. Only measurements without attenuation were used. The mean and the standard deviation of the subgrain distribution are displayed in figure 5.12 and the annealing history can be seen in figure 5.10.*

5.2.5 Sample thickness

The thickness of the sample in the measurement region is difficult to measure. Using the integrated intensity over one Debye-Scherrer ring and comparing this to the response of a sample of known thickness is a method with some degree of uncertainty. Not all orientations are measured which means that the texture will influence the results. Nevertheless the thickness was calculated with this method. Three different Debye-Scherrer rings were used yielding results between 2 μm and 5 μm.

As an alternative it was decided to measure the thickness of the sample by the use of a FIB microscope. The idea was, by means of ion bombarding, to sputter a hole in the sample just on the edge of the region used by the 3DXRD microscope. After the hole was sputtered, the sample was tilted in such a way that it was possible to scan the wall of the hole next to the area subjected to the 3DXRD measurement. In this way the height of the hole was estimated to be 4 μm. It was assumed that the gradient of the thickness profile of the sample foil was small and consequently the area measured by

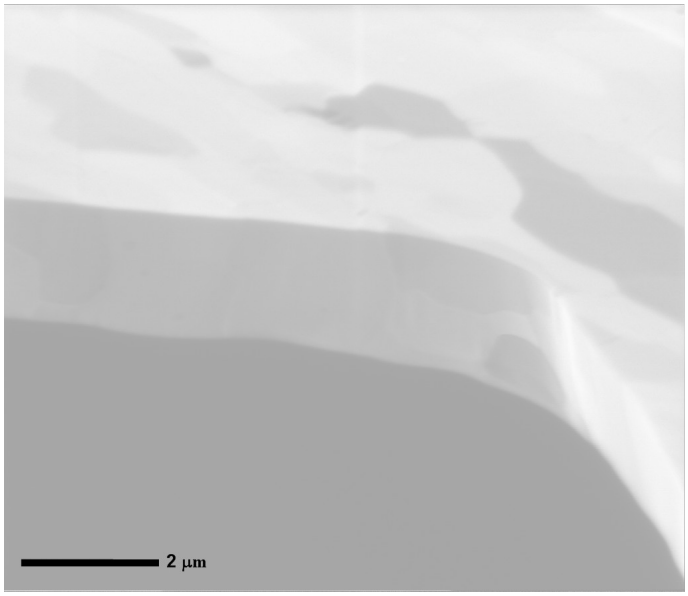

Figure 5.14: *FIB image of an AA1200 sample with a sputtered hole. The ion beam was focused at the corner of the sputtered hole next to the region subjected to 3DXRD measurements. The different contrast observed within the foil originates from different orientations of different subgrains.*

3DXRD was 4 μm thick. 4 μm was within the range of the expected thickness from the 3DXRD calculations described above. An image of the edge of the sputtered hole in the sample taken with the FIB microscope is displayed in figure 5.14. In the figure it is possible to see orientation contrast and some subgrains are visible. Due to focusing problems it was not possible to get better orientation contrast but similar investigations have been performed[1] and in these images subgrains are seen to fill the wall of the hole entirely.

5.2.6 Experimental problems

In carrying out this experiment some problems were encountered which resulted in fewer results than in the first experiment. Those problems will be discussed in this section.

[1] FIB investigations by J. R. Bowen, private commination

One problem was finding diffraction spots from the same subgrain during annealing. With the use of gold markers to ensure that the same area of the sample was exposed during the experiment, it was a surprise that most diffraction spots were only located within the measurement grid in a few time steps. It seemed that the combination of increasing temperature and the use of gold markers as position reference led to some error. Thermal expansion follows the increase in temperature, and hence causes a change in the position of the motor translating the sample to the position of the edge of the gold marker. Examination of these motor positions showed that the positional change has been irregular, which indicated that the thermal expansion was not completed before the location of the marker was obtained. This was in contrast to the isothermal annealing in the first experiment where the thermal expansion reached equilibrium and the gold markers were used to correct for small drifts in the microscope.

Another problem already mentioned in section 5.2.3 are the tails of the X-ray beam. Due to the tails a much larger area of the sample is exposed and more subgrains are diffracting leading to an enhanced spot overlap. In comparing this experiment with the first experiment, it is observed that spot overlap is a bigger problem for the present experiment even though the choice of material should decrease the spot overlap on the following two accounts: 1) the random texture compared to the rolling texture normally found in material lightly deformed by cold rolling, and 2) the reduction factor of 10 in thickness.

The spot overlap caused a third problem related to the sample thickness. The region subjected to measurement was chosen by inspection as a tradeoff between the number of diffraction spots and the spot overlap. The erroneous assessment of the beam profile implied that the foil thickness at the region investigated was in fact too thin for a "bulk" study.

The data analysis approach described in section 4.3 using a 5D space was tested on the data acquired from this experiment. But due to the problem of thermal expansion just explained only fragments of "diffraction strings" (restricted growth curves) was detected in the 5D space and the data analysis was terminated. One such fragment is presented in figure 4.10.

Chapter 6

Summary and outlook

6.1 Summary

The aim in this Ph.D. project has been to extend the use of the 3DXRD microscope to smaller scales, thereby making it possible to study the dynamics of subgrains. Subgrain sizes are approximately of 100 nm to 2 μm. The dynamic process studied during annealing is recovery. Two experiments using the method developed have been presented in this thesis and the main findings are summarised below:

1. A unique diffraction technique was developed, which enables *in-situ* studies of dynamics of the individual subgrains during recovery.
2. An analysis of subgrain size distributions indicated that subgrains coarsening mostly occurs during the heating up and the first 3 minutes of annealing for a recovery study of an aluminium alloy (AA1050) cold rolled to 38% reduction.
3. The growth curves for individual subgrains are different from the average behaviour for a subgrain of a given size as predicted by standard deterministic models based on interfacial energy driven mechanisms.
4. No rotation of the nine observed subgrains could be detected during annealing within the accuracy of the method developed.
5. The image analysis algorithms known as Connected Components and Labelling have been extended to 5D space, thereby enabling blob finding in 5D space.

6. Incorporating a multi-component fit in the blob finding analysis tool provides a fast approximation to a watershed algorithm.
7. It was found from the experiment on AA1200 that isochronal annealing is challenging because even a small thermal expansion is critical when using micro-beams.
8. The analysis based on apparent size distributions provides information on the evolution of distributions.

6.2 Outlook

To test theories on recovery in general, the aim would be to gather an ensemble of hundred(s) of individual growth-curves. Due to the experimental problems encountered (see section 5.2.6) this aim was not achieved within the time-frame of this Ph.D. However, in my view the aim is clearly reachable. In that connection it may be instructive to compare with the progress in growth curve studies of recrystallisation. Here the first study comprised 6 grains (Lauridsen *et al.*, 2000) while a study 3 years later dealt with the dynamics of 240 grains (Lauridsen *et al.*, 2003). As an example of scientific issues that could be addressed if such ensembles were available, I mention the relative importance of coalescence and coarsening and the question of whether the coarsening can be described by conventional grain-growth models.

Extending the data acquisition to a larger ω-range will enable an analysis based on the multi-crystal indexing program GRAINDEX (Lauridsen *et al.*, 2001) (for description of GRAINDEX see section 3.1.9) and provide the full orientation of each subgrain and its elastic strain tensor (Poulsen *et al.*, 2001).

Furthermore, by indexing subgrains and acquiring data over a larger ω-range it will be possible to determine the 3D centre-of-mass position of each subgrain within the sample, based on triangulation of two or more diffraction spots. If the reflections used span 90° in ω, the accuracy will match the 1-2 μm found from the (y, z) fit of the measurement grid.

6.2.1 Sample preparation by FIB

One of the main problems has been the sample preparation and especially the achievement of a homogenous area of the desired thickness. One solu-

tion to this problem could be to roll the material to the thickness wanted. Aluminium sheets with a thickness down to 10 μm are rolled in industry and can be found in almost every household as aluminium kitchen sheets. An attempt was made to cold roll a sheet of AA1050 to 10 μm thickness with a deformation of 40% reduction in thickness. This attempt was unsuccessful because the aluminium sheet turned sidewards under the rolls in the rolling mill. The result was a visible shear in the sheet.

One possible way to prepare a sample could be by the use of a FIB. Providing that the FIB removal rate is known for the given material, it would be possible to sputter a cavity with the desired dimension in the sample. This is a time consuming task and therefore requires easy access to a FIB. The time could be reduced by rolling the material to the smallest possible thickness before drilling.

6.2.2 Novel X-ray optics

Another critical issue is the problem of the tails in the X-ray beam profile which results in spot overlap. A recent suggestion, for a novel X-ray optics setup could be the solution[1]. Two specially designed X-ray lenses are used to first condense the beam and then produce an exit beam with low divergence and a uniform beam profile (at least in the centre part). Simulations indicate that it is possible in this way to focus the beam down to a size in the range of 10-20 μm in two directions. Then, it would be possible to define the X-ray beam by slits. In such a situation the method developed to study subgrain evolution described in this thesis would be outdated. The validation based on the measurement grid could be replaced by the validation method previously used in recrystallisation studies, that is opening and closing the slits as described in section 3.2.2. In a case without a measurement grid the sample would stay fixed in the beam, and time resolution would improve by a factor equal to the number of grid positions in the measurement grid. Consequently, it would be possible to expand the ω-scan range by an order of magnitude without deteriorating the time-resolution, and thereby increasing statistics and enabling determination of the full orientations of the subgrains.

[1] G. Vanghan, private communication

6.2.3 Nanoscope

The beamline ID11 at ESRF is currently in the process of expanding the beamline in such a way that it will be possible to focus the X-ray beams in the 30-100 keV range down to sizes around 100 nm. A dedicated instrument — the nanoscope — for utilisation of such beams is being constructed. With the nanoscope it will be possible to study the dynamics of embedded crystalline nano-structures. These dynamics are a topic of much interest currently, e.g. in connection with the stability of nano-materials towards heating. The limiting size of detection of such structures is estimated to be ≈ 20 nm. However, according to current plans the focusing of X-ray beams to sizes of 100 nm will not provide an uniform intensity profile. Hence, the method to characterise such nano-structures will have to be analogous to the method developed in this thesis to analyses of subgrains in deformed structures on a micrometre scale.

Bibliography

Abbruzzese, G. and Lücke, K.: 1986, A theory of texture controlled grain growth-I. Derivation and general discussion of the model, *Acta Metall.* **34**(5), 905–914.

Als-Nielsen, J. and McMorrow, D.: 2001, *Elements of ModernX-ray Physics*, 1 edn, John Wiley & Sons Ltd., Chichester, UK.

Atkinson, H. V.: 1988, Theories of normal grain growth in pure single phase systems, *Acta Metall.* **36**(3), 469–491.

Bay, B., Hansen, N., Hughes, D. A. and Kuhlmann-Wilsdorf, D.: 1992, Evolution of F.C.C. deformation structures in polyslip, *Acta Metallurgica et Materialia* **40**(2), 205–219.

Bay, B., Hansen, N. and Kuhlmann-Wilsdorf, D.: 1992, Microstructural evolution in rolled aluminium, *Material Science and Engineering A* **158**(2), 139–146.

Beck, P. A.: 1954, Annealing of cold worked metals, *Advances In Physics* **3**(11), 245–324.

Bässmann, H. and Besslich, P. W.: 1991, *Bildverarbeitung Ad Oculos*, 1 edn, Springer-Verlag, Berlin, Germany.

Burke, J. E. and Turnbull, D.: 1952, Recrystallization and grain growth, *Progress In Metal Physics* **3**, 220–292.

Christiansen, G., Bowen, J. and Lindbo, J.: 2002, Electrolytic preparation of metallic thin foils with large electron-transparent regions, *Materials Characterization* **49**(4), 331–335.

Cotterill, P. and Mould, R. R.: 1976, *Recrystallization and Grain Growth in Metals*, 1 edn, Surrey University Press, London, UK.

Delannay, L., Mishin, O. V., Juul Jensen, D. and Houtte, P. V.: 2001, Quantitative analysis of grain subdivision in cold rolled aluminium, *Acta Materialia* **49**(13), 2441–2451.

Doherty, R. D. and Szpunar, J. A.: 1984, Kinetics of sub-grain coalescence - a reconsideration of the theory, *Acta Metallurgica* **32**(10), 1789–1798.

Faivre, P. J. and Doherty, R. D.: 1979, Nucleation of recrystallization in compressed aluminum - studies by electron-microscopy and kikuchi diffraction, *Journal Of Materials Science* **14**(4), 897–919.

Friedel, J.: 1964, *Dislocations*, Vol. 3 of *International series of monographs on solid state physics*, 1 edn, Pergamon Press Ltd., London, UK.

Fu, X., Poulsen, H., Schmidt, S., Nielsen, S., Lauridsen, E. and Juul Jensen, D.: 2003, Non-destructive mapping of grains in three dimensions, *Scripta Materialia* **49**(11), 1093–1096.

Furu, T., Ørsund, R. and Nes, E.: 1995, Subgrain growth in heacily deformed aluminium - experimental investigation and modelling treatment, *Acta Metallurgica Et Materialia* **43**(6), 2209–2232.

Gundlach, C., Pantleon, W., Lauridsen, E. M., Margulies, L., Doherty, R. D. and Poulsen, H. F.: 2004a, Direct observation of subgrain evolution during recovery of cold-rolled aluminium, *Scripta Materialia* **50**, 477–481.

Gundlach, C., Pantleon, W., Lauridsen, E. M., Margulies, L., Doherty, R. D. and Poulsen, H. F.: 2004b, In-situ observation of subgrain evolution during static recovery of cold-rolled aluminium, *Materials Science Forum* **467-470**, 1389–1394.

Gundlach, C., Schmidt, S., Margulies, L., Knudsen, T., Pantleon, W. and Poulsen, H. F.: 2005, Image analysis for X-ray studies of the dynamics of individual embedded subgrains during revovery, *Materials Science and Technology* **21**(12), 1476–1479.

Haasen, P.: 1996, *Physical Metallurgy*, 3 edn, Press Syndicate of the University of Cambridge, Cambridge, UK.

Hansen, N.: 1990, Cold deformation microstructures, *Materials Science and Technology* **6**(11), 1039–1047.

Hansen, N. and Huang, X.: 1998, Microstructure and flow stress of polycrystals and single crystals, *Acta Metallurgica* **46**(5), 1827–1836.

Hansen, N. and Juul Jensen, D.: 1999, Development of microstructure in fcc metals during cold work, *Philosophical Transactions Of The Royal Society Of London Series A-Mathematical Physical And Engineering Sciences* **357**(1756), 1447–1469.

Hillert, M.: 1965, On theory of normal and abnormal grain growth, *Acta Metallurgica* **13**(3), 227.

Hough, P. V. C.: 1962, A method and means for recognizing complez patterns, *U.S. Patent 3,069,654* .

Hu, H.: 1962, Direct Observations on the Annealing of a Si-Fe Crystal in the Electron Microscope, *Transactions of the Metallurgical Society of Aime* **224**(1), 75–84.

Hughes, D., Chrzan, D. C., Liu, Q. and Hansen, N.: 1997, Scaling of microstructural parameters: Misorientations of deformation induced boundaries, *Acta Materialia* **45**(1), 105–112.

Hull, D. and Bacon, D. J.: 1984, *Intruduction to DISLOCATIONS*, Vol. 37 of *International series on Materils Science and Technology*, 3 edn, Pergamon Press, Oxford, UK.

Humphreys, F. J.: 1997a, A unified theory of recovery, recrystallization and grain growth, based on the stability and growth of cellular microstructures-II. the effect of second-phase particles, *Acta Materialia* **45**(12), 5031–5039.

Humphreys, F. J.: 1997b, A unified theory of recovery, recrystallization and grain growth, based on the stability and growth of cellular microstructures-The Basic Model, *Acta Materialia* **45**(12), 4231–4240.

Humphreys, F. J.: 1999, A new analysis of recovery, recrystallisation and grain growth, *Materials Science and Technology* **15**(1), 37–44.

Humphreys, F. J. and Harherley, M.: 1995, *Recrystallization and related annealing phenoma*, 1 edn, Pergamon Press, New York, USA.

Jakobsen, B., Poulsen, H. F., Lienert, U., Almer, J., Shastri, S. D., Sørensen, H. O., Gundlach, C. and Pantleon, W.: 2006, Formation and subdivision of deformation structures during plastic deformation, *Science* . In press.

Jones, A. R., Ralph, B. and Hansen, N.: 1979, Subgrain Coalescence And The Nucleation Of Recrystallization At Grain-Boundaries In Aluminum, *Proceedings Of The Royal Society Of London Series A* **A368**, 345–357.

Kuhlmann, D. V., Masing, G. and Raffelsieper, J.: 1949, Zur Theorie der Erholung, *Zeitschrift Fur Metallkunde* **40**(7), 241–246.

Kuhlmann-Wilsdorf, D. and Hansen, N.: 1991, Geometrically Necessary, Incidental And Subgrain Boundaries, *Scripta Metallurgica et Materialia* **25**(7), 1557–1562.

Larsen, A., Gundlach, C., Poulsen, H., Margulies, L., Xing, Q. and Juul Jensen, D.: 2004, In-Situ Investigation of Bulk Nucleation by X-Ray Diffraction, *Materials Science Forum* **467-470**, 81–86.

Larsen, A. W.: 2004, *Quantitative studies of the nucleation of recrystallization in metals utilizing microscopy and X-ray diffraction*, PhD thesis, University of Copenhagen.

Larsen, A. W., Poulsen, H. F., Margulies, L., Gundlach, C., Xing, Q., Huang, X. and Juul Jensen, D.: 2005, Nucleation of recrystallization observed in situ in the bulk of a deformed metal, *Scripta Materialia* **53**, 553–557.

Lassen, N. C. K., Juul Jensen, D. and Conradsen, K.: 1992, Image procedures for analysis of electron back scattering patterns., *Scanning Microscopy* **6**(1), 115–121.

Lauridsen, E., Juul Jensen, D., Poulsen, H. and Lienert, U.: 2000, Kinetics of individual grains during recrystallization, *Scripta Materialia* **43**(6), 561–566.

Lauridsen, E. M.: 2001, *The 3D X-Ray Diffraction Microscope and its Application to the Study of Recrystallization Kinetics*, PhD thesis, University of Copenhagen.

Lauridsen, E. M., Schmidt, S., Suter, R. M. and Poulsen, H. F.: 2001, Tracking: a method for structural characterization of grains in powders or polycrystals, *Journal Of Applied Crystallography* **34**, 744–750.

Lauridsen, E., Poulsen, H., Nielsen, S. and Juul Jensen, D.: 2003, Recrystallization kinetics of individual bulk grains in 90aluminium, *Acta Materialia* **51**(15), 4423–4435.

Li, J. C. M.: 1962, possibility of subgrain rotation during recrystallization, *journal of applied physics* **33**(10), 2958–2965.

Lienert, U., Schulze, C., Honkimäki, V., Tschentscher, T., Garbe, S., Hignette, O., Horsewell, A., Lingham, M., Poulsen, H., Thomsen, N. and Ziegler, E.: 1998, Focusing optics for high-energy x-ray diffraction, *Journal Of Synchrotron Radiation* **5**(3), 226–231.

Liu, Q. and Hansen, N.: 1995, Geometrically necessary boundaries and incidental dislocation boundaries formed during cold deformation, *Scripta Metallurgical et Materialia* **32**(8), 1289–1295.

Liu, Q., Huang, X., Lloyd, D. J. and Hansen, N.: 2002, Microstructure and strength of commercial purity aluminium (AA 1200) cold-rolled to large strains, *Acta Materialia* **50**(15), 3789–3802.

Liu, Q., Juul Jensen, D. and Hansen, N.: 1998, Effect of grain orientation on deformation structure in cold-rolled polyscrystalline aluminium, *Acta Materialia* **46**(16), 5819–5838.

Margulies, L., Winther, G. and Poulsen, H.: 2001, In situ measurement of grain rotation during deformation of polycrystals, *Science* **291**(5512), 2392–2394.

Mishin, O. V., Bay, B. and Juul Jensen, D.: 2000, Through-thickness texture gradients in cold-rolled aluminum , *Metallurgical And Materials Transactions A* **31**(6), 1653–1662.

Mishin, O. V. and Juul Jensen, D.: 1999, The effect of rolling draughts on texture and microstruture in aluminium, *in* J. A. Szpunar (ed.), *ICOTOM-12*, NRC Research Press, pp. 1154–1159.

Nes, E.: 1995, Recovery revisited, *Acta Metallurgica et Materialia* **43**(6), 2189–2207.

Nes, E. and Sæter, J. A.: 1995, Recovery, modelling and experiments, *in* N. Hansen, D. Juul Jensen, Y. L. Liu and B. Ralph (eds), *16th Risø International Symposium on Materials Science*.

Nielsen, S. F.: 2000, *Synchrotron X-Ray Radiation and Deformation Studies*, PhD thesis, University of Copenhagen.

Nielsen, S. F., Wolf, A., Poulsen, H. F., Ohler, M., Lienert, U. and Owen, R. A.: 2000, A conical slit for three-dimensional XRD mapping, *Journal Of Synchrotron Radiation* **7**, 103–109.

Offerman, S., Dijk, N. V., Sietsma, J., Grigull, S., Lauridsen, E., Margulies, L., Poulsen, H., Rekveldt, M. and van der Zwaag, S.: 2002, Grain nucleation and growth during phase transformations, *Science* **298**(5595), 1003–1005.

Poulsen, H. F.: 2004, *Three-Dimensional X-Ray Diffraction Microscopy Mapping Polycrystals and their Dynamics*, Springer Tracts In Modern Physics 205, 1 edn, Springer-Verlag, Berlin, Germany.

Poulsen, H., Garbe, S., Lorentzen, T., Juul Jensen, D., Poulsen, F., Andersen, N., Frello, T., Feidenhansl, R. and Graafsma, H.: 1997, Applications of high-energy synchrotron radiation for structural studies of polycrystalline materials., *Journal Of Synchrotron Radiation* **4**, 147–154.

Poulsen, H., Nielsen, S., Lauridsen, E., Schmidt, S., Suter, R., Lienert, U., Margulies, L., Lorentzen, T. and Juul Jensen, D.: 2001, Three-dimensional maps of grain boundaries and stress state of individual grains in polycrystals and powders, *Journal Of Applied Crystallography* **34**(6), 751–756.

Read, W. T. and Shockley, W.: 1950, Dislocation Models of Crystal Grain Boundaries, *Phsyical Review* **78**(3), 275–289.

Reed-Hill, R. E.: 1964, *Physical Metallurgy Principles*, University series in basic engineering, 1 edn, D. Van Nostrand Company, INC., New York, USA.

Roerdink, J. M. and Meijster, A.: 2000, The Watershed Transform: Definitions, Algorithms and Parallelization Strategies, *FUNDINF: Fundamenta Informatica* **41**, 187–228.

Sabin, T. J., Winther, G. and Juul Jensen, D.: 2003, Orientation relationships between recrystallization nuclei at triple junctions and deformed structures, *Acta Materialia* **51**(4), 3999–4011.

Schmidt, S., Nielsen, S. F., Gundlach, C., Margulies, L., Huang, X. and Juul Jensen, D.: 2004, Watching the Growth of Bulk Grains During Recrystallization of Deformed Metals, *Science* **305**, 229–232.

Schulze, C., Lienert, U., Hanfland, M., Lorenzen, M. and Zontone, F.: 1998, Microfocusing of hard x-rays with cylindrically bent crystal monochromators, *Journal Of Synchrotron Radiation* **5**(2), 77–81.

Sörby, H. C.: 1886, *J. Iron Steel Inst.* p. 140.

Tabor, D.: 2000, *The hardness of metals*, Oxford University Press.

Vandermeer, R. A.: 1959, Edge-nucleated, growth controlled recrystallization in aluminum, *Transactions Of The American Institute Of Mining And Metallurgical Engineers* **215**(4), 577–588.

Warren, B. E.: 1990, *X-ray diffraction*, Springer Tracts in Modern Physics, 1 edn, Dover Publications, Inc., New York, USA.

Xing, Q., Huang, X. and Hansen, N.: 2004, Microstructural coarsening during annealing of cold rolled Aluminum, *Materials Science Forum* **467-470**(1-2), 209–214.

Available online at www.sciencedirect.com
SCIENCE DIRECT®
Scripta Materialia 50 (2004) 477–481
Scripta MATERIALIA
www.actamat-journals.com

Direct observation of subgrain evolution during recovery of cold-rolled aluminium

C. Gundlach [a], W. Pantleon [a], E.M. Lauridsen [a], L. Margulies [a,b], R.D. Doherty [c], H.F. Poulsen [a,*]

[a] *Centre for Fundamental Research: Metal Structures in Four Dimensions, Frederiksborgvej 399, Risø National Laboratory, Roskilde 4000, Denmark*
[b] *European Synchrotron Radiation Facility, BP 220, Grenoble 38043, France*
[c] *Department of Materials Science and Engineering, Drexel University, Room Lebow 332C, Philadelphia, PA 19104, USA*

Received 15 October 2003; accepted 28 October 2003

Abstract

An X-ray diffraction method is introduced for monitoring the change in volume and orientation of individual, embedded subgrains during static recovery. It is limited to plate-like specimens with a thickness of less than 100 subgrain sizes. Growth curves are presented for nine subgrains within a 38% cold-rolled aluminium specimen during annealing for 3 h at 300 °C.

Keywords: Recovery; X-ray diffraction; Synchrotron radiation; 3DXRD; Aluminium

1. Introduction

During plastic deformation of metals metastable dislocation structures form with dislocation boundaries separating nearly dislocation free regions. The latter are termed either dislocation cells or subgrains depending on their morphology and mutual orientation difference. Here, they will always be referred to as subgrains. The processes occurring during subsequent annealing, such as the coarsening of the microstructure, are commonly summarised as (static) recovery.

Conventionally, recovery is studied in several ways [1]. Bulk probes are used, typically calorimetry, electrical resistivity and hardness measurements. The results represent an average over all processes and over the heterogeneity of the specimen. Within the last two decades deformation-induced microstructures have been characterised in detail by TEM and EBSD, both prior to annealing [2–4] and after annealing [1,5,6]. Such studies have provided much insight into structural arrangements. However, the dynamics of the individual elements of the microstructure cannot be observed directly in an unambiguous way with these techniques. (*In-situ* electron microscopy observations have been reported by a number of groups. However, the foil thickness is typically only 100 nm; much less than the mean subgrain size typically of about 1 μm. Thus these experiments are two-dimensional while subgrain growth processes are essentially three-dimensional.)

In this paper a method is presented that enables studies of the individual *embedded* subgrains during recovery. The method is an extension of the recently developed 3-Dimensional X-Ray Diffraction (3DXRD) method, which has been used for structural characterisation of grains within millimetre-to-centimetre thick polycrystals. The basic concepts behind 3DXRD are the use of a focused monochromatic beam of high energy X-rays from a synchrotron source and a "tomographic" approach to diffraction [7–9]. 3DXRD enables the characterisation of the position, volume, crystallographic orientation, strain state and grain boundary morphology of several hundred grains simultaneously. As such it has been applied to nucleation-and-growth studies of the emerging nuclei during static recrystallisation [10,11] and phase transformations [12].

Notably, the smallest elements in the recovered microstructure, the subgrains, can be considered as coherently diffracting domains with a negligible intrinsic orientation spread. Hence, in principle by replacing grains with subgrains the 3DXRD formalism can be applied directly. However, the dimensions of the

* Corresponding author. Tel.: +45-4677-5739; fax: +45-4677-5758.
E-mail address: henning.friis.poulsen@risoe.dk (H.F. Poulsen).

1359-6462/$ - see front matter © 2003 Acta Materialia Inc. Published by Elsevier Ltd. All rights reserved.
doi:10.1016/j.scriptamat.2003.10.034

subgrains make such studies technically challenging. As the spatial resolution of 3DXRD currently is 5 μm [13], subgrains can only be identified by orientation contrast. Likewise, 3DXRD is presently limited to the case of non-overlapping diffraction spots. Under favourable conditions (perfect crystallites with random orientations) this limits the investigation to a few thousand crystallites. Hence, the shear number of subgrains within a millimetre thick specimen is prohibitive. The spot overlap problem can be countered by studies of plate-like specimens with reduced thickness. If there are 10–100 subgrains across the thickness of the plate, the dynamics of the central ones will be a reasonable representation of bulk behaviour.

An in situ recovery experiment has been performed on a disc of 38% cold-rolled aluminium. Growth curves are derived for nine cells during annealing at 300 °C. The study partly proves the feasibility, partly provides first results on the microstructural dynamics.

2. Experimental

The experiment was performed at the 3DXRD microscope located at Materials Science Beamline ID11 at the European Synchrotron Radiation Facility. The set-up is sketched in Fig. 1. The X-ray beam from the synchrotron was monochromatised and focused by a combination of a bent Laue crystal and a bent and graded multi-layer [14]. The resulting 50 keV beam was defined by a set of slits to a Gaussian shaped spot with a full width half maximum of 7 μm.

The sample material was commercial purity aluminium AA1050 (99.5%), cold-rolled to 38% reduction in one pass with an intermediate draught (from series A1 of previous studies [15,16]). A thin disc was prepared from the sheet material by mechanical grinding and punching out a 3 mm disc. By means of electro-polishing analogous to the preparation technique for foils suitable for TEM investigations [17] a relatively large, thinner area of nearly uniform thickness was obtained.

The disc was mounted in a massive copper holder together with a copper ring upon which L-shaped gold markers had been deposited. The internal corner of these markers served as reference positions to ensure that the same area of the disc was illuminated during the experiment. The sample holder was placed in an evacuated X-ray transparent furnace. The furnace was mounted on top of an (x, y, z)-translation stage and an ω-rotation stage (see Fig 1). The disc was positioned in the focal spot of the beam, which was centred with respect to the ω-rotation axis.

Images of the diffraction spots were recorded with a two-dimensional area detector, a FRELON CCD coupled to an image intensifier. This 14 bit detector has 1024×1024 pixels, each with a pixel size of 150×150 μm^2.

3. Measuring procedure and data analysis

The aim of the experiment is to determine the orientation and volume of a set of subgrains as function of annealing time. This can be accomplished by repeatedly determining the centre-of-mass (CMS) position on the detector and the integrated intensity of a set of diffraction spots. In previous work on recrystallisation a measuring scheme was presented for sampling integrated intensities and for validating that grains were illuminated fully and uniformly [10,11]. This scheme can in principle be used also for recovery. However, with the available optics, the assumption of a uniform intensity profile cannot be fulfilled for the small beam size of relevance for the present study.

Therefore, the measuring scheme was modified as follows: exposures were made at five ω-positions, namely $-2°$, $-1°$, $0°$, $1°$ and $2°$. During each exposure the specimen was oscillated by $\pm 0.5°$. This ω-scanning was repeated at nine positions of a 3×3 (y, z)-grid, with a distance between the nodes in the grid of 5 μm.

For each non-overlapping diffraction spot and each ω-position, the integrated intensity of the spot at the nine

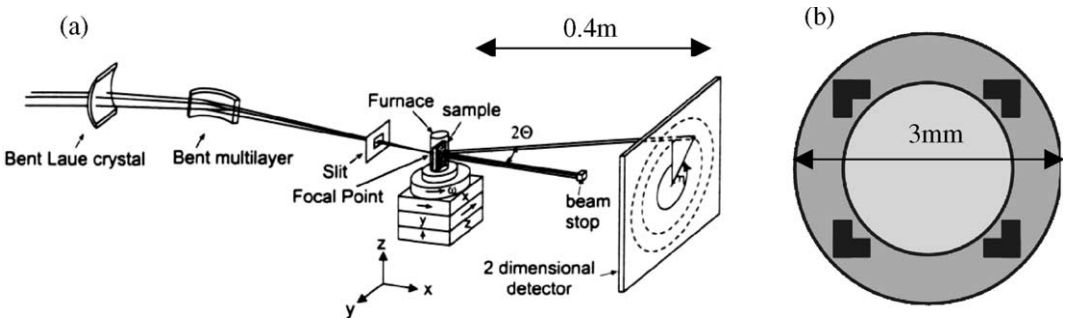

Fig. 1. (a) Sketch of the experimental set-up. The (x, y, z) co-ordinate system and the angles ω, η and 2θ are defined. (b) Sample geometry. The disc is placed in a copper holder together with a copper ring, upon which L-shaped gold fluorescence markers are deposited.

grid points was determined. A least-square fit was performed to these data, assuming a Gaussian beam profile. The parameters fitted were the CMS position of the associated subgrain and a position-independent integrated intensity. Subgrains positioned at a distance of 5 μm or more from the centre of the grid were considered non-valid, as the analysis in such cases is not sufficiently robust. Furthermore, a few reflections were found which spanned two neighbouring ω-bins—an indication of a small orientation spread within the corresponding subgrain. In order to sample the complete volume, the integrated intensities from the two images were added.

The integrated intensity of the diffraction spot is proportional to the volume of the associated coherently diffracting domain—the subgrain (kinematical scattering). The proportionality constant was found by calibration to a powder specimen of known geometry, as described in [10]. From this calibration it was also inferred that the detection limit on the diffraction spots corresponds to a subgrain radius of 150 nm. Furthermore, by scaling the total intensity in specific hkl rings, the thickness of the disc at the illuminated position was determined to be (80 ± 20) μm. Since the mean subgrain size was determined to remain below 2 μm, most of the diffraction spots should be associated with bulk subgrains.

The experiment was initiated by first selecting and characterising a region of the sample with a high density of resolvable diffraction spots and locating the position of this selected region with respect to the gold markers. The sample was then heated from room temperature to 300 °C in 3 min. During the following 181 min the temperature was kept constant while continuously repeating the (y, z, ω) grid measurements every 5 min. Between each of the 5-min-sets of observation the sample position was rechecked against the markers.

4. Results and discussion

Typical examples of background-subtracted images are given in Fig. 2. Approximately 100 distinct diffraction spots are observed in each image. Typically, the spots are point-like and appearing in "clusters" on the screen. Each spot is interpreted as arising from an individual subgrain. A cluster is interpreted as a set of subgrains of similar orientations. These are likely to be neighbours, e.g. appearing within the same cellblock.

Initially we present a statistical analysis. Histograms of the apparent subgrain sizes as derived from 500 diffraction spots are shown in Fig. 3 for the as-deformed state and after 3 and 181 min of annealing at 300 °C. Essentially all non-overlapping spots in the images are

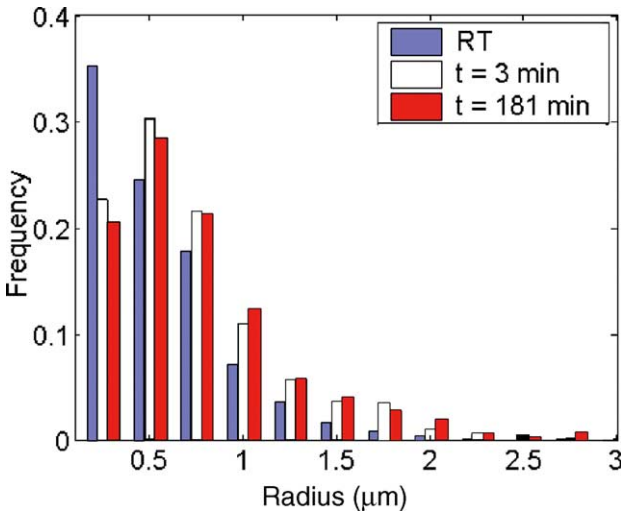

Fig. 3. Histograms of the apparent subgrain size (equivalent sphere radii) obtained from 500 individual diffraction spots of the same region in the as-deformed state (light grey, left) and after 3 min (white, middle) and 181 min (dark grey, right) of in situ annealing at 300 °C.

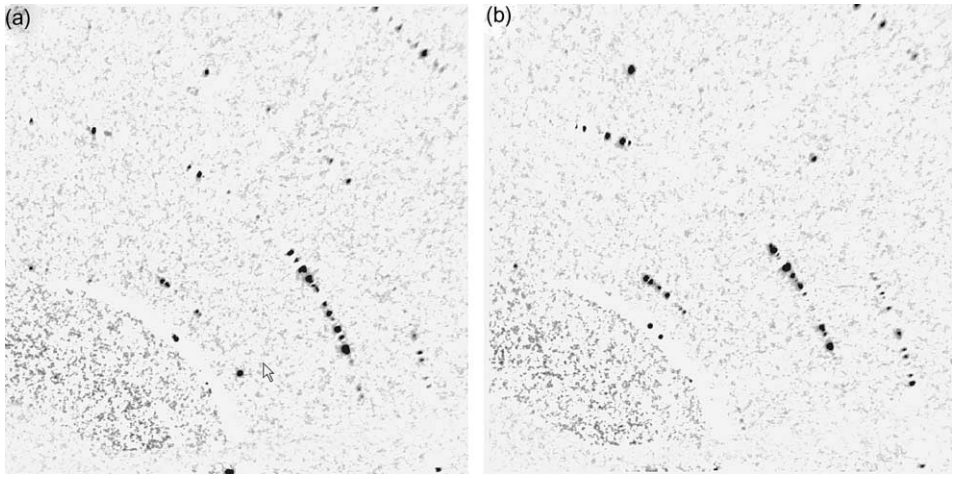

Fig. 2. Background subtracted images representing the same region (and the same ω-range) on the aluminium specimen (a) after 3 min and (b) after 181 min of annealing at 300 °C. Only a quadrant of the full diffraction pattern is shown. Black corresponds to an intensity level of 500 cts/pixel while the maximum intensities in the diffraction spots are 16384 cts/pixel.

included in this analysis, irrespective of whether they are valid and whether it is the same spots that appears at the three stages or not. Note, that the apparent subgrain volume is the result of a convolution of the true subgrain volume with the Gaussian beam profile. From simulations based on a log-normal distribution of the true subgrain radii, an average true subgrain radius of 1.2 μm is obtained by fitting the room temperature data. This is in agreement with estimations from TEM investigations on the same material (cf. Fig. 2a in [16]) and corroborates the interpretation of the diffraction spots as arising predominantly from individual subgrains. After annealing for 3 min the average true subgrain size increased to 1.6 μm and even further to 1.7 μm after 181 min. Evidently, substantial coarsening has occurred during the 3 min of heating up and the duration of the first grid measurement at 300 °C, while the amount of coarsening taking place during the following 3 h is small.

In the following we present results for the dynamics of nine individual subgrains, which fulfil the validation criteria described above.

The evolution in the (true) size is shown in Fig. 4. Among the subgrains, more than half exhibit essentially no growth (# 1,3,4,7,9), two shrink during the first hour and then stay constant (# 6,8), one grows rapidly during the first 5 min then stagnates (#2), while the last one first grows, then shrinks (# 5). In general, the curves exhibit a smooth evolution. Strikingly, there is no obvious correlation between subgrain volume and growth behaviour. The smallest subgrain #2 grows substantially during the first 5 min. So does the rather large subgrain #5. On the other hand, one of the larger subgrains shrinks during the observation and the largest one does not change in size at all. This behaviour is in marked contrast with elementary theories of curvature (i.e. interfacial energy) driven coarsening, e.g. [1,18], where subgrains larger than average are expected to grow while subgrains smaller then average are expected to shrink. However, this behaviour might be strongly affected by the local neighbourhood of the individual subgrains. From the small number of observed subgrains it cannot be excluded, that a curvature driven model is valid in a statistical sense. Analysis of a larger number of subgrains is required for resolving this issue.

An alternative coarsening mechanism has been suggested [19], where two neighbouring subgrains rotate until they approach the same orientation and coalesce. From TEM investigations evidence has been gained for this mechanism [5,18,20]. It is reported to occur only in specific (and statistically rather rare) sites, notably at grain boundaries and at the intersection of grain boundaries and in grain transition bands [5,20]. In order to determine whether any of the nine validated subgrains rotated during the annealing the CMS position of the diffraction spots on the detector and the ω-bin position were monitored. For eight of the reflections no rotation was detected within the experimental accuracy, estimated to be 0.3°. For subgrain #6 the CMS position of the diffraction spot on the detector changed by 1° along η during annealing. However, this particular diffraction spot initially exhibits an orientation spread of $\Delta\eta = 1.2°$ and may consist of contributions from different subgrains. This is further supported by a closer inspection showing that the change in η is caused mainly by vanishing of part of the diffraction spot corresponding to the disappearance of a subgrain of a slightly different orientation.

5. Outlook

The feasibility study presented here has some shortcomings, which however can be circumvented by extending the analysis. Extrapolating from the progress in 3DXRD studies of recrystallisation, where growth curves were determined first for 6 grains [10], then for 240 grains [11], it is foreseeable that analysis of a larger ensemble of subgrains will be possible in the future. At the same time, extending the data acquisition to a larger

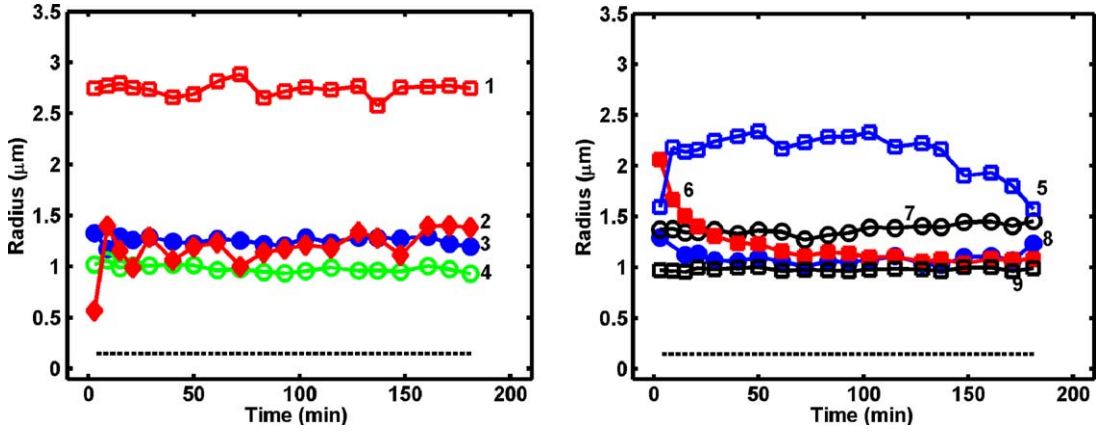

Fig. 4. The evolution in size of nine individual subgrains. The equivalent sphere radius is shown as a function of annealing time. The detection threshold of 150 nm is marked as a dashed line. Numbers are used to identify the subgrains.

ω-range will enable an analysis based on multi-crystal indexing program GRAINDEX [7] and provide the full orientation of each subgrain and its elastic strain tensor [8]. Furthermore, by triangulation the position of a subgrain in the specimen can be determined with respect to the thickness of the disc based on the analysis of two or more diffraction spots. If the reflections used span 90° in ω, the accuracy will match the 1–2 μm found from the (y,z) fit above. Notably, this extended analysis requires a longer total acquisition time and can be performed only at the beginning of the experiment, before heating, and/or at the end of the annealing process.

With these upgrades, a fairly universal method is devised, which for the first time makes it possible to base coarsening models directly on observations of the microstructural dynamics.

6. Conclusions

(i) A unique diffraction technique has been established, enabling *in-situ* studies of the dynamics of the individual subgrains during recovery.
(ii) Statistics on subgrain size distributions imply that most of the subgrain coarsening occurs during heating up and the first 3 min of annealing.
(iii) The growth curves for the individual subgrains are different from the average behaviour for a subgrain of a given size as predicted by deterministic models based on interfacial energy driven mechanisms.
(iv) Within the accuracy of the method no rotation of the nine observed subgrains could be detected during annealing.

Acknowledgements

The authors gratefully acknowledge the Danish National Research Foundation for supporting the Centre for Fundamental Research: Metal Structures in Four Dimensions, within which this work was performed. Additional support for this work was provided by the Danish research council SNF (via Dansync). The authors thank the staff of ID11, ESRF for help with the synchrotron experiment, O.V. Mishin and D. Juul Jensen for supplying the cold-rolled material, P. Nielsen and G. Christiansen for technical support and N. Hansen, E. Johnson, J. Teuber and J.R. Bowen for valuable discussions.

References

[1] Humphreys FJ, Hatherley M. Recrystallization and related annealing phenomena. New York: Pergamon Press; 1995.
[2] Hansen N, Juul Jensen D. Philos Trans R Soc London 1999;A357:1447.
[3] Hansen N. Metall Mater Trans 2001;A32:2917.
[4] Hurley PJ, Humphreys FJ. Acta Mater 2003;51:1087.
[5] Faivre P, Doherty RD. J Mater Sci 1979;14:897.
[6] Godfrey A, Juul Jensen D, Hansen N. Acta Mater 2001;49:2429.
[7] Lauridsen EM, Schmidt S, Suter RM, Poulsen HF. J Appl Cryst 2001;34:744.
[8] Poulsen HF, Nielsen SF, Lauridsen EM, Schmidt S, Suter RM, Lienert U. J Appl Cryst 2001;34:751.
[9] Poulsen HF. Philos Mag 2003;83:2761.
[10] Lauridsen EM, Juul Jensen D, Poulsen HF, Lienert U. Scripta Mater 2000;43:561.
[11] Lauridsen EM, Poulsen HF, Nielsen SF, Juul Jensen D. Acta Mater 2003;51:4423.
[12] Offerman SE, van Dijk NH, Sietsma J, Grigull S, Lauridsen EM, Margulies L. Science 2002;298:1003.
[13] Poulsen HF, Fu X. J Appl Cryst 2003;36:1062.
[14] Lienert U, Schulze C, Honkimäki V, Tschentscher T, Garbe S, Hignette O. J Synchrotron Radiat 1998;5:226.
[15] Mishin OV, Bay B, Juul Jensen D. Metall Mater Trans 2000;A31:1653.
[16] Mishin OV, Juul Jensen D, Bay B. In: J.A. Szpunar, editor. Proceedings of ICOTOM-12. NRC Research Press; 1999. p. 1154.
[17] Christiansen G, Bowen JR, Lindbo J. Mater Charact 2003;49:331.
[18] Jones AR, Ralph B, Hansen N. Proc R Soc 1979;A368:345.
[19] Hu H. Trans Metall Soc AIME 1962;224:75.
[20] Doherty RD, Szpunar JA. Acta Metall 1984;32:1789.

Materials Science Forum Vols. 467-470 (2004) pp. 1389-1394
online at http://www.scientific.net

In-situ Observation of Subgrain Evolution during Static Recovery of Cold-rolled Aluminium.

C. Gundlach[1], W. Pantleon[1], E.M. Lauridsen[1], L. Margulies[1,2], R.D. Doherty[3] and H.F. Poulsen[1]

[1] Center for Fundamental Research: Metal Structures in Four Dimensions,
Materials Research Department, Risoe National Laboratory, DK-4000 Roskilde, Denmark

[2] European Synchrotron Radiation Facility, BP 220, F-38043 Grenoble, France

[3] Dept. for Materials Science and Engineering, Drexel University, Philadelphia PA 19104, US

Keywords: Recovery; X-ray Diffraction; Synchrotron Radiation; 3DXRD; Aluminium

Abstract. A method for *in-situ* studies of the dynamics of individual embedded subgrains during recovery is introduced. The method is an extension of 3DXRD principles for studies of grain dynamics in connection with recrystallisation. It is limited to studies of foils with a sample thickness of 10-100 subgrains due to diffraction spot overlap. The volume evolution during recovery (annealing at 300°C for 181 minutes) of nine individual subgrains in a deformed sample (38% cold rolled Aluminium) is presented.

Introduction

Classically the processes taking place during (static) recovery have been studied in two ways [1]: For the first category of methods, results are obtained as averages over all processes and the heterogeneity of the sample. Examples are calorimetry and measurements of hardness and electrical resistivity. For such measurements typically bulk samples are used. The other category comprises local studies by electron microscopy. With TEM and EBSP deformation microstructures have been characterized in great detail [2-4]. A good description of the microstructure before and after annealing is obtained [1,5,6], but information about the dynamics of the individual bulk subgrains during annealing is missing. Notably, *in-situ* recovery studies with TEM have been reported, but specimens used were ~100 nm thick, which is smaller than the typical subgrain size. Hence, the dynamics is not considered representative of bulk behaviour.

A relatively new method to study annealing processes *in-situ* is 3-Dimensional X-ray Diffraction (3DXRD) microscopy [7,8]. Based on the use of diffraction with high energy x-rays generated from synchrotron sources, 3DXRD has proven to be a powerful tool for studies of grain dynamics within millimeter to centimeter thick polycrystals. In favourable conditions 3DXRD can be used to study the volume, crystallographic orientations, positions, strain state and grain boundary morphology of hundreds of grains simultaneously.

The objective of the work reported here is to extend 3DXRD microscopy to work on the subgrain scale. Subgrains are nearly dislocation free regions. Hence, they can be considered to be coherently diffracting domains, generating independent diffraction spots. Provided these spots are distinct (non-overlapping) the 3DXRD formalism applies. However, the spot overlap issue is much more pronounced in this case, as the deformation induced subgrains are smaller than the recrystallised grains of interest in previous studies (*e.g.* [9]).

The solution suggested in [10] is to reduce the size of the gauge volume by focusing the beam and using thin samples. Under the best conditions for the 3DXRD method (the diffraction spots distributed evenly on the Debye-Scherrer rings, grains or subgrains with random orientations) a few

thousand structural elements can be characterised simultaneously. In the case of subgrains of size about 1 μm this implies focusing the beam to a spot with dimensions of a few microns and the use of foils with a thickness corresponding to 10-100 subgrains. With this geometry the subgrains in the middle of the foil can be considered bulk subgrains. Hence the dynamic of these subgrains will be a reasonable representation of the bulk behavior.

Results [10] from an *in-situ* recovery experiment on a disc of 38% cold rolled Aluminium using the described method will be presented.

Experimental

The 3DXRD microscope, on which the experiment was performed, is located at the Materials Science Beamline ID11, ESRF. The x-ray beam was monochromatised with an energy of 50 keV using a bent Laue Si(111) crystal. In combination with a bent and graded multilayer the bent Laue crystal [11] focused the beam to a size of 7 μm x 7 μm, as defined by the full width half maximum (FWHM). The tails of the beam were in part removed by slits, resulting in a Gaussian shaped intensity distribution.

Diffraction spots from the individual subgrains were recorded on a two-dimensional position sensitive detector: a 14 bit FRELON CCD coupled to an Image Intensifier. The active area of the detector was 1536 mm x 1536 mm, which when distributed on 1024 x1024 pixels corresponds to a pixel size of 150 μm x 150 μm. The detector was placed 0.4 m from the sample. A schematic view of the setup is provided in Fig 1 a).

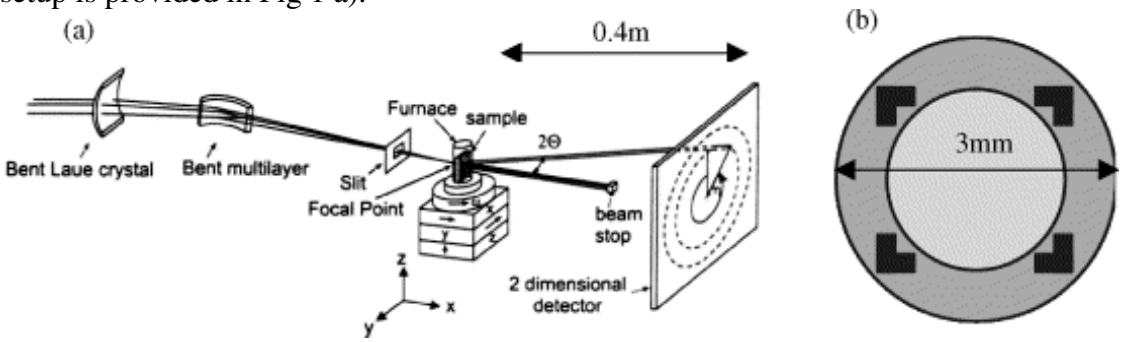

Figure 1: a) The setup of the experiment, defining the translations (x,y,z) and angles (ω, η, 2θ). The sample is positioned at the focal point. b) Schematic view of the 3 mm aluminium disc (dark grey) with gold markers (black) attached to the sample (light grey). The inner diameter of the disc is 1 mm.

Sample

The materiel studied was commercial purity aluminium AA1050 (99.5%) cold rolled to 38% thickness reduction in one pass. This materiel has been the subject of other studies [12,13]. Samples in the form of small discs with a diameter of 3 mm were made from this material. The discs were prepared as samples for TEM studies, and electro-polished to produce an area of almost uniform thickness. The sample disc was put inside a copper sample holder together with an aluminium ring upon which L-shaped gold markers have been sputtered, see Fig 1b). The legs of the gold markers have a length of 400 μm and a width of 100 μm. The gold markers were used as reference points. The sample holder was placed in a furnace, which was operated in an Argon atmosphere. The furnace was mounted on a goniometer comprising an (x,y,z) translation stage and an ω rotation

stage. The foil was aligned perpendicular to the beam for $\omega = 0°$. Furthermore, the illuminated part of the foil was aligned with respect to the center of rotation.

Measurements

The measurement scheme was as follows: exposures were made at 5 different ω settings: -2°, -1°, 0°, 1° and 2°. At each exposure the sample was oscillated ± 0.5°. Such a set of exposures was made for a total of 9 sample positions, corresponding to translations of the sample along y and z in a 3x3 grid. This (y,z)-grid was made in steps of 5 μm, to be compared with the beam dimension of 7 μm x 7 μm. By inspection a region of the sample was selected with not too many overlapping diffraction spots. The location of this region was determined with respect to the position of the two legs of one of the gold markers, as measured with a fluorescence detector. The sample was heated to 300°C in 3 minutes and kept at temperature for 3 hours. The grid measurements were performed continuously during this period. Every 10 minutes the position of the gold marker was rechecked. In this way it was ensured that the same volume was illuminated throughout.

Data analysis

A non-overlapping spot on the detector will be located on the same pixel independent of position within the (y,z)-translation grid. For a diffraction spot identified at all grid positions the integrated intensity was determined at each position. Based on these nine intensities a least square fit of a Gaussian function was performed in order to determine the position of the subgrain within the grid. Only subgrains positioned within 5 μm from the center of the grid were considered valid, as the fit is only robust in these cases. A few diffractions spots were found to be in two adjacent ω-bins; in these cases the integrated intensities were added.

In the kinematical scattering approximation – which is fulfilled in the present case – the integrated intensity of a diffraction spot is proportional to the associated coherently scattering domain volume; that is to the volume of the associated subgrain. Similar to the case of analyzing grain growth [9], the proportionality constant was found by calibration with a sample of known thickness and random orientations of grains.

Results

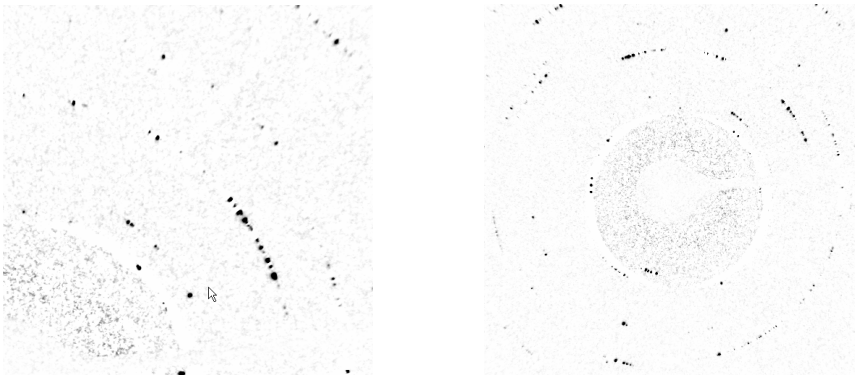

Figure 2: Background subtracted images representing the same region (and the same ω-range) of the aluminium specimen (a) after 3 minutes and (b) after 181 minutes of annealing at 300 °C: (a) a zoom to see the different diffraction spots. (b) the entire image recorded by the CCD-camera.

By summing the intensities in the Debye-Scherrer rings and comparing the result with the outcome of a similar analysis of the data originating from the calibration sample the thickness of the illuminated sample was estimated to be 80 μm ± 20 μm. Hence, the majority of the diffracting subgrains are fully embedded structural elements.

Fig. 2 shows characteristic examples of background-subtracted images. It is seen that the diffraction spots are clustered but still appear as distinct spots. Each spot is assumed to originate from diffraction on one subgrain. There are around 100 diffraction spots in each image. Unfortunately, with the geometry chosen, most diffraction spots are not valid, as the maximum intensity subgrain positions determined are more than 5 μm apart from the center of the grid. Following the described data analysis nine spots were found to fulfill the validation criteria. The growth dynamics of these nine individual subgrains are presented below.

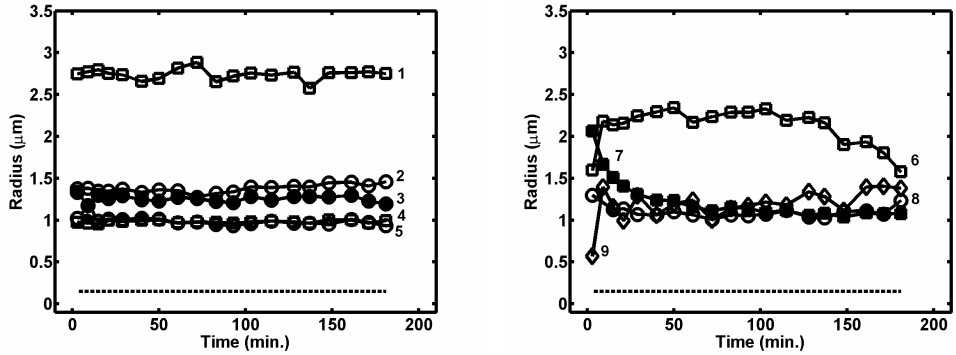

Figure 3: Equivalent spherical radius of the nine individual subgrains during 181 minutes of annealing. The dashed line shows the detection limit of 150 nm. a) five of the subgrains stay with constant size during the annealing. b) four subgrains change size during the annealing time.

The evolution of the sizes of the individual subgrains is shown in Fig. 3. Five subgrains (no. 1 – 5) exhibit essentially no growth as seen in fig. 3 a). Two subgrains (no. 7,8) shrink during the first hour and then stay constant in size, fig. 3 b). One grows (no. 9) quickly within the first 5 minutes, after which the volume is fixed. The last one (no. 6) starts by growing, then after 100 minutes it shrinks as seen in fig. 3 b).

The most interesting observation from these curves is that there is no correlation between the initial sizes of the subgrains and whether they grow or shrink. This observation is in contrast to the elementary theories of curvature driven coarsening [1]. According to these subgrains above the average subgrain size are expected to grow and the subgrains with smaller size the average subgrain size are expected to shrink. In the present set of data the smallest subgrain grows and the second largest subgrain shrinks. The largest subgrain found stays constant during the time of observation.

However, one should keep in mind the small amount of subgrains validated. Furthermore, no information about the size of neighboring subgrains is provided. Hence, it is not possible to exclude that a curvature-driven coarsening model is valid in a statistical sense.

The center-of-mass positions on the detector of the different diffraction spots were determined. Based on this an analysis of the potential rotation of the subgrains was performed. From TEM work it has been reported that in some cases two neighboring subgrains rotate to the same orientation to become one subgrain [5,14]. For 8 of the sub-grains, no rotation was found within the experimental

accuracy, which is about 0.3° in η and 0.2°-1° in ω. For diffraction spot no. 7, a rotation of 1° along η was detected during the first time step. However, this diffraction spot had an initial orientation spread of 1.2°. A closer investigation of the spot revealed that the rotation was the result of the disappearance of intensity at one end of the η–range. This behaviour can be explained in terms of the spot initially being a compound spot, and the disappearance of one of the component subgrains.

Conclusion

- A method to study evolution of individual bulk subgrains *in-situ* during recovery has been established.
- Growth curves for nine subgrains are reported. These growth curves differ from the average behavior predicted by curvature driven models.
- Within the experimental accuracy, no evidence was found for subgrain rotation.

Acknowledgments

The authors gratefully acknowledge the Danish National Research Foundation for supporting the Center for Fundamental Research: Metal Structures in Four Dimensions, within which this work was performed. Additional support for this work was provided by the Danish research council SNF (via Dansync). The authors thank the staff of ID11, ESRF for help with the synchrotron experiment, O.V. Mishin and D. Juul Jensen for supplying the cold-rolled material, P. Nielsen and G. Christiansen for technical support and N. Hansen, E. Johnson, J. Teuber and J.R. Bowen for valuable discussions.

References

[1] F. J. Humphreys, M. Hatherley: *Recrystallization and Related Annealing Phenomena.* (New York, Pergamon Press, 1995).

[2] N. Hansen, D. Juul Jensen: Phil Tr Royal Soc London Vol. 357 (1999), p. 1447

[3] N. Hansen: Metall. Mater Trans Vol. 32 (2001), p. 2917

[4] P. J. Hurley, F. J. Humphreys: Acta Mat Vol. 51 (2003), p. 1087

[5] P. Faivre, R. D. Doherty: J Mater Sci Vol. 14 (1979), p. 897

[6] A. Godfrey, D. Juul Jensen, N. Hansen: Acta Mat Vol. 49 (2001), p. 2429

[7] H. F. Poulsen, S. F. Nielsen, E.M. Lauridsen, S. Schmidt, R.M. Suter, U. Lienert, J Appl Cryst Vol. 34 (2001), p. 751

[8] H. P. Poulsen, D. Juul Jensen: Mater. Sci. Forum Vol 408-412 (2002), p 49

[9] E. M. Lauridsen, D. Juul Jensen, H. F. Poulsen, U. Lienert: Scripta mater. Vol. 43 (2000), p. 561

[10] C. Gundlach, W. Pantleon, E.M. Lauridsen, L. Margulies, R.D. Doherty, H.F. Poulsen, Scripta mater. Vol. 50 (2004), p. 477.

[11] U. Lienert, C. Schulze, V. Honkimäki, T. Tschentscher, S. Garbe, O. Hignette, J Synchrotron Rad Vol. 5 (1998), p. 226

[12] O. V. Mishin, B. Bay, D. Juul Jensen: Metall Mater Trans Vol. 31 (2000), p. 1653

[13] O. V. Mishin, D. Juul Jensen, B. Bay: In: J.A. Szpunar, editor: *Proceedings of ICOTOM-12.* (NRC Research Press, 1999, p. 1154)

[14] A. R. Jones, B. Ralph, N. Hansen: Proc Roy Soc Vol. 368 (1979), p. 345

Available online at www.sciencedirect.com
SCIENCE DIRECT®
Scripta Materialia 51 (2004) 783–788
Scripta MATERIALIA
www.actamat-journals.com

Characterising the dynamics of individual embedded dislocation structures

H.F. Poulsen *, J.R. Bowen, C. Gundlach

Department of Materials Research, Centre for Fundamental Research: Metal Structures in Four Dimensions, Risø National Laboratory, Frederiksborgvej 399, DK-4000 Roskilde, Denmark

Accepted 8 June 2004
Available online 10 July 2004

Abstract

The 3DXRD concept is extended to the characterisation of elements within the microstructure of deformed metals. Using orientation contrast, the dynamics of individual embedded cells are characterised as a function of annealing with a size-limitation of 100 nm. Applications for studies of recovery and nucleation are demonstrated and discussed.

Keywords: X-ray diffraction; Synchrotron radiation; 3DXRD; Recovery; Nucleation

1. Introduction

Traditionally structural characterisation of metals and alloys on the scale of grains and dislocation structures is performed by the application of surface-sensitive probes, such as electron microscopy (EM). The resulting characterisation in 2D prohibits studies of the real dynamics of the individual elements in the microstructure, which is 3D in nature. Hence, no direct information is provided on the local behaviour and therefore on the governing mechanisms. More generally, it is difficult to characterise the effect of heterogeneities in the structure.

In the view of the authors, it is vital to develop experimental methods that overcome these shortcomings, in order to be able to substitute state-of-the-art phenomenological models by models based on first-principles. Therefore Risø has collaborated with the European Synchrotron Radiation Facility (ESRF) in establishing a method for characterising the structure and dynamics of the *individual* embedded grains within thick specimens. The method, known as three-dimensional X-ray diffraction (3DXRD) microscopy, is based on the diffraction of X-rays in the energy range above 50 keV [1–4]. When generated by synchrotrons such hard X-rays exhibit a unique combination of a large penetration power (1 mm universally and up to 4 cm in light materials such as aluminium) and high flux. By focusing the beam and applying novel reconstruction software the position, volume, orientation and elastic strain can be determined in hundreds of grains simultaneously [1,2]. Furthermore, for coarse-grained materials a three-dimensional map of the grain boundaries can be generated [2,3]. With the dedicated 3DXRD microscope at ESRF, these methods have been employed to in-situ studies of the grain dynamics during recrystallization [5] and during phase transformations [6]. Moreover, a comprehensive study has been made of the response of the embedded grains during plastic deformation [7,8]. A main limitation for these studies has been the spatial resolution, which is a function of the available hardware, and presently is 5 μm [3].

* Corresponding author. Tel.: +45 4677 5739; fax: +45 4677 5758.
E-mail address: henning.friis.poulsen@risoe.dk (H.F. Poulsen).

1359-6462/$ - see front matter
doi:10.1016/j.scriptamat.2004.06.024

In this paper it is discussed how 3DXRD can be extended to studies in the 0.1–5 μm scale. The focus is on in-situ annealing studies of the dynamics of embedded dislocation structures in cell-forming metals; that is on the processes of static recovery and nucleation. However, the methodology has applications within a broad range of fields, e.g. phase transformations in steels, domain evolution in ferro-electrics and studies of sintering in ceramic compounds.

In the case of cell-forming metals, the microstructure is arranged hierarchically in such a way that the smallest elements—the dislocation cells—can be considered as near-perfect crystallites. Hence, in principle by replacing grains with cells the 3DXRD formalism can be applied directly. However, it is not possible to map the cells, as the size typically is 0.2–2 μm, which is smaller than the spatial resolution. To circumvent this problem two approaches are suggested: a general-purpose one based on the use of thick foils, and one mainly of relevance for bulk nucleation studies. In both cases, the cells are identified by orientation contrast. The limitation on size is then determined by counting statistics only.

Recently, the first results on static recovery in cold-rolled aluminium by the two approaches have appeared in separate publications [9,10]. In this article we compare the two and discuss their potential further development. In addition the feasiblity of coarsening studies of a material deformed to a very high strain ($\varepsilon_{vm} = 10$) is demonstrated.

2. DXRD: basic concepts

The 3DXRD methodology is described in detail in [1–4]. The underlying geometry of relevance to this article is shown in Fig. 1. The sample is mounted on an $x-y-z-\omega$ stage, where ω is a rotation around an axis perpendicular to the incoming beam. A monochromatic beam is focused in two directions, probing the specimen within a rod-shaped volume. The cross-section of the beam is substantially larger than the size of the smallest microstructural element. The part of the structure, which fulfils the Bragg condition, will generate a diffracted beam. This is transmitted through the sample and detected as diffraction spots on a wide-area 2D detector, positioned at a distance from the specimen. To probe the complete structure, and not just the part that happens to fulfil the Bragg condition, the sample must be rotated. Hence, exposures are made for equiangular settings of ω with a step of $\Delta\omega$.

In analogy with previous studies of grains, it is suggested to pursue characterisation by 3DXRD at two levels of ambition:

1. A statistical analysis, where a sub-set of the illuminated cells are characterised as function of time (growth-curves). The analysis is based on monitoring the center-of-mass (CMS) position and the integrated intensity for a set of diffraction spots. The integrated intensity is proportional to the volume of the associated cell. Hence, by a suitable normalisation to the diffraction pattern of an object with a known geometry, growth curves can be determined, showing the evolution of the equivalent spherical radius with an accuracy of order 20%. Movements of the CMS position in the azimuthal direction η, see Fig. 1, are related to a rotation of the cell. These can be determined with a resolution of 0.2°.
2. A comprehensive structural analysis, where all cells within the illuminated part of the specimen are characterised. The indexing program GRAINDEX sorts the spots with respect to their element of origin [1], and produces the full orientation of each cell as well as a list of associated spots. By additional analysis, the elastic strain tensor for each cell can be determined [2].

The former approach can be based on a few images, taken at consecutive ω-positions, while the latter requires a scan in ω over ~25° (for the full strain tensor: ~120°). Hence, the time resolution differs. As such it may be relevant to combine kinetic studies based on

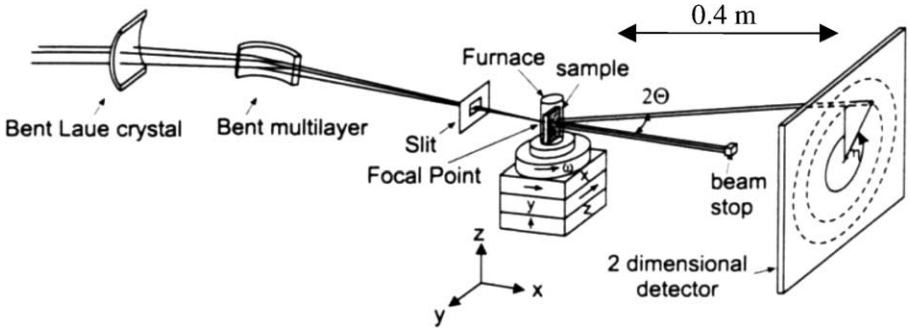

Fig. 1. Sketch of 3DXRD principle for the case of the incoming beam being focused in two directions. The Bragg angle 2θ, the rotation ω and the azimuthal angle η are indicated.

the statistical approach with a comprehensive analysis prior to and/or after the annealing. In the following focus is on the statistical analysis only.

The main limitation of 3DXRD in general is the restriction to non-overlapping diffraction spots. When used in connection with grains, this has so far limited the degree of deformation to at most 20%, as the probability of spot overlap increases quadratically with the spread in orientation within each grain. In the case of the diffraction spots arising from cells there is no or only a small intrinsic orientation spread. The limitation is then determined by the local misorientations. For a texture-free material with high angle boundaries only, simulations indicate that a few thousand cells can be characterised simultaneously [11].

3. The foil approach

The most general solution to the problem of spot overlap is to decrease the specimen thickness. To avoid an additional driving force from wedges, approximately planar foils are preferable. Using a focused beam with a width 3–4 times the average size of the cells, the foil can in favourable cases be ~50 units thick. That is sufficient that the kinetics of the cells at the center can be considered as representative of bulk behaviour. Furthermore, for reasons of statistics it may be permissible not to discriminate between surface and bulk cells. Hence, it is not required to determine the position of the cells within the foil.

First results were reported by Gundlach et al. [9]. They studied the recovery of a 40% cold-rolled Al specimen during annealing for 3 h at 300 °C. This material exhibits cells with an average size of $\sim 2\times2\times2$ μm^3 in the as-deformed state. A foil with a thickness of ~80 μm was used. Exposures with a 7×7 μm^2 beam were made repeatedly for five neighbouring ω settings with a time interval of 5 min. In the paper growth curves for nine cells are reported. Validation criteria ensure that the integrated intensities have been sampled properly, e.g. that the cells at all times have been fully illuminated by the beam. The growth of the individual cells were found to differ from the average behaviour for cells of the same size as predicted by deterministic models based on interfacial energy driven mechanisms.

With the same experimental set-up another specimen was characterised. High purity Al 0.13% Mg alloy was deformed by equal channel angular extrusion (ECAE) [12] to a very high strain, corresponding to a total reduction of 99.995% ($\varepsilon_{vm} = 10$) [13]. From EM the average cell size for the material in the as-deformed state was found to be $0.5\times0.5\times1$ μm^3.

An example of raw data is shown in Fig. 2. With an exposure time of 1 s, distinct diffraction spots are clearly visible. Based on the derived size distribution and the fact that they exhibit no discernible mosaic spread these spots are interpreted as originating from individual cells. Note also that the orientations are nearly random, reflecting a large fraction of high angle boundaries between the individual elements of the microstructure, as observed previously by EM [13].

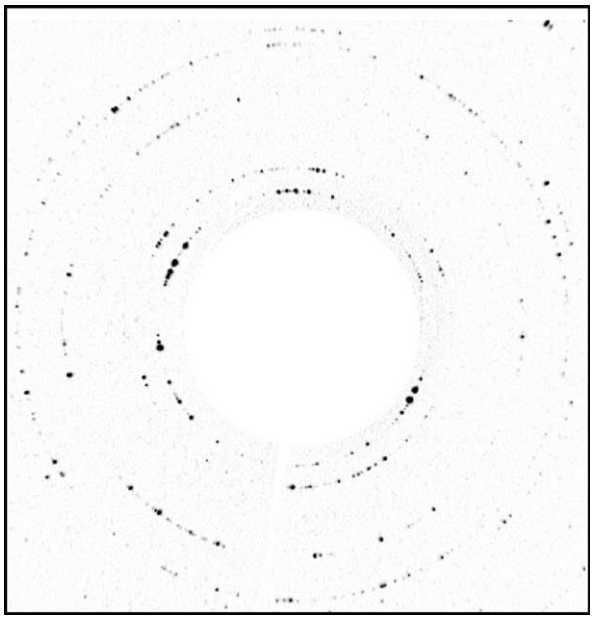

Fig. 2. Background subtracted image representing the highly strained Al specimen after 2 h of annealing at 175 °C. Black corresponds to an intensity level of 500 cts/pixel while the maximum intensities in the diffraction spots are 16,000 cts/pixel.

The first growth curve emerging from the ongoing data analysis is shown in Fig. 3. Signal-to-noise concerns was found to limit such studies of the dynamics of individual grains to those having a radius of 100 nm or more. The data set is estimated to comprise of order 50 cells suitable for such an analysis.

With this methodology some fundamental issues on the stability/coarsening of deformation-induced

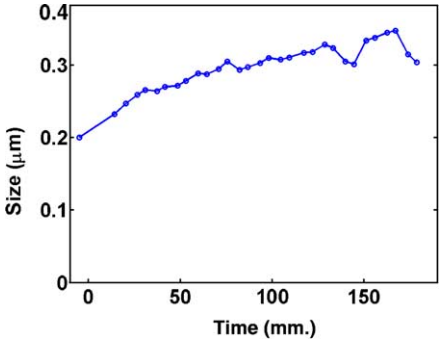

Fig. 3. A growth curve for one of the cells in the ECAE specimen. The equivalent spherical radius is shown as a function of annealing time at 175 °C.

microstructures can be addressed in a very direct way. As an example, Hu suggested in 1962 a possible coarsening mechanism. In this, two neighbouring structures rotate until they obtain the same orientation, at which point they coalesce [14]. This mechanism has been much debated, see e.g. [15]. If it occurs, the rotations would be easily observable. More generally, by quantitative analysis estimates could be provided of e.g. activation energies for recovery.

4. Bulk nucleation studies

In-situ studies of nucleation processes pose a challenge. Such studies require the identification of the "embryo", the element in the deformation-induced microstructure that eventually nucleates. In addition to the embryos being small they are in general also rare. In the extreme, the aim might be to identify and characterise a single embryo with a size of 1 μm^3 within 1 mm^3 of material, and to observe this starting to grow. It is almost impossible to find objects occurring in such small volume fractions by scanning methods. As an example, even with the fastest EBSP techniques, where up to 60 images can be acquired per second, it would on average take 200 days of un-interrupted measurements to scan a sufficient volume. Moreover, by EBSP there would be no representative way to determine which site actually becomes a nucleus.

With respect to 3DXRD, in general the foil approach will fail. For several reasons. Firstly, the investigated volume may not be sufficiently large to comprise an embryo. Secondly, the surface may act as a site for preferential nucleation. Thirdly, the recrystallization process will become retarded due to the 2D geometry. It is also an issue that the nuclei initially embedded within the foil may grow to a size comparable to the thickness. From this point onwards the dynamics is clearly not representative of bulk behaviour anymore.

Notably, in the context of phase transformations, the diffraction spots associated with the emerging phase will initially be few and appear at other Bragg angles than those of the parent phase. Hence, when illuminating large volumes the emerging nuclei can be resolved, while the individual elements in the microstructure of the parent phase cannot.

Similarly, coarsening studies of mm thick specimens are feasible in the context of recrystallization provided the dislocation structures or nuclei of interest exhibit rare orientations, that are easily detectable. Such cells are clearly not "characteristic" ones, but they are nevertheless of much interest, as they are surrounded by high angle boundaries, and therefore may be associated with a large driving force for growth.

In [10], this approach has been applied to an outstanding problem in recovery/recrystallization studies: do new orientations emerge during annealing of deformed metals, or do all the recovered cells and nuclei develop by growth of specific cells already present in the deformed microstructure? Existing recovery/nucleation models all predict that orientation should be conserved, while a number of recent EM investigations suggest that some fraction of the nuclei do appear with new orientations (e.g. [16–18]). However, due to the limitations of EM, these studies can be questioned on the basis that the deformed microstructure was not mapped over a sufficient volume.

The specimen studied by 3DXRD was an Al single crystal of the S-orientation, which had been subjected to channel die deformation to a strain of $\varepsilon = 1.5$. Previous TEM investigations had indicated that new orientations may arise during heat treatment of such crystals [19]. By 3DXRD the same total volume of 0.08 mm^3 was investigated in the as-deformed state and after 5 min of annealing at 300 °C. At this point, no nucleation events had taken place, but the microstructure had recovered. Data were acquired within a grid with the total volume being divided into 399 disjunct sub-volumes.

Shown in Fig. 4 are pole figures for a single sub-volume in the as-deformed state (a,b) and in the annealed state (c). From these figures and additional figures in the publication it is observed that:

- the pole figures for both the as-deformed and the annealed specimens exhibit distinct diffraction maxima, poles, characteristic of the single crystal. These are spread out to some extent, due to the deformation. The vast majority of the microstructure is associated with these poles and cannot be resolved with 3DXRD.
- upon annealing the poles become sharper, such that orientation components such as the one marked B disappear.
- upon annealing new distinct spots appear with orientations far from the poles. The positions of these exhibit little correlation with the position of the spots in the as-deformed state (compare (b) and (c)).

By comparing pole figures from all the grid-points, it is found that some of the emerging spots are associated with orientations that are not present in any of the 399 pole figures for the as-deformed state. This rules out the possibility of an erroneous identification of a "new orientation" due to a minor drift in position between the measurements for the as-deformed and for the annealed state.

Principally there are two ways the new minority orientation components can be generated. Either they have emerged from very rare parts of the deformed structure, associated with a very small volume fraction (in [10] the relationship is found to be $V_v < 9 \times 10^{-7}$). In addition, their size must be at the very tail of the distribution of

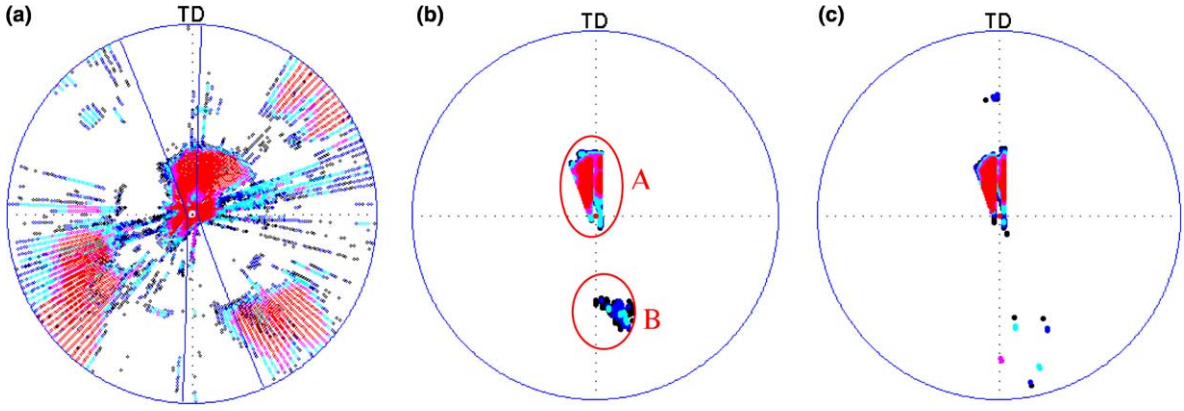

Fig. 4. {2 0 0} pole figures of a 2 mm thick deformed Al single crystal in the as-deformed state (a,b) and after 5 min of annealing at 300 °C (c). (a) is a full pole figure. To save time the characterisation was in general based on data acquisition within a limited ω-range of [0°–20°]. The corresponding part of the pole figure is indicated by two solid lines. (b,c) Partial pole figures for the same 240,000 μm^3 sub-volume within the specimen. The colour code is: [black, blue, cyan, magenta, red] for [1, 2, 5, 20, 100], with 1 corresponding to the signal-to-noise ratio. From [10].

cell sizes, as well as substantially below the classical nucleation threshold, or they have emerged by rotation.

5. Conclusions and outlook

Unique methods for studying the coarsening of individual embedded dislocation structures have been demonstrated. Methodological improvements are foreseen. These include:

- It should be possible to find the CMS position of a cell to a precision that is substantially better than the spatial resolution. This is done by monitoring the integrated intensity of an associated spot as a function of scanning the specimen along y and z. In this way the projected CMS in the directions of the two scans is found. This procedure is repeated for another spot associated with the same cell but reflecting at an angle that differs by approximately 90° in ω. Experience shows that triangulation based on the combined measurements provide the (x,y,z) CMS position with an accuracy of $\sim$1 μm.
- Diffraction spots arising from structures with a submicrometre size will be associated with an intrinsic broadening (size broadening). In the absence of a mosaic spread and a negligible point-spread-function of the detector the size broadening can be detected. In this way, an independent measure on the volumes of the cells is provided. Furthermore, information on the shape of each cell—such as its aspect ratios—would be observable, as the shape of the associated diffraction spots is related to the shape of the grain by Fourier transform.

As an alternative to the above procedures an integral 3DXRD approach is demonstrated in Ref. [20]. In this case the individual cells are not resolved, but the dislocation dynamics within a specific embedded grain is inferred from a 3D peak shape analysis of the associated diffraction spots. The information gathered is complementary to one obtained by orientation contrast studies.

In conclusion, it is demonstrated how 3DXRD microscopy enables a comprehensive and relatively fast 3D structural characterisation of polycrystalline materials over a length scale ranging from 100 nm to 1 mm. The possibility for in-situ studies of the dynamics of the individual elements in the microstructure is considered vital in order to extend beyond state-of-art models in metal science.

Acknowledgments

The authors gratefully acknowledge the Danish National Research Foundation for supporting the Centre for Fundamental Research: Metal Structures in Four Dimensions, within which this work was performed. Additional support for this work was provided by the Danish research council SNF (via Dansync). The authors thank N. Hansen, D. Juul Jensen, W. Pantleon and R.D. Doherty for valuable discussions, J. Driver for provision of the Al single crystal, and the staff of ID11, ESRF, as well as E.M. Lauridsen, S. Schmidt and L. Margulies for help with the synchrotron experiments.

References

[1] Lauridsen EM, Schmidt S, Suter RM, Poulsen HF. J Appl Cryst 2001;34:744.
[2] Poulsen HF, Nielsen SF, Lauridsen EM, Schmidt S, Suter RM, Lienert U, et al. J Appl Cryst 2001;34:751.
[3] Poulsen HF, Fu X. J Appl Cryst 2003;36:1062.
[4] Poulsen HF. Philos Mag 2003;83:2761.

[5] Lauridsen EM, Poulsen HF, Nielsen SF, Juul Jensen D. Acta Mater 2003;51:4423.
[6] Offerman SE, van Dijk NH, Sietsma J, Grigull S, Lauridsen EM, Margulies L, et al. Science 2002;298:1003.
[7] Margulies L, Winther G, Poulsen HF. Science 2001;291:2392.
[8] Poulsen HF, Margulies L, Schmidt S, Winther G. Acta Mater 2003;51:3821.
[9] Gundlach C, Pantleon W, Lauridsen EM, Margulies L, Doherty RD, Poulsen HF. Scripta Mater 2004;50:477.
[10] Poulsen HF, Lauridsen EM, Schmidt S, Margulies L, Driver JH. Acta Mater 2003;51:2517.
[11] Schmidt S, Poulsen HF, Vaughan GBM. J Appl Cryst 2003;36:326.
[12] Segal VM. Mater Sci Eng A 1995;197:157.
[13] Bowen JR, Prangnell PB, Humphreys FJ. Mater Sci Technol 2000;16:1246.
[14] Hu H. Trans Met Soc AIME 1962;224:75.
[15] Humphreys FJ, Hatherley M. Recrystallisation and related annealing phenomena. Oxford: Pergamon; 1995.
[16] Kikuchi S, Kimura E, Koiwa M. J Mater Sci 1992;27:4927.
[17] Juul Jensen D. In: Sakai T, Suzuki HG, editors. Proc 4th Int Conf on Recrystallisation and Related Phenomena. JIM; 1999. p. 3.
[18] Paul H, Driver JH, Maurice C, Jasienski Z. Acta Mater 2002;50:4355.
[19] Godfrey A, Juul Jensen D, Hansen N. Acta Mater 2001;49:2429.
[20] Pantleon W, Lienert U, Almer J, Poulsen HF. Mater Sci Eng A, in press.

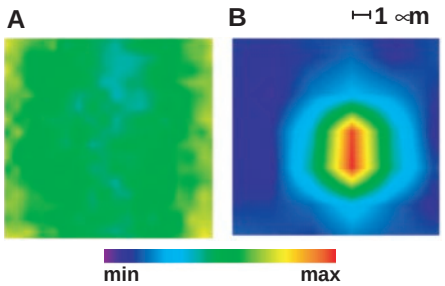

Fig. 4. μPL mapping results around defect v at (**A**) 1.3 μm (outside the PBG) and (**B**) 1.55 μm (within the PBG).

surements from regions of full PBG without defects, for reference. The excitation source and power density were the same as in the Fig. 2 experiment. The PL spectrum (Fig. 3C) for defect i shows strong emission in a broad range of wavelengths contrasting with that of the full PBG region, indicating that defect-cavity modes are created. The number of defect-cavity modes was so large that emissions from individual modes overlapped. Emission in the wavelength region from 1.45 to 1.6 μm was especially strong, suggesting that the full PBG results in enhancement of defect-mode emission by suppressing other leakage paths. When the defect size was steadily reduced from i to vii, the broad multimode emission narrowed until a single emission peak was observed for the smallest defect vii. We believe that this is emission from a nanocavity in the 3D PC.

The results for defects v to vii show that the number of defect-cavity modes becomes small enough to become distinguishable. The full width at half maximum (linewidth) (which is related to the *Q* factor) of these cavity modes, indicated by the arrows, is plotted in Fig. 3D. The calculated results obtained by the group theory–assisted FDTD method (*22*) are also shown as a function of defect size, and the number of layers in the PC is used as a parameter. It is seen that the linewidth (or the *Q* factor) is almost constant, independent of defect size, for the same number of layers. This is because optical confinement in the 3D PC is the result of the PBG effect for both the in-plane and vertical directions. In contrast, for 2D photonic crystals, the linewidth broadens (and the *Q* factor reduces) as defect size is reduced, as vertical optical confinement is imposed by total internal reflection owing to the refractive index contrast. When a 3D PC is constructed with more than 17 layers, including a lightemitting layer, linewidths of less than 0.5 nm are expected, equivalent to a *Q* factor of more than 3000.

Finally, micro-PL (μPL) mapping was performed, which gave direct information on the PBG effect and the localization of emitted light. Typical results (Fig. 4, A and B) were observed in a sample area containing defect v at wavelengths of 1.3 μm (outside the band gap) and 1.55 μm (inside the band gap). It is seen in Fig. 4A that light was emitted throughout the measured region when probed at 1.3 μm. By contrast, when the measurement was carried out within the PBG wavelength region and in resonance with the defect, emission was observed only from the defect. The area of 2 × 3 μm measured, in which strong emission was observed, is at the resolution limit of the μPL system. These results are direct evidence that light emission is suppressed in the PC region, with emission coming only from the artificial defect. The results obtained here are an important step toward the complete control of photons in PCs.

References and Notes

1. E. Yablonovitch, *Phys. Rev. Lett.* **58**, 2059 (1987).
2. S. John, *Phys. Today* **44**, 32 (1991).
3. S. Noda, K. Tomoda, N. Yamamoto, A. Chutinan, *Science* **289**, 604 (2000).
4. S. Noda, A. Chutinan, M. Imada, *Nature* **407**, 608 (2000).
5. O. Painter *et al.*, *Science* **284**, 1819 (1999).
6. B. Sogn, S. Noda, T. Asano, *Science* **300**, 1537 (2003).
7. Y. Akahane, T. Asano, B. Song, S. Noda, *Nature* **425**, 944 (2003).
8. T. Baba, N. Fukaya, J. Yonekura, *Electron. Lett.* **35**, 654 (1999).
9. T. D. Happ, M. Kamp, A. Forchel, *Opt. Lett.* **26**, 1102 (2001).
10. P. Kramper *et al.*, *Phys. Rev. Lett.* **92**, 113903 (2004).
11. T. F. Krauss, R. M. De La Rue, S. Brand, *Nature* **383**, 699 (1996).
12. M. Notomi *et al.*, *IEEE J. Quantum Electron.* **38**, 736 (2002).
13. S. J. McNab, N. Moll, Y. A. Vlasov, *Opt. Express* **11**, 2927 (2003).
14. H. Benisty *et al.*, *J. Lightwave Technol.* **17**, 2063 (1999).
15. K. M. Ho, C. T. Chan, C. M. Soukoulis, R. Biswas, M. Sigalas, *Solid State Commun.* **89**, 413 (1994).
16. J. G. Fleming, S. Y. Lin, *Opt. Lett.* **24**, 49 (1999).
17. I. Bulu, H. Caglayan, E. Ozbay, *Phys. Rev. B* **67**, 205103 (2003).
18. M. Megens, J. Wijnhoven, A. Lagendijk, W. L. Vos, *Phys. Rev. A* **59**, 4727 (1999).
19. S. Noda *et al.*, *IEEE J. Quantum Electron.* **38**, 726 (2002).
20. S. G. Romanov *et al.*, *J. Appl. Phys.* **91**, 9426 (2002).
21. S. Ogawa, M. Imada, S. Noda, *Appl. Phys. Lett.* **82**, 3406 (2003).
22. M. Okano, S. Noda, in preparation.
23. This work was mainly supported by Core Research for Evolution Science and Technology (CREST), Japan Science and Technology Agency; and partly supported by a Grant-in-Aid for Scientific Research and Information Technology program of the Ministry of Education, Culture, Sports, Science and Technology of Japan.

17 March 2004; accepted 21 May 2004
Published online 3 June 2004;
10.1126/science.1097968
Include this information when citing this paper.

Watching the Growth of Bulk Grains During Recrystallization of Deformed Metals

S. Schmidt,[1]* S. F. Nielsen,[1] C. Gundlach,[1] L. Margulies,[1,2] X. Huang,[1] D. Juul Jensen[1]

We observed the in situ growth of a grain during recrystallization in the bulk of a deformed sample. We used the three-dimensional x-ray diffraction microscope located at the European Synchrotron Radiation Facility in Grenoble, France. The results showed a very heterogeneous growth pattern, contradicting the classical assumption of smooth and spherical growth of new grains during recrystallization. This type of in situ bulk measurement opens up the possibility of obtaining experimental data on scientific topics that before could only be analyzed theoretically on the basis of the statistical characterization of microstructures. For recrystallization, the in situ method includes direct measurements of nucleation and boundary migration through a deformed matrix.

When a material is deformed plastically, excess line defects (dislocations) and some excess point defects are introduced into the material. The density of these excess defects can be reduced by means of annealing. Basic processes that take place during annealing are recovery, recrystallization, and grain growth.

Recrystallization resembles crystallization in that both require nucleation and growth stages, but the processes are in fact very different. Recrystallization occurs in an already solid crystalline material, and thus the atoms have to move from one lattice arrangement in the deformed material into a new and more perfect one. Therefore, the nucleation of recrystallization does not occur in its classical sense by random atomic fluctuations. Also, it is the motion of atoms at the interface between the recrystallized grain and the deformed matrix that determines growth rates, and therefore the local heterogeneities at these interfaces must be considered. Recent detailed quantitative transmission electron microscopy (TEM) analysis has revealed that the deformed microstructure in metals is heavily subdivided into small, typical-

[1]Center for Fundamental Research, Metal Structures in Four Dimensions, Risø National Laboratory, 4000 Roskilde, Denmark. [2]European Synchrotron Radiation Facility, Boîte Postale 220, 38043 Grenoble, France.

*To whom correspondence should be addressed. E-mail: soeren.schmidt@risoe.dk

ly micrometer-sized volume elements of different crystallographic orientations (*1*). Furthermore, the orientation of the crystal or the original grain in a polycrystalline sample affects this subdivision, which leads to heterogeneous microstructures (*2*, *3*). Understanding the nucleation and growth processes that occur during recrystallization thus requires local-scale dynamic data.

Experimentally, such data can be obtained only for near-surface volumes by techniques such as electron back-scattering characterization in the scanning electron microscope (*4*, *5*) or laboratory-based x-ray diffraction (XRD) of weakly deformed bicrystals (*6*). However, in such experiments, the effects of the free surface(s) on the observations are not known, and the data only reveal a two-dimensional (2D) picture of the annealing processes. Alternatively, it is often preferred to rely on a static, statistical analysis, averaging over groups of grains in a series of partially recrystallized samples. These data are then used in combination with modeling to estimate nucleation and growth rates (*7*). However, such an analysis does not address the local-scale effects on a volume basis.

Various types of recrystallization models are used. They all have, however, limitations because of the lack of suitable experimental data that can be used either as input to the models or as verifications of the modeling results. The classical models generally consider the deformation microstructure as a continuum whereby the local-scale effects are again neglected. Recent cellular automata (*8*), network models (*9*, *10*), and Monte Carlo simulations (*11*) do include realistic deformation structures but suffer from a lack of validated nucleation mechanisms as well as boundary mobilities and energies. For the latter two, empirical functions are used that are supported mostly by grain growth experiments—i.e., experiments where the driving pressure is given by the reduction in grain boundary energy and not the energy stored in the deformed matrix. This means that the driving pressure is typically two to three orders of magnitude lower than that in a recrystallization process. As a result, despite the substantial effort devoted to recrystallization modeling, limited basic knowledge about the fundamentals of nucleation and growth have been obtained, and even simple properties such as the recrystallization grain size and texture are often not predicted correctly.

We studied recrystallization with a focus on the growth of new grains. We chose to use aluminum of so-called commercial purity (AA1050) because (i) the results obtained would be of more general value than if superpure aluminum were used, and (ii) the microstructure is much more stable in slightly impure aluminum than in superpure aluminum. Also, we have experience studying recrystallization in AA1050. The chemical composition is given in Table 1. The initial material contained 0.5 volume % $FeAl_3$ and FeAlSi particles, which had an average diameter of 1.7 μm and were relatively uniformly distributed (*12*). A single crystal with the initial orientation of {110}⟨001⟩ (i.e., Goss orientation) was grown by the Bridgman technique from this initial material. To ensure that there was enough driving pressure for recrystallization while still keeping a relatively simple deformed microstructure, the sample was deformed by rolling to a 42% reduction of its original thickness, resulting in a final thickness of 1 mm along the normal direction (ND). Afterward, the sample was cut into smaller pieces with dimensions of 6 mm along the rolling direction (RD) and 5 mm along the transverse direction (TD). A montage of TEM micrographs is shown in Fig. 1. The structure is subdivided by elongated, almost planar dislocation boundaries inclined at 30° to 35° to the RD. The distances between these boundaries are typically in the range of 0.5 to 3 μm. Crystallographic orientation determinations (*13*) revealed that only small misorientations, on average 1.8°, exist across these boundaries. On top of this primary set of dislocation boundaries, a second set, often in the form of microbands consisting of small elongated cells, is seen at –30° to –35° to the RD. The boundaries between these cells have a much larger spacing, typically in the range of 4 to 20 μm, and are associated with substantially larger misorientation; angles of up to 8° are observed.

To stimulate controlled nucleation, the TD-ND surface on the sample was locally deformed by pyramid-shaped diamond hardness indentations positioned in a regular square grid. The indentation load was 2 kg. This type of sample was first used in the original work of Beck *et al*. (*14*) and was later used by Lücke *et al*. (*15*).

The growth of the recrystallizing grain was observed by means of the 3DXRD microscope (*16*) at beamline ID-11 at the European Synchrotron Radiation Facility. A schematic view of the experimental setup is shown in Fig. 2.

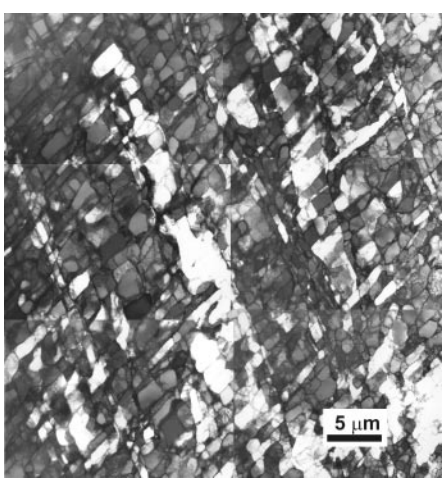

Fig. 1. A montage of micrographs of 42% cold, rolled Al single crystal with an initial orientation of {110}⟨001⟩. The structure is subdivided by elongated, almost planar dislocation boundaries inclined at 30° to 35° to the RD. On top of this primary set of dislocation boundaries, a second set, often in the form of microbands consisting of small elongated cells, is seen at –30° to –35° to the RD.

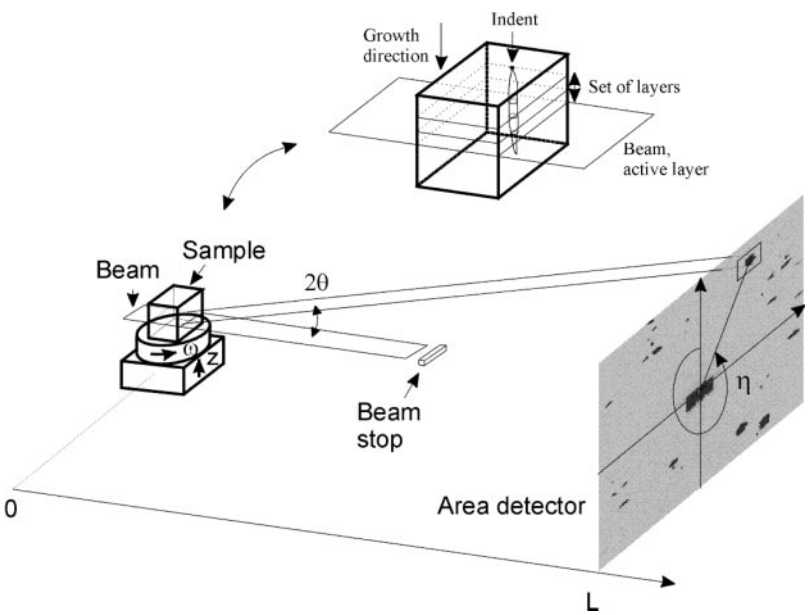

Fig. 2. Sketch of experimental setup. Coordinate system (*x*,*y*,*z*) and angles (ω,2θ,η) are defined. The *x* axis is along the beam direction, the *y* axis is transverse to the beam direction, and the *z* axis is normal to the beam plane. For the diffraction spot in question, the direction of the diffracted beam is parameterized by the angles 2θ and η. The right-hand rotation of rotation stage around the *z* axis is given by the angle ω. All grains within the stripe illuminated by the beam will give rise to diffracted spots during scanning of ω. The inset shows the principle of obtaining a picture of the grain by repeatedly recording a oscillation photograph followed by a vertical translation of the sample stage. L denotes the distance between the sample and the CCD detector.

The synchrotron beam was focused vertically with a bent Laue crystal to a full width at half maximum (FWHM) of 6 μm at the focal point. The width of the beam in the horizontal direction, defined by slits, was 600 μm. The energy of the monochromatic beam was 52 keV. Every volume element fulfilling the Bragg condition inside the illuminated region of the sample would give rise to a diffraction spot on the charge-coupled device detector positioned about 10 mm downstream from the sample. All volume elements in the illuminated region would fulfill the Bragg criterion at least once by recording a set of oscillation images, a so-called ω scan, in which each image covers a 1° range of the ω range (−45° to +45°), where ω is the rotation angle of the rotation stage (Fig. 2).

To anneal the sample in situ, a furnace was mounted on the rotation stage. The sample was mounted in the furnace such that for ω = 0, ND was parallel to the beam direction with the hardness indentations on the top surface, which was parallel to the beam plane. Initially, an ω scan was performed with the incoming beam plane intersecting the sample just below the surface. Afterward, a Bragg reflection from a recrystallizing grain was identified in one of the oscillation images. The measurements were then collected at the given ω position by successively translating the sample 6 μm vertically and recording an oscillation image. Hence, each image constituted a cross section of the grain (inset in Fig. 2).

A 3D shape of the grain was reconstructed in the following way: Before background subtraction and normalization to the synchrotron current, the images were deconvoluted by the point-spread function of the detector. The resulting cross section of the grain as seen on the detector was related to the real cross section in the sample reference system by an affine transformation T,

$$T = \Omega^{-1}A^{-1}$$

$$A = \begin{pmatrix} -\tan 2\theta \sin\eta & 1 \\ \tan 2\theta \cos\eta & 0 \end{pmatrix}$$

$$\Omega = \begin{pmatrix} \cos\omega & \sin\omega \\ -\sin\omega & \cos\omega \end{pmatrix}$$

where A^{-1} projects the cross section from the vertical plane (the detector) along the direction of the diffracted beam into the horizontal plane, and Ω^{-1} rotates the projection around the vertical axis into the sample reference system. The angles (ω, 2θ, and η) (definitions in Fig. 2)

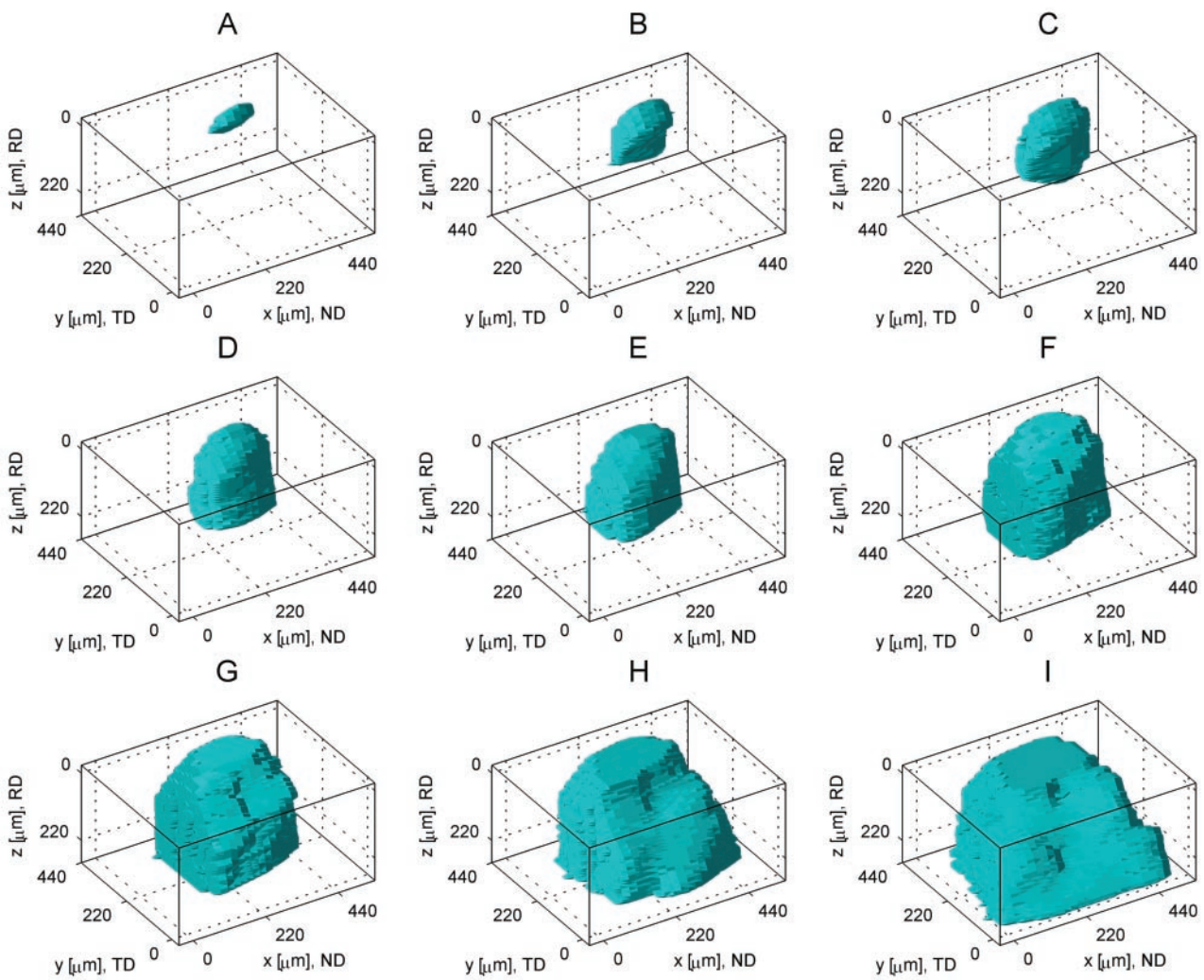

Fig. 3. Storyboard of the expansions of the grain in the sample reference system. The storyboard contain pictures 1, 12, 17, 27, 39, 49, 59, 72, and 73 (**A** to **I**). The annealing temperature as a function of time is shown in fig. S1. In the sample reference system, the *x* axis coincides with the ND, the *y* axis coincides with the TD, and the *z* axis coincides with RD. The surface of the sample was roughly at $z = 0$. The grain started out as a small flattened object in picture 1 (A). Later, a clear change in the grain shape was observed in picture 17 (C), in which the grain had expanded 198 μm along the *x* axis and 180 μm along the *z* axis but only 85 μm along the *y* axis (movie S1). By comparing pictures 39 and 72 [(E) and (H)], it was seen that at different times, different parts of the grain were leading in the expansion along the *y* axis. In picture 39, the left part of the grain, near $(x, y) = (220\ \mu m, 220\ \mu m)$, was leading, as opposed to picture 72, in which the right part was leading.

were measured to $\omega = -9°$, $2\theta = 14.7°$, and $\eta = 220°$ [i.e., a (331) reflection]. During the transformation, the voxel intensities in the sample reference system were interpolated from the pixel intensities on the detector conserving the integrated intensity in the diffraction spot. Finally, a complete picture of the grain shape was obtained by stacking the reconstructed cross sections. Because the pixel size of the detector was 4.3 by 4.3 μm, the spatial resolution in the sample reference system was 22 μm along the *x* axis and 4.3 μm along the *y* axis. The resolution along the *x* axis was worse because of the low inclination of the diffracted beam.

The sample had a preannealing period of 1 hour at 260°C. Afterward, a grain was observed just below the sample surface. During the following 30 hours, 73 pictures were recorded while annealing at temperatures between 280° and 290°C, apart from the final picture, for which the annealing temperature was raised to 310°C. Each picture took 7.5 min and there was an idle period of about 17 minutes between each completed picture and the initiation of the next. A subset of the pictures is shown in Fig. 3. All 73 pictures can be seen in movie S1. As stated earlier, this analysis is based on one Bragg reflection yielding different spatial resolutions along the *x* and *y* axes. By combining the information contained in several reflections from the same grain, the overall spatial resolution can be improved to 5 μm (*17*), which corresponds to the length of a few cells in the deformed microstructure. In addition, knowing the crystallographic orientation of the grain, which can be deduced with a program such as GRAINDEX (*18*), the misorientation between the recrystallizing grain and the mean orientation of the neighboring cells can be calculated.

The data show that the grains may be very irregular in shape and the growth may occur by abrupt movements of individual boundary segments. Analysis of data for the growth of two more grains confirms that this is typical for the growth of all the grains measured so far. This is a remarkable result given that recrystallization is generally considered to occur by steady-state boundary migration, similar to the growth of a soap bubble, particularly in simple systems like this one. Our results are similar to those that are often observed by in situ electron microscopy (EM) observations (*5*, *19*). However, with these EM observations, doubt always exists if the reason for such unexpected observations is related to the effects of the free sample surface(s).

For our bulk results, for which this uncertainty does not exist, reasons for the irregular shape and abrupt movement may relate to local inhomogeneities in the deformation microstructure and orientation distribution, as well as local particle pinning of the boundary.

The importance of particle pinning may be estimated by comparing the driving pressure acting on the moving boundary to the Zener drag caused by the particles. Applying values typical for our experiment (Table 2), we found that the driving pressure from the classical equation is 0.4×10^6 N/m^2, which is close to the value calculated on the basis of the microstructure characterization with the Read-Shockley equation giving 0.3×10^6 N/m^2. This is comparable to the driving pressure derived from stored energy measurements (*20*) of 0.38×10^6 N/m^2. In comparison, the Zener drag is $P_z = 0.03 \times 10^6$ N/m^2 (i.e., about a factor of 10 lower than the driving pressure). Particle effects are therefore not considered to be the major reason for the irregular grain-shape evolution and abrupt movement.

Other effects relating to local inhomogeneities in the deformed matrix and orientation distributions must be sought. Because the dislocations, which provide the driving pressure for recrystallization, are not uniformly distributed in the deformed microstructure but are organized into dislocation boundaries (Fig. 1), the moving boundary may experience quite large variations in the local driving pressure. Also, the misorientations across the boundary will vary from point to point on the boundary, and the conditions will change as the boundary moves. Such effects could well give rise to inhomogeneities as those observed by the 3DXRD experiment. In addition, one may speculate on how adoption of individual dislocation boundaries into a recrystallizing grain takes place and how that affects the growth process. Further 3DXRD experiments with improved spatial resolution seem ideal to address such issues.

Experiments of the present type are essential for understanding the fundamental mechanisms of grain boundary migration through a deformed matrix containing a high concentration of dislocations and dislocation boundaries. Furthermore, it may provide a direct determination of grain boundary mobilities and energies essential for realistic recrystallization modeling. The data may also be used for direct comparison of computer simulations, including those involving molecular dynamics. Such simulations have not yet been done, essentially because no experimental data existed to validate the results.

Table 1. Chemical composition of AA1050 (weight %).

A1	Fe	Mg	Mn	Si	Cu	Ca	Na	Ti	B
99.46	0.3384	0.0011	0.0026	0.1538	0.0019	0.0002	0.0005	0.0066	0.0021

Table 2. Quantities used in the estimation of the driving pressure and the Zener drag in the Al sample. The quantities are: *f*, the volume fraction of particles; γ_b, the boundary energy of the moving boundary; r_0, the particle radius; *G*, the shear modulus; *b*, the Burger's vector; ρ, the dislocation density; *d*, is the cell size; and θ, the average misorientation in the deformed microstructure.

f (volume %)	γ_b (J/m^2)	r_0 (μm)	*G* (GPa)	*b* (nm)	ρ (m^{-2})	*d* (μm)	θ (°)
0.5	0.324	0.85	25.4	0.286	2×10^{14}	1.5	2

References and Notes

1. N. Hansen, *Metall. Mater. Trans. A* **32**, 2917 (2001).
2. J. H. Driver, D. Juul Jensen, N. Hansen, *Acta Metall. Mater.* **42**, 3105 (1994).
3. G. Winther, *Acta Mater.* **51**, 417 (2003).
4. B. Hutchinson, *Proc. ICOTOM-11*, Eleventh International Conference on Textures of Materials, Xi'an, China, (1996), p. 377.
5. F. J. Humphreys, www.umist.ac.uk/material/staff/academic/fjh/SEM-PSN.htm.
6. D. A. Molodov, *Recrystallization and Grain Growth* in *Proceeding of the First Joint International Conference*, RWTH Aachen, Germany, 2001, vol. 1, p. 21.
7. R. A. Vandermeer, D. Juul Jensen, *Acta Metall. Mater.* **42**, 2427 (1994).
8. V. Marx, F. R. Reher, G. Gottstein, *Acta Mater.* **47**, 1219 (1999).
9. C. Maurice, J. Humphreys, *Proc. ICGG-3, Third International Conference on Grain Growth*, Carnegie Mellon University, Pittsburgh, PA, (June 1998), vol. 1, p. 81.
10. F. J. Humphreys, *Acta Mater.* **45**, 4231 (1997).
11. B. Radhakrishnan, G. B. Sarma, T. Zacharia, *Acta Mater.* **46**, 4415 (1998).
12. K. D. Vernon-Parry, T. Furu, D. Juul Jensen, F. J. Humphreys, *Mater. Sci. Technol.* **12**, 889 (1996).
13. Q. Liu, *Ultramicroscopy* **60**, 81 (1995).
14. P. A. Beck, *Adv. Phys.* **3**, 245 (1954).
15. K. Lücke, R. Rixen, M. Senna, *Acta Metall.* **24**, 103 (1976).
16. H. F. Poulsen *et al.*, *J. Synchrotron Rad.* **4**, 147 (1997).
17. H. F. Poulsen, X. Fu, *J. Appl. Crystallogr.* **36**, 1062 (2003).
18. E. M. Lauridsen, S. Schmidt, R. M. Suter, H. F. Poulsen, *J. Appl. Crystallogr.* **34**, 744 (2001).
19. I. M. Fielden, J. Cawley, J. M. Rodenburg, in Proceedings of the *Institute of Physics Electron Microscopy and Analysis Group Conference 2003*, University of Oxford, UK, S. McVitie *et al.*, Eds. (Institute of Physics Conference Series, Institute of Physics Publishing, Bristol, UK, 2004), vol. 179, p. 181.
20. R. A. Vandermeer, P. Gordon, in *Recovery and Recrystallization of Metals*, L. Himmel, Ed. (Interscience, New York, 1963) p. 211.

21. We thank the Danish National Research Foundation for supporting the Center for Fundamental Research, Metal Structures in Four Dimensions, within which this work was performed; support from the Danish Natural Science Research Council via Dansync as well as European Synchrotron Radiation Facility for provision of synchrotron radiation facilities; the beamline staff at ID-11 for assistance in using the beamline; and R. A. Vandermeer, B. Ralph, H. F. Poulsen, G. Winther, and N. Hansen for useful discussions.

Supporting Online Material

www.sciencemag.org/cgi/content/full/305/5681/229/DC1
Fig. S1
Movie S1

1 April 2004; accepted 24 May 2004

Materials Science Forum Vols. 467-470 (2004) pp. 81-86
online at http://www.scientific.net

In-Situ Investigation of Bulk Nucleation by X-Ray Diffraction

A.W. Larsen[1], C. Gundlach[1], H.F. Poulsen[1],
L. Margulies[1+2], Q. Xing[1], D. Juul Jensen[1]

[1] Center for Fundamental Research: Metal Structures in Four Dimensions,
Materials Research Department, Risoe National Laboratory, DK-4000 Roskilde, Denmark

[2] ID11, ESRF, 38043 Grenoble Cedex 9, France

Keywords: Nucleation, Triple junctions, 3DXRD, X-Ray Diffraction, Orientation measurements

Abstract. A new method for *in-situ* studies of nucleation in bulk metals based on high energy synchrotron radiation is presented. Copper samples cold rolled 20% are investigated. The crystallographic orientations near triple junctions are characterized using non-destructive 3DXRD microscopy before, during, and after annealing for 1 hour at 290°C. This method allows in-situ identification of new nuclei and the deformed material, which spawns the nuclei. Also, since data is acquired during annealing nucleation kinetics can be studied.

Introduction

Studies of bulk nucleation have always been hampered by the fact that it has been impossible to know the exact microstructure at the exact nucleation sites *before* the nuclei emerged.
It is possible to perform microscopic scanning electron microscopy (SEM) and transmission electron microscopy (TEM) studies of nucleation, where the starting structure is known [1,2]. But in both cases it is not possible to rule out surface effects. In SEM studies there is also the added problem of grains growing up from the hidden bulk sample below the surface.

With high X-ray energies (50 keV) a 10% transmission through a thickness of 25 mm of Al, 1.5 mm of Fe, and 1 mm of Cu is obtained, thus allowing non-destructive probing of the *bulk* of metal samples. By using samples of a suitable thickness it is possible to characterize the microstructure within a column through the sample, which is representative of the bulk microstructure. Depending on the X-ray beam spot size, the measurement time, and the material being investigated, a sub-micron volume resolution can be achieved.
Poulsen et al have shown that it is possible to perform in-situ studies of recovery in a deformed Al single crystal using 3DXRD microscopy [3].

Earlier studies of nucleation have shown that areas near triple junctions are likely sites for nucleation [2,4], so in this study we limit ourselves to volumes near triple junctions. The purpose of this paper is to explain in detail the experimental procedure and illustrate it's potentials, by showing the first results obtained with the method.

The 3DXRD microscope

The 3D X-ray diffraction (3DXRD) microscope[1] works in the X-ray energy regime of 40-100 keV [5]. It is installed in the second hutch of ID11, which is a high energy beamline at the ESRF[2] (Grenoble, France). The X-ray beam can be focused down to a 2x5 μm^2 spot, using double focusing

[1] http://www.risoe.dk/afm/synch/3dxrd.htm
[2] http://www.esrf.fr/exp_facilities/ID11/handbook/welcome.html

from a bent Laue Si-111 crystal and a bent multilayer, giving a maximum flux of $\Phi_0=1.5\cdot10^{10}$ (photons/sec/μm^2) on the sample with an energy bandwidth of 0.06-1%.
A schematic diagram of the 3DXRD microscope can be seen on Fig. 1.
The 3DXRD microscope allows static and dynamic studies of the microstructure of solid bulk samples. The high transmission and photon flux allows the reflections from individual crystallographic grains to be detected, and specialized software allows these reflections to be indexed back to the individual grains, thus allowing individual grains to be followed in-situ.
Slits placed right in front of the sample precisely define the spot size, and several different detectors of varying resolution are available. It is possible to mount a furnace (used in this study), a cryostat, a tensile stress rig, or a torsion device on the sample stage, thus allowing in-situ studies of phase transformations, annealing, and deformation.

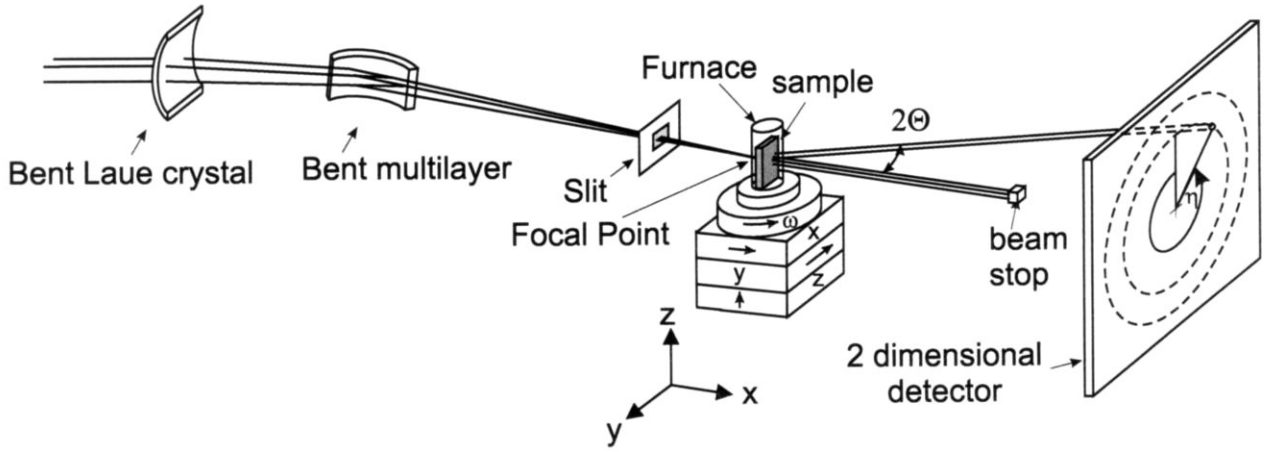

Figure 1: *Schematic diagram of the 3DXRD microscope. The 1×1 mm^2 white X-ray beam enters from the left, where it is monochromated and focused in the vertical plane using a bent Laue Si-111 crystal. Horizontal focusing is performed with a bent multilayer. A slit in front of the sample defines the size of the beam on the sample. The sample can be translated in the x, y, z-direction, ω is the sample rotation around the z-axis, and it is possible to tilt the sample around the x and y-direction.*

Sample preparation

The sample material is 99.995% Vol. pure copper, which is initially cold rolled 20%, and then annealed for 8 h at 700°C. This results in an inhomogeneous grain size distribution with an average grain size of about 500 µm. This starting material is additionally cold rolled 20% to a thickness of 25.6 mm. During cold rolling the *l/h* ratio is equal to 1.2, and the deformation is therefore expected to be uniform throughout the thickness of the material [6]. Here *l* is the cordal length of the contact area with the rolls, and *h* is the sample thickness.

From the rolled material a thin 10×10 mm^2 sample is cut out, and the sample surface (the RD/ND plane) is polished down to a thickness of 0.3 mm (see Fig. 2), using a Logitech PM5D polishing and lapping machine with a PSM1 sample monitor[3] [7], where polishing is performed from both sides. Lastly, the sample is electrochemically polished, with a D2-electrolyte[4] for 5 seconds at 10 V, to remove any remnant surface deformation or sub-micron scratching (i.e., surface nucleation sites).

[3] http://www.logitech.uk.com/
[4] D2: 500 ml H_2O, 250 ml H_3O_4P, 250 ml ethanol, 2 ml Vogel's Sparbeize, 50 ml propanol, and 5 g H_2N CO NH_2 (urea)

An illustration of the sample geometry can be seen on Fig. 2.

Initially, the surface microstructure of the sample is studied to determine the surface positions of the triple junctions within a chosen area on the surface. The surface microstructure of a 1.8×1.8 mm^2 area is characterized by electron backscatter patterns (EBSP), producing an orientation image map (OIM) of the area in studied [8,9]. A JEOL JSM-840 scanning electron microscope, with a LaB_6-filament is used to collect the data, and the step size is 20 µm. From the OIM, an area containing one or more well defined triple junctions is chosen for 3DXRD studies (see Fig. 2).

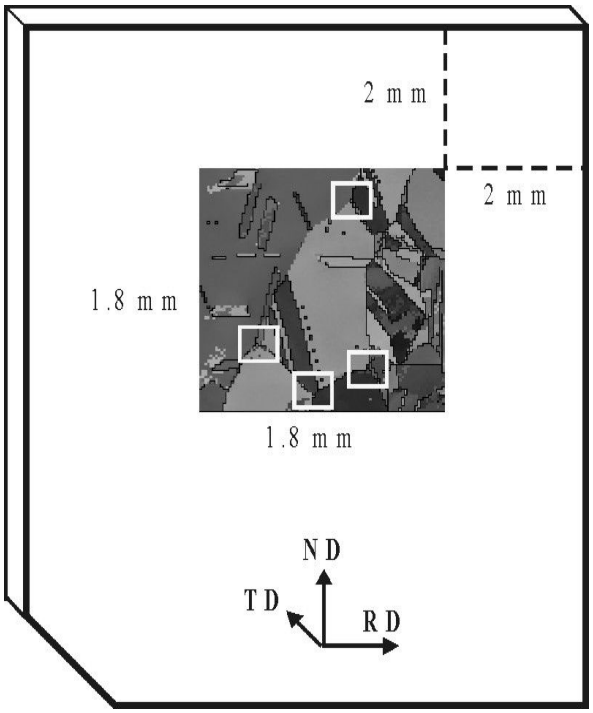

Figure 2: *Sample geometry. Side lengths are less than 10 mm, and thickness is 0.3 mm. The RD, ND, and TD-directions are respectively oriented along the y, z, and x-axis in the 3DXRD microscope (see Fig. 1).*
The upper right corner of the OIM is located 2 mm below the top edge and 2 mm to the left of the right edge. Note that the relative size of the OIM has been exagerated to make the microstructure more easily discernable. The white squares indicate the position of suitable triple junctions.

A TEM foil is taken parallel to the RD/ND plane, and prepared by electro polishing. From this the average distance between dislocation boundaries (the cord length) within the deformed material is determined using a JEOL-2000FX transmission electron microscope, operating at 200 kV. The average cord length is found to be about 0.5 µm, and the smallest length is ~0.15 µm.

3DXRD experiment

For the 3DXRD experiment, an energy of E=50.77 keV (λ=0.2442 Å) is chosen, giving a transmission of 50% through the 0.3 mm thick copper samples. A 1024×1024 pixel Frelon[5] CCD-detector was placed 333 mm from the sample, allowing for the simultaneous full recording of the four Debye-Scherrer rings of lowest multiplicity: [111], [200], [220], and [311].
The sample is mounted within a furnace (see Fig. 1), with the RD/ND plane perpendicular to the X-ray beam (see Fig. 2). It is possible to heat and cool the sample within the furnace, which consists of a 0.1 mm thick glass capillary tube with a thermocouple in the middle. This can be done in vacuum or in an argon atmosphere.

[5] http://www.esrf.fr/experiments/ISG/SpecialDetectors/AreaDiffraction.php

The approach is in detail to map a 40×40×300 μm^3 volume (grid area × sample thickness), centered on a triple junction in the as-deformed sample. The sample is then heated to 290°C, and data is continually collected from the same volume with a time resolution of 6 min. After 1 hour, the sample is cooled to room temperature, and the same 40×40×300 μm^3 volume is mapped again.
By comparing the post-annealed with the pre-annealed data, it is possible to locate new nuclei, and the microstructure from which it grew. If the new nuclei yields more than one diffraction spot, it is possible to determine the nuclei's maximum distance from the sample center by triangulating the positions of the diffraction spots.

To avoid spot-overlap (different sample volumes diffracting into the same position on the detector), it was decided to limit the number of grains intersected by the X-ray beam penetrating through the sample. The solution is to make the grain size and the sample thickness comparable, while keeping the sample thick enough for the microstructure to have true bulk properties. This lead to the chosen 0.3 mm sample thickness. Also, the sample is cold rolled 20%, only creating a moderate deformation and therefore only a moderate broadening of the poles. With this approach, it is typically possible to observe all the broadened reflections (poles) from the 3 grains at a triple junction *without* spot-overlap.

The time and ω resolutions are chosen as 1 second and 1° respectively. To make sure that the sensitivity of the 3DXRD microscope is high enough to detect the deformed cells, a small X-ray beam size is chosen: the beam is horizontally and vertically focused down to a 20x20 μm^2 spot.
To detect a cell, the diffracted intensity from that cell must be at least twice that of the background noise. A textureless aluminium foil of known thickness is used to calibrate the volume detection limit, and from that a volume detection limit of $(0.26\ \mu m)^3$ is determined for copper.

For the experiment, the microstructure of a 2×2 grid (40x40 μm^2 area), centered on a triple junction, which is chosen from the OIM, is characterized at different time steps. At each grid point a 1 second ±0.5° rocking curve scan is performed at ω positions from -20° to 20° in 1° increments. This angular range is sufficient to cover all crystallographic orientations.
The as-deformed triple junction is characterized at room temperature, after which the sample is heated to 290°C. When at temperature, identical 2×2 grid scans are continually performed at the same sample position. Each grid point contains 42 rocking curve scans (each taking ~2 seconds), and since there is 4 of these, it corresponds to a complete 2×2 grid scan roughly once every 6 minutes, thus allowing us to follow nucleation in-situ as a function of time with that time resolution.

The choice of a 20x20 μm^2 spot size is a compromise between spatial and time resolution. It is possible to focus the X-ray beam as far down as a 2x5 μm^2 spot, but since studying in-situ nucleation is a 'needle in the haystack' problem, a larger area would still have to be covered, requiring many more grid points, and the corresponding time resolution would make dynamical studies impossible.

Because the smallest observed cells (~0.15 μm) in the deformed structure are just smaller than the volume detection limit $(0.26\ \mu m)^3$, an additional high sensitivity measurement on an as-deformed sample is also performed. This measurement has a time and ω resolution of respectively 15 seconds and 0.5°, giving a volume detection limit of $(0.15\ \mu m)^3$, and thus allowing us to see the smallest length/cells observed in the TEM study.

Results

In the diffraction images from the as-deformed samples, the reflections are seen as elongated poles, as would is seen in the diffraction patterns from deformed crystals. Due to the moderate deformation (20%), even when all three grains diffract into the same image, the Debye-Scherrer rings are still *not* fully filled with reflections (see Fig. 3a). As heating progresses, nuclei are seen to appear as sharp diffraction spots with very low mosaic spread and intensity increasing with time (see Fig. 3b).
In Fig. 3, diffraction images from the same volume of the sample before and after annealing can be seen. In this case, the nucleus clearly forms with an old (already existing) orientation.
Triangulating the positions of the diffraction spots from the nuclei shows where the nuclei are inside the sample. It is therefore possible to determine whether a detected nucleus has formed in the sample bulk or on the sample surface.

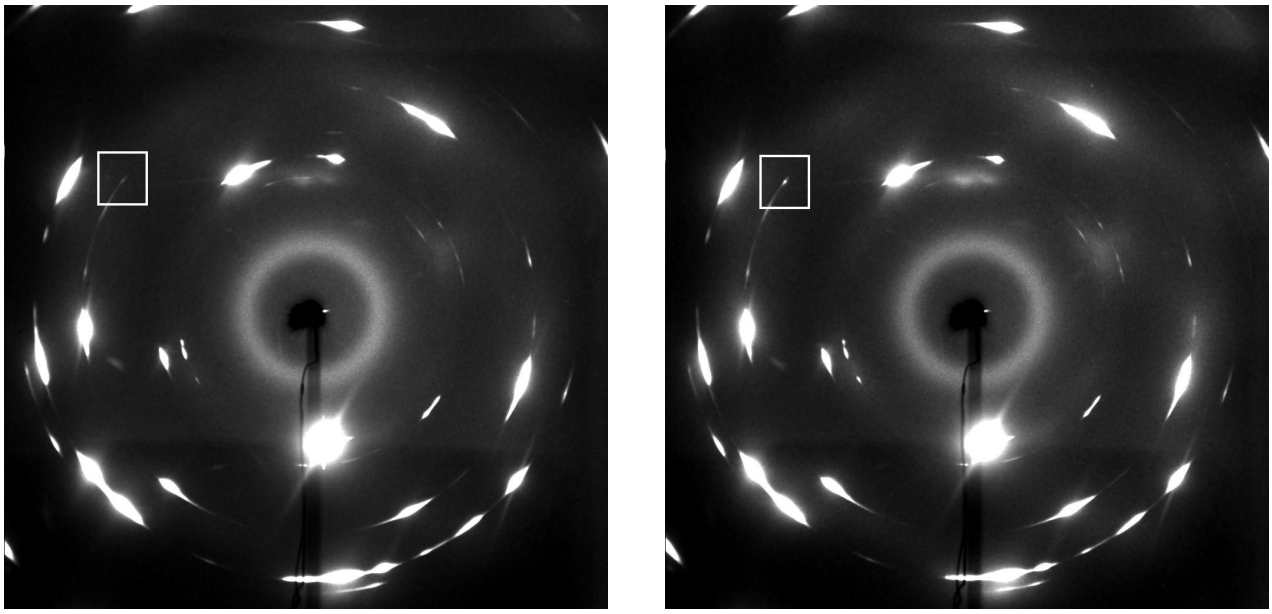

(a) **(b)**

Figure 3: *Example of experimental data. The two figures show the raw X-ray diffraction data as seen on the detector.* ***(a)*** *in the as-deformed state; and* ***(b)*** *after annealing for 3 hours at 290 °C. The white square indicates where in the diffraction images a nucleus can be seen to appear.*

In general, the nuclei are observed primarily within the existing crystallographic orientations (the poles, see Fig. 3b), but some nuclei are also seen to form with orientations *not* previously found within the poles of the as-deformed sample.
In this case, the high sensitivity images of the as-deformed sample confirm that no diffraction spots are observed in the space between the crystallographic poles. This means that *before* the onset of annealing, no cells of volumes larger than $(0.15\ \mu m)^3$ have orientations outside the poles.
Further analysis will show if these new orientations are within annealing-twin orientations, results of grain rotations, or if they are indeed completely new orientations inherent to the annealing process itself.

Conclusion

A new method for in-situ studies of bulk nucleation has been presented. The method has allowed for the in-situ detection of new *bulk* nuclei, while they formed and therefore, the nucleation kinetics could be followed. It has been confirmed that triple junctions are good nucleation sites.
With this method, there is no 'lost evidence', i.e., the parent bulk microstructure is fully characterized *before* the nuclei form.
In the present preliminary investigation: Nuclei with crystallographic orientations corresponding to the orientations already observed in the deformed structure are seen (see Fig. 3); but some nuclei, which form with orientations not previously observed in the microstructure are seen as well.

Acknowledgements

The authors gratefully acknowledge the Danish Research Foundation for supporting the Center for Fundamental Research: Metal Structures in Four Dimensions, within which this work was performed.

References

[1] T.J. Sabin, G. Winther and D. Juul Jensen: *Orientation relationships between recrystallization nuclei at triple junctions and deformed structures* (Acta Mat. Vol. 51 (2003), p. 3999-4011)

[2] H. Hu: *Recovery and recrystallization in Metals* (Interscience, New York (1963), p. 311)

[3] H.F. Poulsen, E.M. Lauridsen, S. Schmidt, L. Margulies and J.H. Driver: *3D-characterisation of microstructure evolution during annealing of a aluminum single crystal of the S-orientation* (Acta Mat. Vol. 51 (2003), p. 2517-2529)

[4] R.A. Vandermeer and P. Gordon: *Edge-nucleated, growth controlled recrystallization in aluminum* (Met. Trans. Vol. 215 (1957), p. 577-588)

[5] H.F. Poulsen and D. Juul Jensen: *From 2D to 3D microtexture investigations,* 13. International conference on textures of materials (ICOTOM 13), Seoul (KR), 26-30 August 2002.
(*Mat. Sci. Forum* 408-412 (2002), p. 49-66)

[6] M. Holscher, D. Raabe and K. Lucke: *Relation between rolling textures and shear textures in fcc and bcc metals* (Acta Metall. Mater. Vol. 42:3 (1994), p. 879-886)

[7] A.W. Larsen: *'Logitech PM5D Precision Polishing and Lapping System' user manual* (Risø-I-2051(EN), Risoe National Laboratory, Roskilde, Denmark (2003))

[8] N.C.K. Lassen, D. Juul Jensen and K. Conradsen: *Image-processing procedures for analysis of electron back scattering patterns* (Scanning Microscopy Vol. 6:1 (1992), p. 115-121)

[9] B.L. Adams: *Orientation Imaging Microscopy: Application to measurement of grain boundary structure* (Mat. Sci. Eng. Vol. 166(A):59 (1993), p. 2517-2529)

Trans Tech Publications Ltd

Brandrain 6
CH-8707 Uetikon-Zuerich
Switzerland

Fax: +41 - 1 922 10 33
e-mail: ttp@ttp.net
Web: http://www.ttp.net

Proceedings of IMECE2004
2004 ASME International Mechanical Engineering Congress and RD&D Expo
November 13-19, 2004, Anaheim, California USA

IMECE2004-62435

METAL MICROSTRUCTURES IN FOUR DIMENSIONS

S. F. Nielsen
Materials Research Department,
Risø National Laboratory,
DK4000 Roskilde, Denmark

C. Gundlach
Center for Fundamental Research:
Metal Structures in Four Dimensions,
Risø National Laboratory,
DK4000 Roskilde, Denmark

E. M. Lauridsen,
Center for Fundamental Research:
Metal Structures in Four Dimensions
Risø National Laboratory,
DK4000 Roskilde, Denmark

R.V. Martins
Center for Fundamental Research:
Metal Structures in Four Dimensions
Risø National Laboratory,
DK4000 Roskilde, Denmark

H. F. Poulsen
Center for Fundamental Research:
Metal Structures in Four Dimensions
Risø National Laboratory,
DK4000 Roskilde, Denmark

S. Schmidt
Center for Fundamental Research:
Metal Structures in Four Dimensions,
Risø National Laboratory,
DK4000 Roskilde, Denmark

D. Juul Jensen
Center for Fundamental Research:
Metal Structures in Four Dimensions,
Risø National Laboratory,
DK4000 Roskilde, Denmark

ABSTRACT

By Three Dimensional X-ray Diffraction (3DXRD) microscopy it is possible to characterize microstructures non-destructively in 3 dimensions. The measurements are furthermore typically so fast that dynamics may be monitored in-situ, giving also the 4'th dimension, namely the time. The 3DXRD technique is based on diffraction of high energy x-rays from third generation synchrotron sources. In the present paper the 3DXRD technique is described and it's potentials are illustrated by examples relating to elastic and plastic strains, recovery, recrystallization and grain growth.

INTRODUCTION

Today's techniques for characterization of microstructure are typically either limited to detailed inspections in 2D or to coarse-scale (mm-range) inspections in 3D. For bulk investigations, the 2D techniques can be used only for static characterizations at discrete processing intervals (i.e. *post mortem* analysis) and not for *in-situ* characterization of the dynamics of microstructural development. The coarse-scale techniques, on the other hand, cannot reveal the individual "building blocks" of the microstructure, e.g. grains, dislocation boundaries or recrystallization nuclei, and thus only average characteristics may be derived.

The so-called 3 dimensional X-ray Diffraction (3DXRD) microscope was designed to overcome these limitations. When developing the 3DXRD microscope the specific aims were to achieve

i) non-destructive bulk measurements (3D)
ii) spatial resolution matching typical microstructural scales, i.e. μm scale
iii) measurements fast enough to follow typical dynamical processes in-situ, i.e. second-minutes time resolutions

This was to allow in-situ mapping of bulk microstructures in otherwise opaque materials.

2 THE THREE DIMENSIONAL X-RAY DIFFRACTION MICROSCOPE

The three dimensional X-ray diffraction microscope (3DXRD) is installed at the Materials Science beamline (ID11) at the European Synchrotron Radiation Facility (ESRF) in France. A schematic diagram of the 3DXRD instrument is shown in Fig. 1. The microscope allows two-dimensional focusing of hard X-

rays (50-80keV), by using a bent Si single crystal (a Laue crystal), which besides working as a monochromator acts as a vertical focusing device. In the horizontal direction a graded bent multilayer provides the horizontal focusing [1]. Focal spot sizes are achieved down to $2\times4\mu m^2$ at the sample position and the divergence of the monochromatic beam is approximately 0.1-1mrad. For more technical details see [2] .

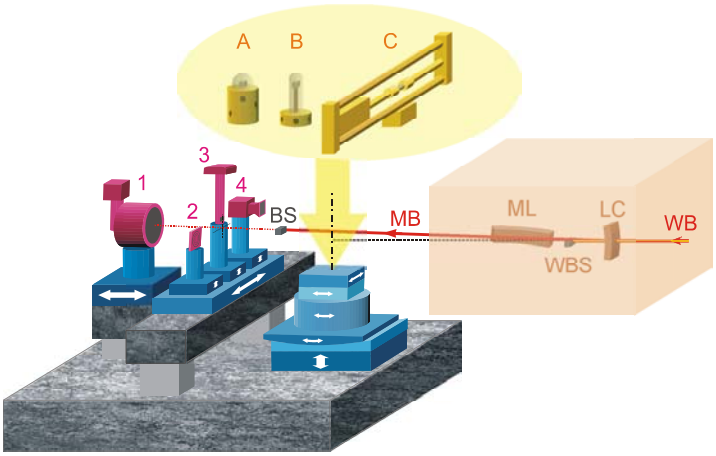

Fig. 1. 3DXRD instrumental schematic. *Optics:* WB: White beam, LC: Bent Laue crystal, ML: Bent multilayer. *Sample environment:* A: Cryostat, B: Furnace, C: 25kN Stress rig. *Detectors and slits:* 1: Large area detector, 2: Conical slit system, 3: High resolution area detector, 4: Optional detector system, BS: Beam stop

The ESRF synchrotron provides a large photon flux of about 10^{11} counts per second. When the energy of the X-ray beam is 80keV the penetration depth is 5 mm in steel and 4 cm in aluminium. The combination of the high photon flux and the high X-ray energy makes the X-ray diffraction microscope ideal for non-destructive characterisation of the microstructure, in the µm-scale range, within the bulk of crystalline materials.

The 3DXRD microscope is a two-axis diffractometer and consists basically of a sample tower and two detector stages. The sample tower can be translated along three axes in an orthogonal co-ordinate system (x,y,z). Above the tower is mounted a rotation unit and a sample stage with an extra set of x and y translations to be used for alignment of the sample. The rotation stage is air driven and has a sphere of confusion of less than 1 µm. The setup makes it possible to rotate and translated the sample with a very high spatial accuracy even with a heavy load on the sample tower. The sample tower is designed to carry loads up to 200 kg making it possible to mount a stress rig or a furnace at the sample position for *in-situ* measurements. Presently a 25 kN Instron tensile rig, a variety of furnaces with maximum temperatures of 1000 °C to 1500 °C, and a cryostat is available at the beamline.

The first of the two detector stages is parallel to the beam direction and holds a large 2D detector – a CCD. The CCD can be positioned in a distance of 0.4-3 m from the specimen. This detector exhibits a high angular resolution needed e.g. for elastic strain measurements. Furthermore, the efficiency is high and the readout fast, making it ideal for dynamic studies (with a time resolution down to 50 ms). The second stage is perpendicular to the beam and currently holds a high resolution 2D detector for 3D spatial mapping and a conical slit cell [3] which is used in conjunction with the large area detector to define a three dimensional gauge volume. This is useful for studies of deformed materials. It is often of interest to combine far field, high resolution angular measurements with near field high spatial resolution. The compound detector stage allows for fast swapping between detectors and optical elements so that a complete sample characterisation can be made with a minimum of dead time.

EXAMPLES OF APPLICATIONS

3,1 Plastic deformation

In-situ measurements of the crystallographic rotations of bulk grains in polycrystalline samples during tensile deformation are reported. The results are compared to standard texture models and it is shown that none of them fits all of the individual grains measured. It is argued that the dataset provides a solid basis for understanding the texture evolution and for development/ evaluation of texture models.

Experimental data on the rotation pathway of individual bulk grains during plastic deformation is critical in guiding current modeling efforts in polycrystalline deformation. Recently we reported on the first such measurements on the rotation of grains embedded in the bulk of an Al polycrystal during tensile deformation [4]. These results on 4 imbedded grains showed that neither the classical Taylor nor Sachs models could adequately account for the observed rotations. In this first experiment, diffraction spots were recorded which originated from grains throughout the entire intersected cross section between the sample and incident beam. It was found that due to broadening of reflections at increasing strain, a maximum cross section of 10 grain lengths was allowable to prevent significant spot overlap at strains approaching 10%. Hence, a significant percentage of the reflections belonged to grains at or close to the surface, which had to be rejected due to their non-representative nature. This restriction also set a lower limit on the grain size, which could be examined.

Here we report on an extension of the above technique, which alleviates these limitations by adding an extra optical element, a conical slit. The conical slit is aligned between the sample and detector and acts to define a gauge volume within the bulk of the sample, which will give rise to diffraction spots on the detector. Diffraction from volumes outside this gauge volume will be rejected by the slit. In this way we can provide a three dimensionally resolved reference volume within the sample and limit the spot overlap problem, which would otherwise be faced when examining thicker or finer grained samples. The conical

slit is used in conjunction with a point-focused beam, which leads to a gauge volume of approximately 5×5×250 μm^3. By assuring that the gauge volume is aligned on the center of rotation, and that the sample is probed far from the surface, we can increase the number of valid grains measured at each position. In this way we can scale up the efficiency of the technique in order to provide the statistics needed for model development.

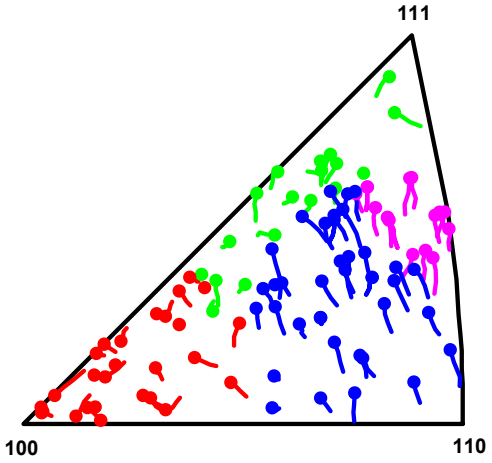

Fig. 2. Stereographic triangle showing the rotation of the tensile axis of individual bulk grains during tensile deformation measured in three experiments on different fcc metals. The circles mark the final orientation of the grains[5].

The data presented here were taken on a sample of 99.5% percent pure Al with a thickness of 4 mm and an average grain size of 75 μm. Data was collected at 0, 2, 4, and 6 % strain. The indexing program GRAINDEX [6] was used to sort the reflections by grain and calculate their orientation. Fig. 2 shows the rotation of the tensile axis for 95 embedded grains measured on a single sample. This analysis resulted in subdivision of the triangle into four different regions, each having a certain main rotation trend:

- Grains in the <110> corner rotate systematically towards the <100>-<111> line
- Grains at the <100>-<111> line rotate along this line towards the <111> corner but with more scatter than observed in the <110> corner
- Grains half way up the <110>-<111> line rotate directly towards the <111> corner without much scatter
- Grains in the <100> corner of the triangle rotate in an apparently random manner

It is therefore concluded that at least at low strains, the rotations are dominated by the lattice orientation and not by grain interaction. Grain interaction may, however, be the origin of the smaller variations found within each of these regions. These results represent the first experimental data containing both sufficient detail and statistics to distinguish between the existing plasticity models.

3.2 Internal strains

3DXRD offers the possibility of measuring internal strains in a set of single grains in the bulk of polycrystalline samples. For each grain and each strain tensor component, the average response of the grain is determined. Once, the strain tensor is known, the stress tensor can be derived from Hooke's law.

The data analysis procedure is as follows. Initially, the diffraction spots observed are sorted with respect to grain of origin by the multi-grain indexing program GRAINDEX [6]. Next, for each grain and each reflection, the lattice strain is determined based on the shift in average Bragg angle of the corresponding diffraction spot. Provided a sufficient number of reflections is measured for each grain (ideally >10) the strain tensor components are determined from a fit to the lattice strains.

This approach is presented and verified in [7]. The strain components of a single embedded Cu grain are determined as function of tensile deformation. The uncertainty in the strain determination is found to be 1×10^{-4}. Recently, Martins and co-workers have reported on an extended study of this type involving tensile deformation of Al up to 2.1% elongation. In this case, the positions, orientations and all strain components were characterised *in-situ* for a large number of grains simultaneously [8]. An example of the results is shown in Fig. 3.

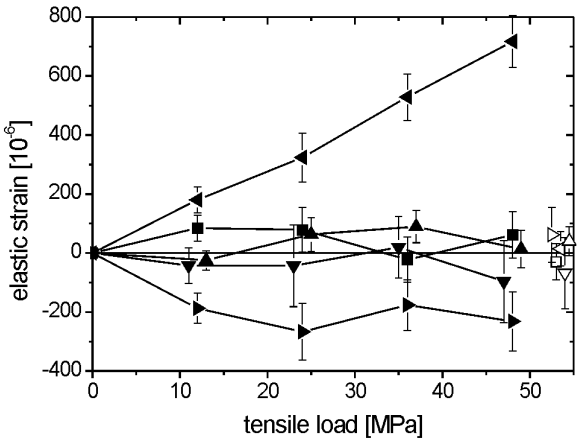

Fig. 3 Strain evolution in one grain as function of load for the components ε_{12} (■),ε_{22} (◀),ε_{13} (▼),ε_{23} (▲) and ε_{33} (▶). Unfilled symbols relate to the strain state after final unloading. A slight scatter along the abscissa is imposed to enhance the visibility of the error bars. From [8].

The only error sources associated with this strain characterization procedure are the experimental inaccuracy in Bragg angle and the provision of a strain-free reference material. The accuracy can be increased substantially by positioning the area detector at a larger distance from the

sample. This has been done by Lienert and co-workers in experiments at APS, where lattice strains were measured with an accuracy of 1×10^{-5} [9].

3.3 Plastic strain

If a material contains second phase particles, they can be used to determine the local strain when the material deformed.

X-ray absorption microtomography can be used to detect marker particle displacements inside a metallic material that undergoes plastic deformation. The displacements of marker particles as a function of externally imposed strain are then used to deduce the internal strain in local regions, which is expected to differ from the externally imposed strain as a consequence of various material factors.

Tomographic data were acquired at the dedicated microtomography instrument at beamline BW2 at HASYLAB, for an aluminium sample containing W marker particles. The sample was made by compacting a mixture of Al and W powder to a 100% dense material. Only 1vol% W powder was used in the mixture and the average particle diameter in the two powders were 7 µm.

The sample was deformed in stepwise compression, with data for a tomographic reconstruction being acquired after each deformation step. After a series of image analysis steps to identify the centre of mass of individual particles and aligning the successive tomographic reconstructions, the displacements of individual particles could be tracked as a function of external strain. Fig. 4 shows the resulting displacement map.

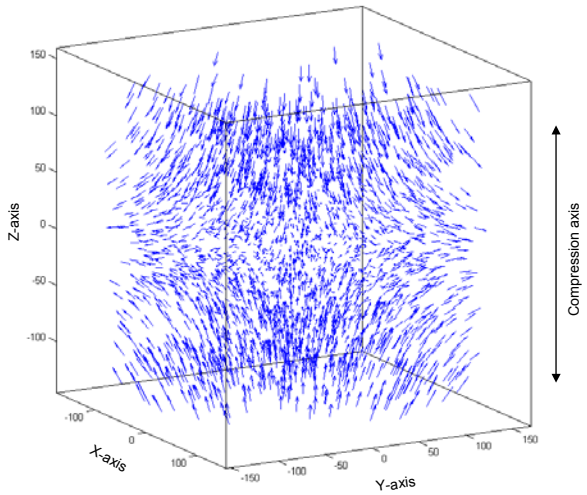

Fig. 4. The vector displacement tracks of 2544 particles within a 0.4 mm cube inside the sample. The numbers on the axes are in units of pixels of 1.5µm. From [10].

The particle displacements can be used to identify the local displacement gradient components, from which the local 3D plastic strain tensor can be determined. This allows us, to map the strain components as a function of location inside a deforming metallic solid. For more details about this experiment see [10]. For the described experimental conditions the strain resolution is 10^{-2} on the measurements of displacement gradient components.

3.4 Recovery

During plastic deformation of metals metastable dislocation structures form with dislocation boundaries separating nearly dislocation free regions. During subsequent annealing, the structure may undergo recovery.

Here a method is presented that enables studies of the individual *embedded* cells during recovery. The method is an extension of the technique described in section 3.5.2.

An *in-situ* recovery experiment has been performed on a disc of 38% cold-rolled aluminium. Growth curves are derived for 9 cells during annealing at 300 °C. The study partly proves the feasibility, partly provides first results on the microstructural dynamics during recovery [11].

The x-ray beam from the synchrotron was monochromatised to 50 keV and focused horizontally and vertically and defined by a set of slits to a Gaussian shaped spot with a full width half maximum of 7 µm.

The measuring scheme was as follows: exposures were made at five rotations ω of the sample, namely –2°, -1°, 0°, 1° and 2°. During each exposure the specimen was oscillated by ±0.5°. This ω-scanning was repeated at nine positions of a 3×3 (y,z)-grid, with a distance between the nodes in the grid of 5 µm.

The sample was then heated from room temperature to 300 °C in 3 minutes. During the following 181 minutes the temperature was kept constant while continuously repeating the (y,z,ω) grid measurements every 5 minutes. Between each of the 5-minute-sets of observation the sample position was rechecked against the markers.

For each non-overlapping diffraction spot and each ω-position, the integrated intensity of the spot at the nine grid points was determined. A least-square fit was performed to these data, assuming a Gaussian beam profile. The parameters fitted were the center-of-mass (CMS) position of the associated subgrain and a position-independent integrated intensity.

The integrated intensity of the diffraction spot is proportional to the volume of the associated coherently diffracting domain – the cell (kinematical scattering). We succeeded in getting results for the dynamics of nine individual cells, six of those are present in Fig. 5.

The evolution in the (true) size is shown in Fig. 5. Among the cells, more than half exhibit essentially no growth, two shrink during the first hour and then stay constant, one grows rapidly during the first 5 minutes then stagnates, while the last one first grows, then shrinks. In general, the curves exhibit a smooth evolution. Strikingly, there is no obvious correlation between subgrain volume and growth behaviour. The smallest subgrain grows substantially during the first 5 minutes. So does the rather large subgrain. On the other hand, one of the larger subgrains shrinks during the observation and the largest one does not change in size at all. This behaviour is in marked

contrast with elementary theories of curvature (i.e. interfacial energy) driven coarsening [12], where cells larger than average are expected to grow while cells smaller then average are expected to shrink. However, this behaviour might be strongly affected by the local neighbourhood of the individual cells. From the small number of observed cells it cannot be excluded, that a curvature driven model is valid in a statistical sense. Analysis of a larger number of cells is required for resolving this issue.

- A unique diffraction technique has been established, enabling in-situ studies of the dynamics of the individual subgrains during recovery.
- The growth curves for the individual subgrains are different from the average behaviour for a sub-grain of a given size as predicted by deterministic models based on interfacial energy driven mechanisms.

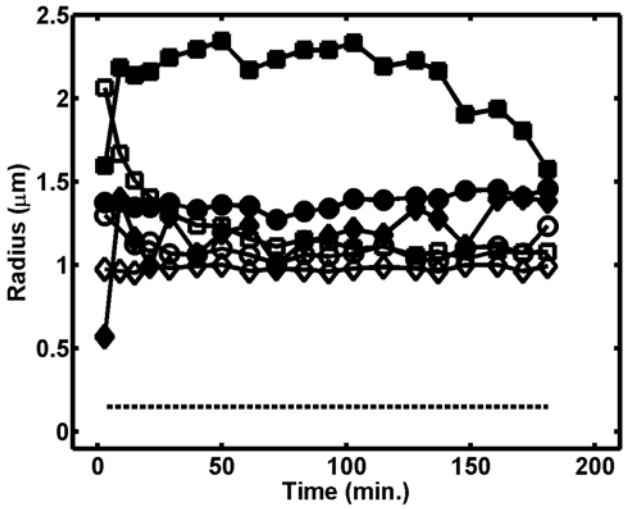

Fig. 5. The evolution in size of 6 individual cells. The equivalent sphere radius is shown as a function of annealing time. The detection limit of 150 nm is marked as a dashed line.

3.5 Recrystallization

Recryslallization is generally separated into two distinct processes: nucleation and growth. During nucleation, almost defect-free nuclei form in the deformed microstructure. During growth, these nuclei grow by boundary migration through the deformed microstructure. The recrystallization process is completed when the entire deformed matrix is replaced by a new grain structure.

Three types of 3DXRD recrystallization measurements are presented, these relates to in-situ studies of i) nucleation, ii) growth kinetics of individual grains and iii)'filming' the growth of interior recrystallizing grains while they grow. All the three types of experiments have lead to results contradicting standard textbook knowledge.

3.5.1 Nucleation

The ideal experiment studying nucleation would be to characterize in detail in 3D the deformation microstructure including orientations. Then anneal the sample *in-situ* to the beginning of nucleation and see where and with what orientations the nuclei develop.

This is possible by 3DXRD for selected samples and nucleation conditions. As examples nucleation in a 65% deformed Al single crystal and in a 20% deformed Cu polykrystal have been studied [13, 14]. In both examples it was found that the nuclei do not necessarily have orientations as the parent deformation microstructures. This result contradicts today's most widely applied nucleation models.

3.5.2 Growth kinetics of individual grains

The 3DXRD microscope can also be used for in-situ investigations of the recrystallization kinetics of a large number of individual grains [15]. Compared to other experimental set-up presented in this paper the experimental set-up for measuring individual growth curves during recrystallization is relatively simple. The high-energy x-ray beam is focused to a box-shaped beam profile with dimensions typically of the order of 3 times the average grains size. This box-shaped beam will illuminate a channel trough the sample where illuminated grains fulfilling the scattering conditions will give rise to diffraction spots. These diffraction spots are recorded on a 2-dimensional detector, which allows for fast data acquisition. The sample of interest is placed inside an x-ray transparent furnace and mounted on a rotation stage. During the in-situ annealing experiment the integrated intensity of the diffraction spots is collected by acquiring images while rotating around the vertical axis. This way typical time resolutions in the order of seconds is obtained.

Monitoring the intensity evolution of the individual diffraction spots, and utilising the fact that the integrated intensity of a diffraction spot is directly proportional to the volume of the diffracting grain, enables detailed growth curves of several hundreds of nuclei/grains to be monitored simultaneously - from the moment they nucleate to they reach their final grain size.

Fig. 6 shows examples of growth curves obtained using this technique with a 90% cold-rolled commercial AA1050 aluminium alloy, which was annealed in-situ at 270°C [16]. As can be seen from the growth curves there is a large variation in growth behaviour for the individual grains. From the growth curves critical recrystallization parameters such as nucleation times, growth rates and 3-dimensional grain sizes is easily derived. As an example the distribution of nucleation times for 244 grains is also shown in Fig. 6. As the technique is diffraction based the crystallographic orientation of the grains can also be determined using the indexing software GRAINDEX [6]. Hence, the parameters describing the recrystallization kinetics can be correlated with

crystallographic information to further elucidate the recrystallization process.
The described technique is not limited to recrystallization studies but applies to all nucleation and growth processes, and has as such been successfully applied to studies of phase-transformations in steel [17].

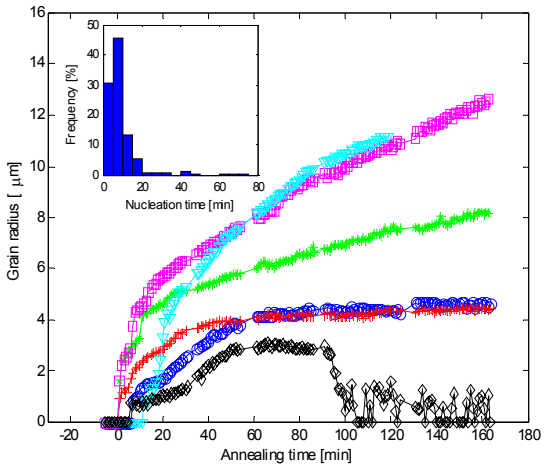

Fig. 6. Examples of data obtained from in-situ 3dxrd recrystallization experiments on a 90% cold rolled commercial aluminium alloy. The figure shows a selection of growth curves of individual grains illustrating the variation of growth kinetics observed (from ref [15]). The insert shows the distribution of nucleation times derived from a total of 244 individual growth curves from the same alloy (from ref [16]).

3.5.3 "Filming" the growth

As mentioned earlier the 3DXRD microscope facilitates observations of structural changes in the bulk of materials non-destructively. Recently, individual shapes of recrystallizing grains have been observed as function of annealing time in the bulk of deformed Al single crystals [18]. An example is shown in Fig. 7. A planar beam shape with dimensions 5 µm vertically and 600 µm horizontally was used to record a "snapshot", i.e. a stack of cross sections constituting the full three dimensional shape of the individual recrystallizing grain. By repeating this procedure during an annealing period a four dimensional measurement, i.e. three spatial dimensions and one time dimension, of the recrystallizing grain was obtained. All the grains measured so far exhibited irregular movements contradicting the assumption of smooth growth in the classical models of recrystallization. The information content provided in this new type of measurements makes it possible to probe the mechanisms of recrystallization *locally* since the position of individual grain boundary segments are known along with the crystallographic orientation of the recrystallzing grain as well as the structure of the surrounding deformed microstructure.

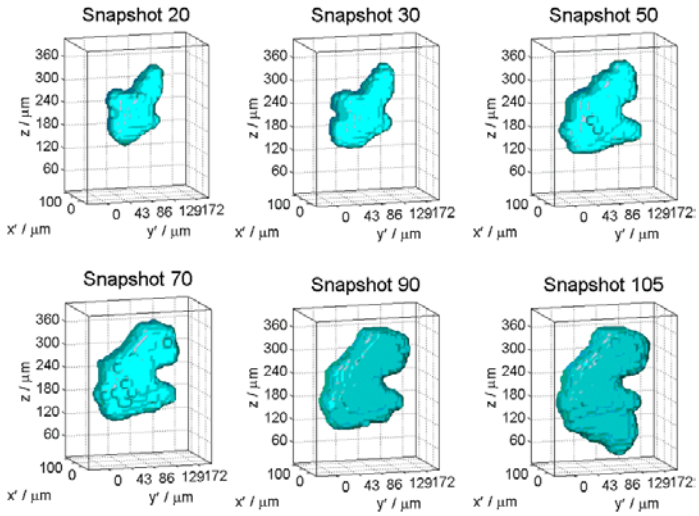

Fig. 7. Storyboard consisting of six "snapshots" of a recrystallizing surface grain in a 42% cold rolled Goss oriented aluminium single crystal. The axes x' and y' denote the directions along and transverse to the beam direction, respectively. The annealing temperatures were in the range 270 °C to 320 °C. The recording time per "snapshot" was 10 minutes.

4 CONCLUDING REMARKS

The 3D X-ray diffraction microscope has already proven to be a powerful tool in many fields of materials science. Measurements performed by 3DXRD have shown that the local environment and local microstructural inhomogeneities often are extremely important. These effects cannot be predicted by classical models, which have been developed considering average properties.
Besides the types of investigations presented here the method applies to polycryslalline research in general, including studies of e.g. ceramics, composites, rocks, ice and drugs. The 3DXRD microscope is available to external scientists upon application following the standad review procedure for granting beam time at ESRF. Information on this can be found on the web-sites: www.esrf.fr and www.risoe.dk/afm/synch.

REFERENCES

1 U. Lienert, C. Schulze, V. Honkimaki, T. Tschentscher, S. Garbe, O. Hignette, A. Horswell, M. Lingham, H.F. Poulsen, N.B. Thomsen and E. Ziegler. *J. Synchrotron Rad.* **5** (1998) 226.

2 U. Lienert, H.F. Poulsen, V. Honkimaki, C. Schulze and O. Hignette, *J. Synchrotron Rad.* **6** (1999) 979.

3 S.F. Nielsen, A. Wolf, H.F. Poulsen, M. Ohler, U. Lienert and R.A. Owen. *J. Synchrotron Rad.* **7** (2000) 103.

4 L. Margulies, G. Winther, H.F. Poulsen. *Science*, **291** (2001) 2392.

5 H.F. Poulsen, L. Margulies, S. Schmidt, G. Winther, *Acta Mater.* **51** (2003) 3821.

6 E.M. Lauridsen, S. Schmidt, R.M. Suter, and H.F. Poulsen. *J. Appl. Cryst*. **34** (2001) 744.

7 L. Margulies, T. Lorentzen, H.F. Poulsen and T. Leffers. *Acta Mater.* **50** (2002) 1771.

8 R.V. Martins, L. Margulies, S. Schmidt, H.F. Poulsen, and T. Leffers (2004). *Mater. Sci. Eng.*, in press.

9 U. Lienert, J. Almer, P.R. Dawson, T.-S. Han, T. Leffers, L. Margulies, S.F. Nielsen, H.F. Poulsen, and S. Schmidt. *Acta Mater.* **52** (2004) 4461.

10 S.F. Nielsen, H.F. Poulsen, F. Beckmann, C. Thorning, J.A. Wert. *Acta. Mater.* **51** (2002) 2407.

11 C. Gundlach, W. Pantleon, E.M. Lauridsen, L. Margulies, R.D. Doherty, H.F. Poulsen, *Scripta mater.* Vol. **50** (2004) 477.

12 F.J. Humphreys, M. Hatherley. Recrystallization and Related Annealing Phenomena. New York: Pergamon Press;1995.

13 H.F. Poulsen, E.M. Lauridsen, S. Schmidt, L. Margulies and J.H. Driver. *Acta Mat.* **51** (2003) 2517.

14 A.W. Larsen, C. Gundlach, H.F. Poulsen, L. Margulies, Q. Xing, and D. Juul Jensen. In 2. International conference on recrystallization and grain growth, Annecy, France, 2004. Trans Tech Publications Ltd.

15 E.M. Lauridsen. D. Juul Jensen, H.F. Poulsen, U. Lienert. *Scripta mater.* **43** (2000) 561.

16 E.M. Lauridsen, H.F. Poulsen, S.F. Nielsen, and D. Juul Jensen. *Acta mater*. **51** (2003) 4423.

17 S.E. Offerman, N.H. Van Dijk, J. Sietsma, S. Grigull, E.M. Lauridsen, L. Margulies, H.F. Poulsen, M.T. Rekveldt, and S. Van der Zwaag. *Science* **298** (2002) 1003.

18 S. Schmidt, S.F. Nielsen, C. Gundlach, L. Margulies, X. Huang and D. Juul Jensen. *Science* **305** (2004) 229.

Image analysis for X-ray studies of the dynamics of individual embedded subgrains during recovery

C. Gundlach[1], S. Schmidt[1], L. Margulies[1,2], T. Knudsen[1], W. Pantleon[1] and H. F. Poulsen*[1]

An advanced image analysis algorithm is presented for extracting growth curves for individual embedded subgrains during static recovery of deformed metals. The data are obtained by three dimensional X-ray diffraction microscopy. Based on a 5D multicomponent labelling scheme embedded in the full five dimensional experimental space, the algorithm is much faster and less biased than one previously used for the same purpose. The use of the methodology is demonstrated on a study of static recovery in an AA1200 specimen cold rolled to a true strain of 2.

Keywords: Recovery, X-ray diffraction, Synchrotron radiation, 3DXRD, Image analysis

Introduction

Traditionally static recovery has been studied in several ways.[1] One method is by use of bulk probes, and includes calorimetry, conductivity and hardness measurements. The results represent an average over all processes and over the heterogeneity of the specimen. A second method uses electron microscopy on the surface of sectioned samples, both before and after annealing.[1–3] While a wealth of detailed information is acquired, the dynamics of the microstructure can only be probed statistically in this manner. (*In situ* electron microscopy studies have been reported by several groups, but are generally not considered as being representative of bulk behaviour for geometric reasons.)

Recently, an X-ray diffraction method has been introduced, which enables direct observation of the dynamics of individual embedded subgrains during annealing.[4] The method is an extension of three dimensional X-ray diffraction (3DXRD)[5,6] conventionally used for structural characterisation of grains within millimetre to centimetre thick polycrystals. By focusing the X-ray beam from a synchrotron source to dimensions of about 5×5 μm and by using foils, diffraction spots arising from individual subgrains were monitored as function of annealing time. As a result growth curves – representing the change in volume – have been determined for nine subgrains simultaneously.[4]

As reported, this method is, however, limited by overlap of the diffraction spots. Due to the requirement for having a ratio of foil thickness to subgrain diameter of 10 or more (to ensure that the dynamics of the subgrains in the centre of the foil can be considered as bulk) many hundreds or thousands of subgrains are illuminated simultaneously. This implies that the probability of overlapping diffraction spots on the detector becomes large. As a result, grain statistics are poor and there is a danger that the method is biased, in the sense that the probed subgrains are special. This problem is accentuated by the fact that many spots, which look clearly 'distinct' to the eye, cannot be resolved by the image analysis applied.

In this paper a superior image analysis technique is presented whereby the number of 'visible' spots is much improved. The algorithm developed is based on two underlying concepts. First, to perform the image analysis in the five dimensional space spanned by all experimental dimensions including time. Second, to separate close lying neighbours in this space by a combination of an extension of the classical 'labelling of components scheme' from 2D,[7] with a multicomponent fitting to the known spatial variation of the X-ray beam.

In the following the 5D data analysis methodology is described in detail, and its use is demonstrated for characterising the recovery of a cold rolled AA1200 foil.

Experimental

The sample material used was AA1200, with an original grain size of 75 μm, which had been cold rolled to a true strain of 2 prior to the annealing experiment. The deformation induced microstructure in this material has been extensively characterised by TEM after cold rolling[8] and subsequent annealing.[9] The average size of the subgrains in the deformed state was found to be 1 μm along the rolling direction and 0·43 μm along the normal direction. A foil of the deformed material was prepared and inserted by means of a special specimen

[1]Center for Fundamental Research: Metal Structures in 4 Dimensions, Materials Research Department, Risoe National Laboratory, 4000 Roskilde, Denmark
[2]European Synchrotron Radiation Facility, BP 220, 38046 Grenoble, France

*Corresponding author, email henning.friis.poulsen@risoe.dk

Published by Maney on behalf of the Institute
Received 24 August 2005; accepted 19 September 2005
DOI 10.1179/174328405X71675

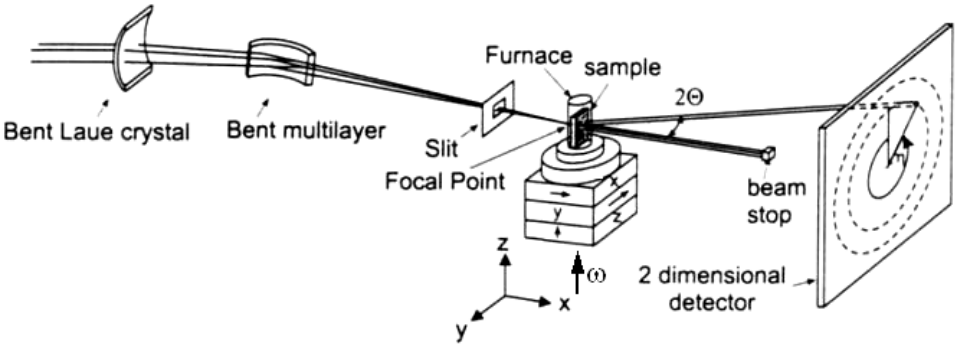

1 Sketch of experimental setup. Laboratory coordinate system (*x*,*y*,*z*) and the diffraction angle 2θ, the angle η on the detector and the rotation angle ω around the z axis are defined

holder in a small evacuated furnace for *in situ* 3DXRD investigations following the procedures described earlier.[4]

The experiment was performed using the dedicated 3DXRD microscope[5] at beam line ID-11 at the European Synchrotron Radiation Facility. A monochromatic 50 keV X-ray beam was focused to a spot with a size as small as possible with the microscope at the time of the experiment. The resulting beam profile was carefully measured and found to be approximately Gaussian with a full width at half maximum (FWHM) of 5·7 μm and 5·7 μm in horizontal and vertical directions, respectively. The foil was positioned at the focal spot and exposures were acquired with a two dimensional detector while rotating the sample around the ω axis. (This and other experimental parameters are defined in the sketch shown in Fig. 1.) The detector, a 14-bit FRELON CCD coupled to an image intensifier, was positioned at a distance of 0·32 m from the sample, such that the first five Debye–Scherrer rings were fully visible. The η-resolution was about 0·2° (η is the azimuthal angle, see Fig. 1). Based on scaling arguments,[6] a reference of known thickness and the integrated intensity in the diffraction pattern, the foil thickness was estimated to be 3 μm.

The sample was subjected to isochronal annealing. Starting at 200°C, the temperature was increased in steps of 8 K to a final temperature of 374°C. At each temperature, the following measuring scheme was applied: exposures were made at 31 equidistant ω positions, spanning 6°. During each exposure the sample was oscillated by $\pm$0·1°. This ω scanning was repeated at 16 positions in a spatial 4×4 (y,z) grid, with a distance of 4 μm between the nodes of the grid. An example of the raw data from one exposure is shown in Fig. 2. The holding time at each temperature step was 15 min. Potential positional drifts during the heat treatment were excluded by regular tests of the position of reference points.[4]

Algorithm

The aim of the data analysis is

(i) to identify which parts of the diffraction patterns (which spots) originate from a single subgrain
(ii) to find the position of the subgrain by fitting the intensity distribution in the 4×4 (y,z) grid to the known beam profile
(iii) based on the above to determine the integrated intensity of the entire reflection.

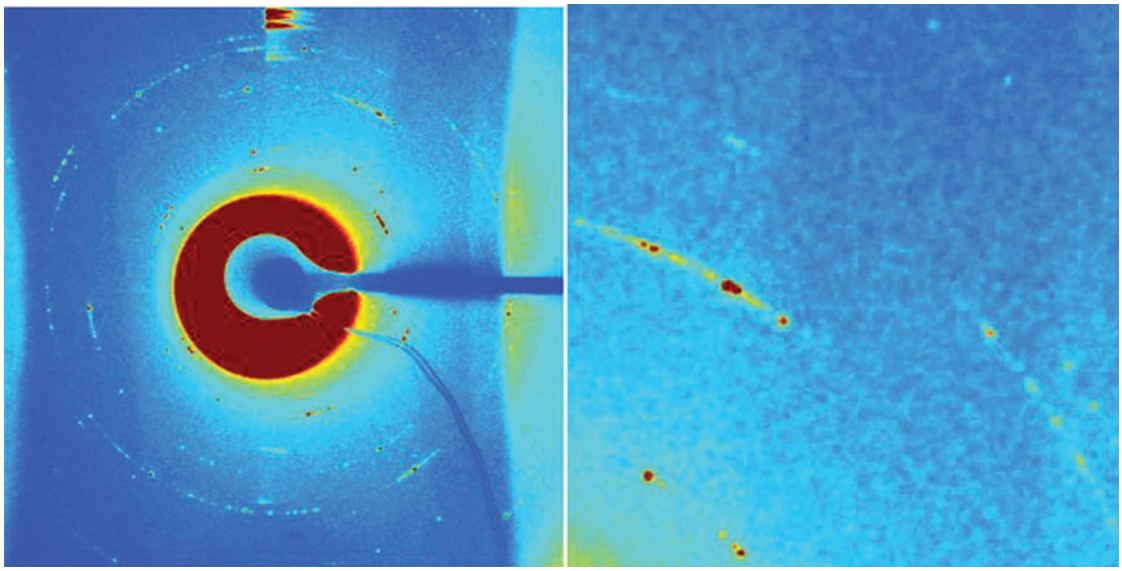

2 Example of raw data for one particular exposure acquired at 200°C. Left: full image. Enhanced intensity close to the centre of the image is an experimental artefact due to lack of screening of background. Right: Zoom of same image. Diffraction pattern comprises distinct but close lying and at times overlapping diffraction spots

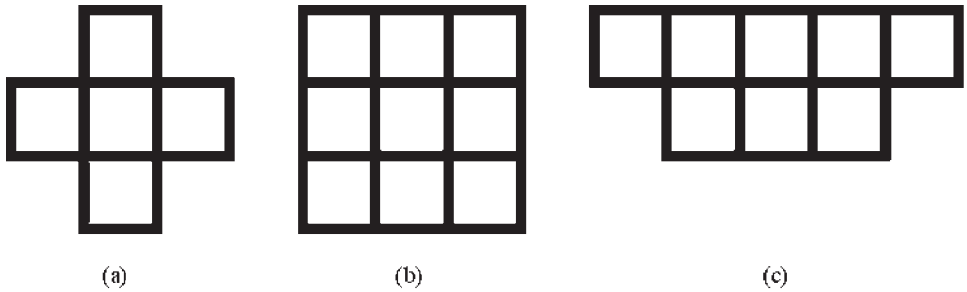

3 Illustration of connectivity rules used for blob identification: (*a*) 4-connectivity, (*b*) 8-connectivity, and (*c*) special connectivity rule designed for (ω, t) plane

After correction for structure and Lorentz factor, the intensity is directly proportional to the volume of the associated subgrain, with a constant of proportionality that is easily determined by calibration.[6]

The straightforward approach[4] published earlier is sequential. First, spots are separated based on raw images, then their (y,z) position and integrated intensity is fitted simultaneously to a single Gaussian distribution and finally their intensities are monitored as function of time. It is found that this approach gives rise to artefacts unless one puts quite conservative constraints on the proximity of spots in the raw images.

The revised algorithm is not sequential but based on image analysis in the 5D experimental space parameterised by (η, ω, y, z, t). This space is large, with $900 \times 31 \times 4 \times 4 \times 23 \approx 10^8$ volume elements (voxels). The algorithm comprises two steps.

Blob finding in 5D space

A 5D array T of intensities is generated based on the background subtracted raw data, corrected for two crystallographic factors: the structure and Lorentz factors. By defining a threshold a binary array T_{bin} is created. This global threshold value is the only adjustable parameter in the algorithm and is set by an analysis of the background. First, the background and its dependence on the position on the detector is determined as a median value from all images in a measuring cycle and subtracted from each image. The threshold is defined as five times the standard deviation of the statistical fluctuations in the remaining background signal.

Next, connected parts – in the following called 'blobs' – in T_{bin} are determined by extending the two pass labelling algorithm[7] to 5D. The nature of connectivity in the various dimensions can be adjusted to the problem at hand. Usually, 4- or 8-connectivity is used in blob finding algorithms in 2D. As illustrated in Fig. 3*a*, 4-connectivity implies that each pixel in the blob is associated with at least one neighbouring pixel, positioned to the north (N), south (S), west (W) or east (E), which are also included in the blob. In the case of 8-connectivity, there should be at least one neighbour within the blob in either N, NW, W, SW, S, SE, E, or NE direction, as shown in Fig. 3*b*. Applying this terminology to all pairs of dimensions in the list (η, ω, y, z, t), we find the following settings to be superior:

As default all 2D planes are 4-connected.

The (η, ω) plane is 8-connected, as the mosaic spread of a given spot may be anisotropic with an arbitrary direction.

The (ω, t)-plane is special. A pixel at (ω, t) is connected to any of the 5 pixels ($\omega-2\Delta\omega$, $t-\Delta t$), ($\omega-\Delta\omega$, $t-\Delta t$), (ω, $t-\Delta t$), ($\omega+\Delta\omega$, $t-\Delta t$), ($\omega+2\Delta\omega$, $t-\Delta t$) as well as ($\omega-\Delta\omega$, t) and ($\omega+\Delta\omega$, t). This rule is designed specifically for this type of experiment. Apparently, the aluminium foil bends slightly during annealing causing a shift in ω of the observed spots. This shift is compensated by the suggested relaxed connectivity rule. Note, that no forward connectivity in the time coordinate is allowed.

Blobs extending to the ω or η borders of the 5D space are excluded as the integrated intensity may not have been measured fully. (In principle the distribution is continuous in η. However, for numerical reasons, the full 5D volume for a given Debye–Scherrer ring is divided into subvolumes corresponding to η intervals of 20°, which are analysed separately.)

Multicomponent fitting

The remainder of the analysis is performed blob by blob. For each blob the intensity distribution in the corresponding part of T is projected onto the (y,z,t) subspace. Within this subspace, for each time step a multicomponent Gaussian least squares fit is made to the (y,z) distribution. All Gaussians have fixed FWHMs given by the beam size.

The number of Gaussian distributions considered in the multicomponent fitting was determined by the number of local maxima in the spatial 4×4 grid. The grid positions of the local maxima were chosen as initial values in the multicomponent fit. The fit is accepted

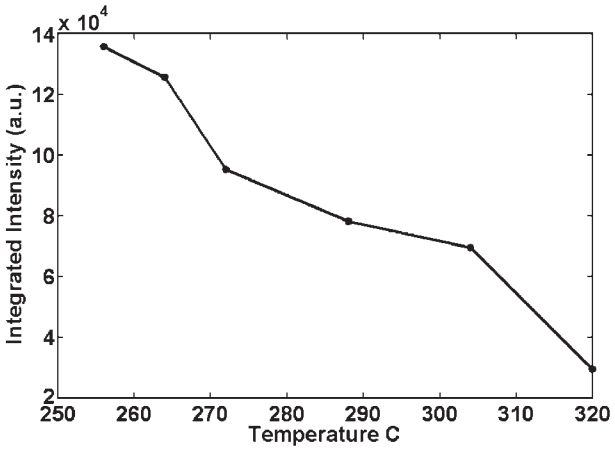

4 Evolution of single individual subgrains during isochronal annealing. Decreasing integrated intensity as a function of successively increasing annealing temperature corresponds to shrinkage of the subgrain

based on conventional criteria for convergence and the norm of the residual. Peaks with a maximum outside of an inner rim of 2 μm from the borders in y and z are excluded as it is deemed impossible to determine their position – and thereby the integrated intensity – with sufficient accuracy.

This procedure is repeated for each time step. If a valid peak is found at the 'same' (y,z) position – within an error of 2 μm – and over at least five contiguous time steps, the evolution in integrated intensity of this peak is identified as a valid growth curve. (The slight lateral motion of the blob was caused by the furnace sample system not being in thermal equilibrium during heating. The position of markers has been monitored repeatedly and thermal equilibrium was assumed when the same position was detected twice. Apparently, this was not sufficient and relaxation in the furnace sample systems has caused further lateral displacements during the measurement.)

The motivation for the multicomponent fit was to remove outliers. By trial and error it was found that (typically low intensity) tails from neighbouring spots disrupt a fit to a single Gaussian distribution. Hence, the typical final result of the fitting procedure is either none or one valid growth curve per blob, but in certain cases several growth curves are identified.

This second part of the algorithm has essentially two types of adjustable parameters, namely the convergence parameters for the fit and the allowed 'wiggle' of the position of the peak.

The algorithm as presented was implemented in MATLAB.

An example of a resulting growth curve is provided in Fig. 4 showing a shrinking subgrain. Scaling the required processing time for a subset of the data, performing a complete data analysis of all data with parameters as defined above is estimated to last about one week.

Discussion

The prospect of measuring an ensemble of growth curves of individual elements within a local bulk region of a deformed microstructure should be emphasised. Relevant research topics include.

1. Characterisation of the variation in growth behaviour as function of position or orientation.
2. Determination of kinetics and activation energies for recovery.
3. Tests of coarsening models for recovery.

It should also be noted that synchrotron beam lines are under development, with the aim of providing hard X-ray beams with a spot size of the order 100 nm. With such beams it is expected that it will be possible to characterise the stability of a diversity of nanostructures in an analogous manner to the analysis of subgrains in deformation structures on a micrometre scale, as outlined here.

It may be argued that the ultimate image analysis tool for the problem discussed in this article would be to find blobs in 5D space using a watershed algorithm. However, we estimate such methods would be prohibitively slow numerically and furthermore argue that threshold based segmentation plus multicomponent fitting is a good – and much faster – approximation to the watershed algorithm in this case.

Acknowledgments

The authors thank J. R. Bowen and N. Hansen for scientific discussions, V. Honkimäki for use of software, Q. Xing for sample preparation, and ESRF for provision of beam time. This work was supported by the Danish National Research Foundation and by the Danish Research Council SNF (via Dansync).

References

1. F. J. Humphreys and M. Hatherley: 'Recrystallization and related annealing phenomena'; 1995, Oxford, Pergamon.
2. P. Faivre and R. D. Doherty: *J. Mater. Sci.*, 1979, **14**, 897–919.
3. A. Godfrey, D. Juul Jensen and N. Hansen: *Acta Mater.*, 2001, **49**, 2429–2440.
4. C. Gundlach, W. Pantleon, E. M. Lauridsen, L. Margulies, R. D. Doherty and H. F. Poulsen: *Scr. Mater.*, 2004, **50**, 477–481.
5. H. F. Poulsen: 'Three-dimensional X-ray diffraction'; 2004, Berlin, Springer.
6. E. M. Lauridsen, D. Juul Jensen, H. F. Poulsen and U. Lienert: *Scr. Mater.*, 2000, **43**, 561–566.
7. H. Bässmann and Ph. W. Besslich: 'Bildverarbeitung ad oculos'; 1991, Berlin, Springer.
8. Q. Liu, X. Huang, D. J. Lloyd and N. Hansen: *Acta Mater.*, 2002, **50**, 3789–3802.
9. Q. Xing, X. Huang and N. Hansen: *Mater. Sci. Forum*, 2004, **467–470**, 209–214.

Available online at www.sciencedirect.com
SCIENCE DIRECT®
Scripta Materialia 53 (2005) 553–557
Scripta MATERIALIA
www.actamat-journals.com

Nucleation of recrystallization observed in situ in the bulk of a deformed metal

Axel W. Larsen [a], Henning F. Poulsen [a], Lawrence Margulies [a,b], Carsten Gundlach [a], Qingfeng Xing [a], Xiaoxu Huang [a], Dorte Juul Jensen [a,*]

[a] *Center for Fundamental Research: Metal Structures in Four Dimensions, Risø National Laboratory, P.O. Box 49, Building 228, Frederiksborgvej 399, DK-4000 Roskilde, Denmark*
[b] *European Synchrotron Radiation Facility, BP 220, F-38043 Grenoble, France*

Received 31 January 2005; received in revised form 18 April 2005; accepted 22 April 2005
Available online 8 June 2005

Abstract

Nucleation of recrystallization is studied in situ in the bulk by three-dimensional X-ray diffraction. Copper samples cold rolled 20% are investigated. The crystallographic orientations near triple junction lines are characterized before, during and after annealing. Three nuclei are identified and it is shown that two nuclei are twin related to their parent grain and one nucleus has an orientation, which is neither present in the deformed parent grains nor first order twin related to any of them. Data on the nucleation kinetics is also presented.

Keywords: Nucleation of recrystallization; X-ray diffraction; Copper; Misorientation

1. Introduction

Nucleation is a much debated recrystallization process, whereby upon annealing nearly perfect nuclei form in a deformed material [1]. One reason for the debate is that it has been impossible to follow experimentally the nucleation process in situ, except at a sample surface.

It is characteristic of previous studies of nucleation, that these have been performed either on the surface of samples, which is not necessarily representative of the bulk of the sample, or have been statistical in nature. In the latter case, the bulk microstructure is characterized in deformed and annealed samples separately. It is therefore not possible to relate directly a nucleus to the specific deformation microstructure at the exact site where it formed. This "loss of evidence" [2] is important, as detailed quantitative analysis by electron microscopy has revealed that the deformed microstructure in metals is heavily subdivided into small, typically μm-sized volume elements of different crystallographic orientations [3]. Furthermore, the orientation of the original grain in a polycrystalline sample affects its subdivision, leading to heterogeneous deformation microstructures [4,5].

A currently much debated issue is the possible development of nuclei with new orientations compared to the deformed microstructure. Existing nucleation models such as strain induced boundary migration [6], nucleation in cube bands [7,8], and particle stimulated nucleation [9], all predict that orientation should be conserved. In contrast a number of electron microscopy (EM) investigations suggest that some fraction of the nuclei do appear with new orientations [10–20]. Such "odd nuclei" would have good growth potentials and are thus considered very important in the understanding of the recrystallization microstructures and texture

* Corresponding author. Tel.: +45 46 77 58 04; fax: +45 46 77 57 58.
E-mail address: dorte.juul.jensen@risoe.dk (D.J. Jensen).

1359-6462/$ - see front matter © 2005 Acta Materialia Inc. Published by Elsevier Ltd. All rights reserved.
doi:10.1016/j.scriptamat.2005.04.053

development. However, these EM studies can be questioned. In the case of in situ surface studies, the nucleus might have formed not at the surface characterized, but at a site below it. Also surface effects may lead to atypical types of nucleation. In the case of statistical studies, it is essential to note that nuclei are small as well as rare. To characterize a representative part of the deformed microstructure, it is necessary to measure volume fractions of the order of 10^{-8} or less with a sub-micron spatial resolution. That is not practical with existing EM methods.

These experimental limitations do not apply to three-dimensional X-ray diffraction (3DXRD) microscopy [21]—an emerging method based on the use of high energy X-rays generated by a synchrotron. 3DXRD enables characterization of the individual embedded grains in bulk crystalline samples as well as studies of the dynamics of the grains during processing [22–24]. In a recent publication, a variant of 3DXRD was demonstrated, whereby the microstructure of a channel-die deformed Al single crystal ($\varepsilon = 1.5$) could be characterized with respect to the existence of structural elements with "odd" orientations [25].

In this paper we extend this method to in situ studies of the microstructure evolution during annealing of deformed polycrystals. For the first time, a direct correlation between the orientation of the emerging nuclei and the parent microstructure is obtained in a polycrystalline sample.

2. Experimental

The material of choice is particle-free, 99.995% pure, oxygen-free, high conductivity copper. The initial material was prepared by cold rolling to 20% reduction in thickness and annealing for 8 h at 700 °C to give a microstructure with relatively coarse grains with an average size of 500 μm. This material was further cold-rolled to 20% reduction. The deformed material was characterized by transmission electron microscopy (TEM) using a JEOL-2000FX microscope operated at 200 keV. Similar to previous studies [26] the average distance between dislocation walls exhibiting a misorientation of 1° or more was 1–2 μm, depending on the orientation of the grain.

From this material three 10×10 mm^2 plates were cut, with the plate normal in the TD direction. These samples were thinned from both sides to a final thickness of 0.3 mm, using a Logitech PM5D polishing and lapping machine. Finally, the sample surfaces were electrochemically polished to remove any remnant surface scratches, which might act as unwanted surface nucleation sites.

The surface of each of the three samples (to be referred to as A, B and C) were inspected within a $\sim 1.8 \times 1.8$ mm^2 area by electron back-scattering pattern (EBSP) using a JEOL JSM-840 scanning electron microscope (see Fig. 1).

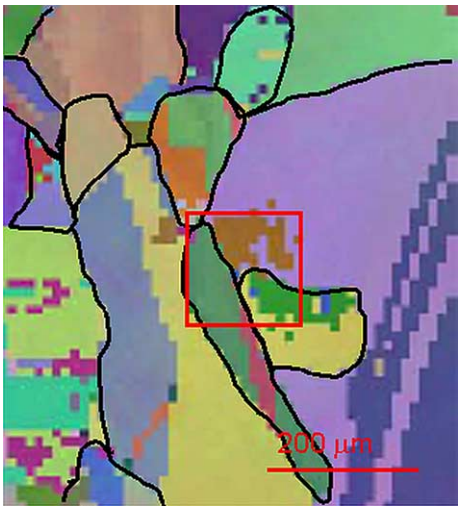

Fig. 1. An EBSP map of the surface of sample B. Deformed grains are outlined by black lines. The red square indicates the 160×160 μm^2 area in the vicinity of a triple junction, which was characterized in the X-ray diffraction study.

The experiment took place at beamline ID11 at ESRF, Grenoble, France. A sketch of the experimental set-up is shown in Fig. 2. The beam was monochromated and focused in two directions by means of a combination of a bent Laue Si crystal and a laterally graded multilayer [21]. The sample was positioned behind the focal spot. In combination with the use of an aperture this set-up resulted in the sample being illuminated by a nearly homogeneous 51 keV beam of dimensions 49×49 μm^2. Diffraction studies were performed in transmission mode by exposing a 14-bit FRELON CCD coupled by an image intensifier to a fluorescence screen of area 160×160 mm^2. Data acquisition times were typically 1 s.

To increase the volume characterized, exposures were made at a set of sample positions. For all samples these corresponded to the four points in a 2×2 (y,z)-grid, while for sample B a larger 4×4 (y,z)-grid was also used. In all cases, the distance between nodes was 40 μm. At each grid point, exposures were made for 22 equally spaced values of the rotation axis ω (see Fig. 2) within a range of 42°. To ensure an even sampling of integrated intensities, the sample was rotated by ±0.5° during each exposure. This corresponds to measurements of partial pole figures covering a fan of 42° around TD. As five reflections are recorded simultaneously on the detector this angular-range is sufficient to determine the crystallographic orientations of the evolving nuclei.

The data analysis methodology was described in Ref. [25]. In terms of image analysis, initially a background

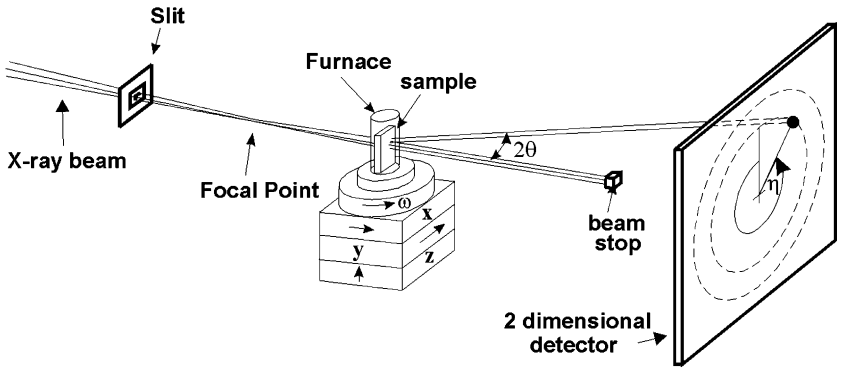

Fig. 2. Schematic diagram of the setup of the 3DXRD experiment, with indication of the angles 2θ, ω and η.

subtraction method was applied [27]. In the algorithm, a box of a given size is scanned across each image. The average and standard deviation of the pixel intensities within the box are determined as function of position. Positions with a small standard deviation are then defined to be in the background. The background level at each point is then determined by interpolation of the average values in the background areas. Images were spatially corrected by the program FIT2D [28].

For each nucleus, the orientation was determined with an accuracy of $\sim 1°$ by the multi-grain indexing algorithm, GRAINDEX [29]. In addition, the volume of the nucleus is readily found, as it is proportional to the integrated intensity of the associated diffraction spots. The proportionality constant was estimated from the integrated intensity of the diffracted signal from a reference Al powder with known thickness [21,25]. Furthermore, the (x, y, z) position of the nucleus can be estimated by trigonometry, based on information on when the nucleus "rotates out of the beam" during the ω-scan. To ensure the same volume was illuminated at all times, the position of the edges of the sample was repeatedly determined by scanning the sample.

The furnace provides a stable temperature of up to 500 °C, with a choice of working in a neutral atmosphere, and can rotate 360° about the z-axis. The sample is enclosed in a glass capillary tube with a thickness of 0.1 mm, giving rise to negligible absorption and minimizing diffuse scattering.

3. Results and discussion

Nucleation in three 300 μm thick plate shaped samples (A, B and C) was studied by the 3DXRD method. As a function of rotating the sample around the ω-axis, diffraction images were acquired with a highly efficient area-detector. Typical data from the as-deformed samples are shown in Fig. 3a. In the corresponding {111}, {200} and {220} partial pole figures, shown in Fig. 4, the orientations present are enclosed within broad poles associated with the three deformed grains at the triple

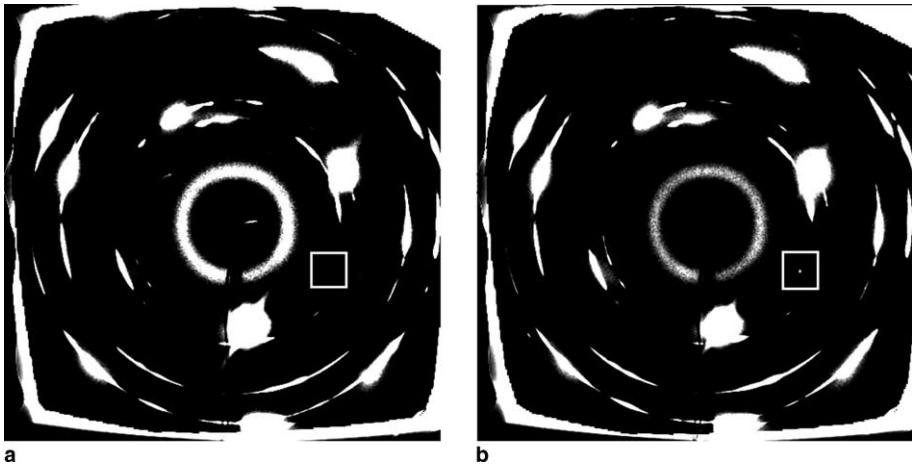

Fig. 3. Examples of 3DXRD images, acquired for sample B. A grey scale is used with white representing the more intense regions. The textured Debye–Scherrer rings of the {111}, {200}, {220}, {311} and {222} reflections are seen. The two images relate to the same position within the sample and represent (a) the as-deformed microstructure, and (b) the microstructure in the sample annealed for 3 h at 290 °C. The white box indicates the position of a diffraction spot, representing a nucleus.

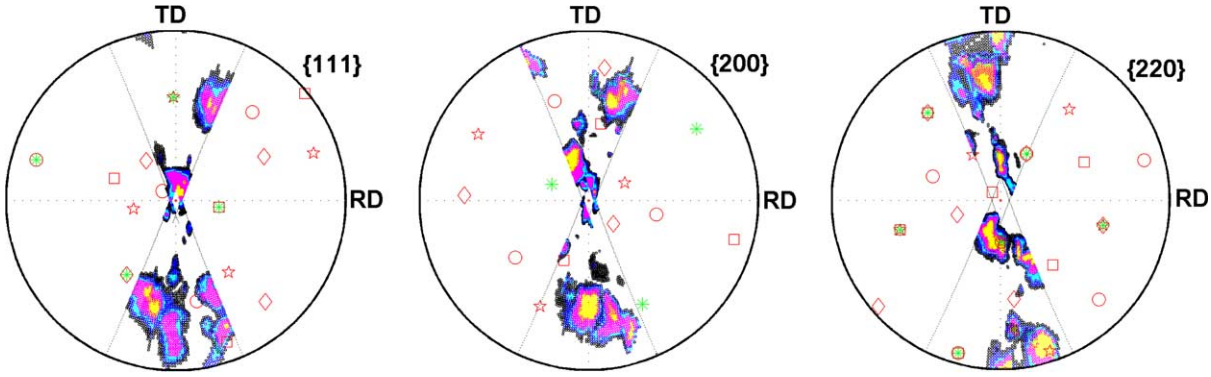

Fig. 4. Partial pole figures of sample B measured at the location of the nucleus with the new orientation. The orientations of the deformed microstructure are shown in colours with [black, blue, light blue, pink, yellow] corresponding to intensities of [400, 1000, 2500, 5000, 10,000] counts/s. The diffraction pattern from the sample after 3 h of annealing at 290 °C is very similar, except for the presence of three sharp diffraction spots, which are shown as green stars. The orientations of the associated four first order twins are marked by red symbols (squares, diamonds, circles, and stars). There is a small "invisible spot" in the centre of all pole figures.

junction. No smoothing has been applied. The individual elements in the deformed microstructure associated with these poles cannot be distinguished. Instead the virtue of the 3DXRD method in this case relates to characterization of the "empty" parts of the partial pole figures (i.e. within the measured ω-range of 42° but away from major poles). The boundary between the white and colored parts of the pole figures indicates the smallest volume elements that can be observed. This limit of 400 counts/s corresponds to an equivalent circle diameter (ECD) of 0.70 μm. In other words, all volume elements within an illuminated sample volume of $49 \times 49 \times 300$ μm^3 with an ECD larger than 0.7 μm will be recorded as a significant signal on the detector. It is characteristic of all three samples that large parts of the partial pole figures are empty, and furthermore that the intensities in the "tails" of the poles fall off rapidly with the distance to the centre of the pole.

The acquisition of such high-sensitivity pole figures was repeated with a frequency of ~10 min, while annealing the samples at 290 °C for 1–3 h. During this process, a few nuclei appeared, easily identifiable in the images as distinct point-like diffraction spots, see Fig. 3b. Based on the position and intensity of these spots 3DXRD specific analysis software was used to determine the orientation and position of the nuclei [21,25], as well as their volume as a function of annealing time.

Three nuclei were detected: one in sample A, two in sample B and zero in sample C—all positioned at least 65 μm from any surface. This result confirms that triple junctions are potential nucleation sites in this material, but also that not all junctions lead to nucleation, which is in good agreement with previous surface [20] and serial sectioning results [30].

The orientation of the sample A nucleus was identical to a first-order twin associated with an orientation close to the centre-of-mass of one of the poles. This nucleus grew to a size of ECD = 9.4 μm within 45 min. The orientation of one of the sample B nuclei was also identical to a first-order twin associated with an orientation close to the centre-of-mass of one of the poles. The results for the second nucleus in sample B, which is of the main interest here, is shown in Figs. 3 and 4. In this case six diffraction spots were observed in the "empty" parts of the partial pole figures (i.e. within the measured ω-range of 22° but away from the poles of the deformed parent grain), while another seven were on top of poles. From the six spots, the orientation of the nucleus was determined to be neither within the range of orientations found in the as-deformed sample, nor related to a first-order twin associated with any of the orientations in this range (see Fig. 4). This nucleus grew to a size of ECD = 6.1 μm within 3 h.

There are two explanations to why such a nucleus could be generated:

1. It emerged by reorientation of parts of the deformed structure.
2. It emerged from rare parts of the deformed microstructure associated with volume fractions of the order of 1.5×10^{-7}. All elements in the deformed microstructure associated with such hypothetical "odd orientations" have an ECD of less than 0.70 μm. This number corresponds to the lower limit of the size-distribution of elements as characterized by chord–length measurements in TEM [26]. Furthermore, they are substantially below the classical nucleation threshold [31], which in the present case is $ECD_{classic} > 1.1$ μm [1,32]. This explanation thus seems very unlikely.

A mechanism explaining how and why reorientation of parts of the deformed microstructure (explanation 1 above) should take place during the early stages of annealing has not been derived. The present result together with the previous observations of nuclei with

new orientations both at triple junction and away from them, however, strongly suggests that further detailed work should be devoted to the understanding of this. For the experimental part of such work, it appears the method presented here is an ideal tool. Uniquely, information on nucleation sites, orientation relationships and kinetics is obtained. The sensitivity of the method can be increased to ECD = 0.2 μm or better by improved focusing [33]. Statistics of nuclei characteristics can be extracted from repeated studies, which in turn is likely to give insight into the underlying mechanisms. Also, potential reorientations of emerging nuclei would be readily observable.

4. Conclusion

A unique method for in situ studies of nucleation in the bulk has been presented. The method is based on three-dimensional X-ray diffraction. It has been confirmed that volumes near triple junction lines are potential nucleation sites in 20% cold rolled copper. Three nuclei have been identified and followed during annealing at 290 °C. Analysis of orientation relationships with their deformed parent grains has revealed that nuclei may develop with orientations within the orientation distributions of the parent grains, being twin related here or with a new orientation that was not detected in the deformed parent grains.

Acknowledgments

The authors gratefully acknowledge the Danish National Research Foundation for supporting the Center for Fundamental Research: Metal Structures in Four Dimensions. This work was also partly supported the Danish Natural Science Research Council (via Dansync). The ESRF is acknowledged for provision of beam time. P. Nielsen and P. Olesen performed the pre-experiment sample scanning and testing.

References

[1] Humphreys FJ, Hatherly M. Recrystallization and related annealing phenomena. Oxford: Pergamon; 1995.
[2] Duggan B. Term suggest at international conference on textures of material. ICOTOM 11, 1996.
[3] Hansen N. Metall Mater Trans A 2001;32:2917.
[4] Driver JH, Juul Jensen D, Hansen N. Acta Metall Mater 1994;42:3105.
[5] Winther G. Acta Mater 2003;51:417.
[6] Bailey JE, Hirsch PB. Proc Roy Soc A 1962;267:11.
[7] Samajdar I, Doherty RD. Scr Metall Mater 1995;32:845.
[8] Vatne HE, Daaland O, Nes E. ICOTOM 10. Mater Sci Forum 1994;157–162:1087.
[9] Humphreys FJ, Fery M, Johnson C, Paillard P. In: Hansen N et al., editors. Proceedings of the 16th Risø international symposium on material science: Microstructural and crystallographic aspects of recrystallization. Roskilde, Denmark: Risø; 1995. p. 87.
[10] Wu GL, Godfrey A, Juul Jensen D, Liu Q. ICOTOM 14. Mater Sci Forum 2005;495–497:1309.
[11] Kikuchi S, Kimura E, Koiwa M. J Mater Sci 1992;27:4927.
[12] Juul Jensen D. In: Sakai T, Suzuki HG, editors. Proceedings of the 4th international conference on recrystallization and related phenomena, 1999;(JIM):3.
[13] Paul H, Driver JH, Maurice C, Jasienski Z. Acta Mater 2002;50:4339.
[14] Inoko F, Okada T, Tagami M, Kashihara K. In: Hansen N et al., editors. Proceedings of the 21st Risø international symposium on material science. Risø National Laboratory; 2000. p. 365.
[15] Godfrey A, Juul Jensen D, Hansen N. Acta Mater 2001;49:2429.
[16] Barett CS. Recrystallization texture of aluminium after compression. Metals Technol 1940:128–49.
[17] Driver JH, Paul H, Glez J-C, Maurice C. In: Hansen N et al., editors. Proceedings of the 21st Risø international symposium on material science. Risø National Laboratory; 2000. p. 35.
[18] Inoko F, Mima G. Scr Metall 1987;21(8):1039.
[19] Okada T, Huang X, Kashihara K, Inoko F, Wert JA. Acta Mater 2003;51:1827.
[20] Sabin TJ, Winther G, Juul Jensen D. Acta Mater 2003;51:3999.
[21] Poulsen HF. Three-dimensional X-ray diffraction microscopy. Berlin: Springer; 2004.
[22] Margulies L, Winther G, Poulsen HFI. Science 2001;291:2392.
[23] Offerman SE et al. Science 2002;298:1003.
[24] Schmidt S, Nielsen SF, Gundlach C, Magulies L, Huang X, Juul Jensen D. Science 2004;305:229.
[25] Poulsen HF, Lauridsen EM, Schmidt S, Margulies L, Driver JH. Acta Mater 2003;51:2517.
[26] Huang X, Leffers T, Hansen N. In: Bilde-Sørensen JB et al., editors. Proceedings of the 20th Risø international symposium on material science. Roskilde, Denmark: Risø National Laboratory; 1999. p. 365.
[27] Teuber J, Bowen J, Lauridsen EM, Private communication.
[28] Hammersley AP, Svensson SO, Hanfland M, Fitch AN, Häusermann D. High Pressure Res 1996;14:235.
[29] Lauridsen EM, Schmidt S, Suter RM, Poulsen HF. J Appl Cryst 2001;34:744.
[30] Vandermeer RA. Trans Metall Soc Aime 1959;215:577.
[31] Doherty R. In: Hansen N et al., editors. Proceedings of the 1st Risø international symposium on material science. Roskilde, Denmark: Risø National Laboratory; 1980. p. 57.
[32] Gordon P. Trans AIME 1955;203(9):1043.
[33] Ice GE, Chung JS, Tischler JZ, Lunt A, Assoufid L. Rev Sci Instrum 2000;71(7):2635.